DESIGN, OPTIMIZATION AND CHARACTERIZATION OF METAL OXIDE NANOWIRE SENSORS.

Fatima Ezahra Annanouch

Dipòsit Legal: T 328-2016

Fatima Ezahra Annanouch

Design, Optimization and Characterization of Metal Oxide Nanowire Sensors

DOCTORAL THESIS

Supervised by:

Prof. Eduard Llobet Valero and Prof. Jose Luis Ramirez

Department of Electronic, Electric and Automatic Control Engineering

UNIVERSITAT ROVIRA I VIRGILI

Tarragona

2015

UNIVERSITAT ROVIRA I VIRGILI
DESIGN, OPTIMIZATION AND CHARACTERIZATION OF METAL OXIDE NANOWIRE SENSORS.
Fatima Ezahra Annanouch
Dipòsit Legal: T 328-2016

Universitat Rovira i Virgili

FAIG CONSTAR que aquest treball, titulat “Design, Optimization, And Characterization of Metal Oxide Nanowire Sensors”, que presenta Fatima Ezahra Annanouch per a l’obtenció del títol de Doctor, ha estat realitzat sota la meva direcció al Departament d'Enginyeria Electrònica, Elèctrica i Automàtica d’aquesta universitat.

HAGO CONSTAR que el presente trabajo, titulado “Design, Optimization, And Characterization of Metal Oxide Nanowire Sensors”, que presenta Fatima Ezahra Annanouch para la obtención del título de Doctor, ha sido realizado bajo mi dirección en el Departamento de Ingeniería Electrónica, Electrónica y Automática de esta universidad.

I STATE that the present study, entitled “Design, Optimization, And Characterization of Metal Oxide Nanowire Sensors”, presented by Fatima Ezahra Annanouch for the award of the degree of Doctor, has been carried out under my supervision at the Department Electronic and Electrical Engineering and Automation of this university.

Tarragona, 2 de Març de 2015

El/s director/s de la tesi doctoral

El/los director/es de la tesis doctoral

Doctoral Thesis Supervisor/s

Eduard Llobet Valero

José Luis Ramírez Falo

Acknowledgments

First of all I would like to express my sincere gratitude and appreciation to my supervisor, Prof. Eduard Llobet, for his support, guidance, encouragement and advice throughout the last four years of my Ph.D. Without his patience, generosity and his confidence in me I could not have lead this research effort. I really feel fortunate to have worked with the finest supervisor I have ever met throughout the course of my studies.

I would also like to thank my supervisor Prof. Jose Luis Ramirez for his constructive suggestions, valuable advice and his endless and kind support during this doctoral work. My heartfelt gratitude to Prof. Benachir Bouchikhi, without whom I could not have known the MiNOS group. Along with them, I would also like to thank Prof. Xavier Correig and Prof. Xavier Vilanova for their help and support.

I extend a word of appreciation to Dr. Stella. Vallejos for all the support, help, and advice during my Ph.D. Special thanks to Prof. Chris Blackman who warmly welcomed me in his lab at UCL, and also for his help and collaboration.

My sincere thanks to Mercé, Mariana, Lukas, Rita and Núria in Servi de Recursos Cientifics i Tècnics of the Universitat Rovira i Virgili, for their guidance and support.

I would also like to express my gratitude to the members of Minos group: especially to Badi, Raul, Serena, Radu, Houda, Radouane, Rosa, Toni, Pierrick, Oriol, Tesfalem, Sergio and Enrique for their support, kindness, and collaboration. A personal thanks to Pinkie, for her friendship, support and the enjoyable days in Tarragona. I would also like to thank Riham, Rahma, Khadija, Sara, Noura, Laxmi, Francesco and Min for their kind love and friendship.

To my parents, Aziz and Aicha, my sister, Sofiya and my brother, Amine for being a source of endless love and support, I would like to express my deepest gratitude.

To my husband Zouhair, I want to say thanks for his unconditional love and encouragement and to say sorry for all the quality time we have lost.

Finally, I am grateful to the Spanish Ministry of Science and Innovation via grant no. TEC2012-32420.

Thesis publications

Full paper

1. J. Smulko, M. Trawka, C. G. Granqvist, R. Ionescu, **F. E. Annanouch**, Eduard Llobet, L. B. Kish, "New approaches for improving selectivity and sensitivity of resistive gas sensors: a review", Sensor Review, Accepted paper 04/2015.
2. **F. E. Annanouch**, I Gràcia, E Figueras, E Llobet, C Cané, S Vallejos, "Localized aerosol-assisted CVD of nanomaterials for the fabrication of monolithic gas sensor microarrays", Sensors and Actuators B, Accepted paper 03/2015.
3. **F.E Annanouch**, Z. Haddi, S. Vallejos, P. Umek, P. Guttmann, C. Bittencourt, E. Llobet, "Aerosol assisted CVD grown WO_3 nanoneedles decorated with Copper oxide nanoparticles for the selective and humidity resilient detection of H_2S", ACS Applied Materials & Interfaces, vol. 7, pp. 6842−6851, 2015.
4. T. Stoycheva, **F.E Annanouch**, I. Gràcia, E. Llobet, C. Blackman, X. Correig, S. Vallejos, "Micromachined gas sensors based on tungsten oxide nanoneedles directly integrated via aerosol assisted CVD", Sensors and Actuators B: Chemical, vol. 198, pp. 210–218, 2014.
5. S. Vallejos, T. Stoycheva, **F. E. Annanouch**, E. Llobet, P. Umek, E. Figueras, C. Canè, I. Gràcia, C. Blackman, "Microsensors based on Pt–nanoparticle functionalised tungsten oxide nanoneedles for monitoring hydrogen sulphide", RSC Advances, vol. 4, pp. 1489–1495, 2014.
6. **F. E. Annanouch**, S. Vallejos, T. Stoycheva, C. Blackman, E. Llobet, " Aerosol assisted chemical vapour deposition of gas-sensitive nanomaterials", Thin Solid Films, vol. 548, pp. 703–709, 2013.
7. **F. E. Annanouch,** T. Stoycheva, S. Vallejos, C. Blackman, X. Correig, E. Llobet, "AA-CVD growth and ethanol sensing properties of pure and metal decorated WO_3 nanoneedles", International Journal of Nanotechnology, vol. 10, pp. 455-469, 2013.
8. S. Vallejos, P. Umek, T. Stoycheva, **F. E. Annanouch**, E. Llobet, X. Correig, P. De Marco, C. Bittencourt, C. Blackman, "Single-Step Deposition of Au- and Pt-Nanoparticle- Functionalized Tungsten Oxide Nanoneedles Synthesized Via Aerosol-

Assisted CVD, and Used for Fabrication of Selective Gas Microsensor Arrays", Advanced Functional Materials, vol. 23, pp. 1313-1322, 2013.

Papers not included in the thesis

1. R. Calavia, **F. E. Annanouch**, X. Correig, O. Yanes, "Nanostructure Initiator Mass Spectrometry for tissue imaging in metabolomics: Future prospects and perspectives", Journal of Proteomics, 75, pp. 5061-5068, 2012.
2. Z. Haddi, A. Amari, **F. E. Annanouch**, A. Ould Ali, N. El Bari, B. Bouchikhi, "Potential of a Portable Electronic Nose for Control Quality of Moroccan traditional fresh cheeses", Sensor Letters, 9, pp. 2229-2231, 2011.

Table of content

Chapter 1: Introduction **1**

1. Motivation **1**

2. Objectives **4**

3. Thesis organization **5**

Chapter 2: Literature review **7**

2.1 Semiconducting metal-oxide gas sensors **7**

2.1.1 Working mechanism of metal-oxides gas sensor 8

2.1.2 Characteristics of metal oxides gas sensors 12

2.2 Tungsten trioxide (WO_3) **13**

2.2.1 Structural properties of WO_3 14

2.2.2 Tungsten oxide (WO_3) thick/thin film for gas sensors applications 16

2.3 Nanostructured metal oxides for gas sensing application- one dimensional nanostructures **19**

2.3.1 Modified nanostructures 22

2.3.2 Deposition techniques for 1D metal-oxides gas sensors 25

2.3.2.1 Direct physical deposition techniques 26

2.3.2.2 Direct chemical deposition methods 27

2.3.2.3 Growth mechanism of 1D metal oxide nanostructures 29

2.4 Aerosol assisted chemical vapour deposition (AACVD) method **31**

2.4.1 Basic principal of AACVD 32

2.4.2 Aerosol-assisted CVD – applications for gas sensors 34

Chapter 3: Experimental section **36**

3.1 Film deposition 36

3.1.1 AACVD reactors 36

3.1.1.1 Hot wall reactor 36

3.1.1.2 Cold wall reactor 38

3.1.2 Precursor characteristics 40
3.1.3 Active sensing layer deposition 41
3.1.3.1 General procedure....41
3.1.3.2 Annealing process....48
3.2 Material characterization....48
3.3 Gas sensor fabrication....50
3.3.1 Alumina gas sensors-1....50
3.3.2 Flexible polymeric sensors 51
3.3.3 Alumina gas sensors-2....53
3.3.4 MEMS-based gas sensors 54
3.4 Gas sensors characterization study....56
3.4.1 Measuring set up 56
3.4.2 Target gases 58
Chapter 4: Au and Pt nanoparticles functionalized tungsten oxide nanoneedles synthesized via aerosol assisted-CVD, and used for gas sensing application 59
4.1 Introduction....59
4.2 AACVD of WO_3 NNs functionalized with Au or Pt NPs grown via a hot wall reactor, onto alumina and flexible gas-sensors platforms 59
4.2.1 Single step deposition of Au- and Pt-NPs- functionalized WO_3 NNs using AACVD method onto alumina gas sensor substrate 60
4.2.1.1 Morphology and structure....61
4.2.1.2 Gas sensing characterization 63
4.2.2 Deposition via tungsten hexacarbonyl ($W(CO)_6$) precursor using a hot wall reactor 67
4.2.3 Single step deposition of Au- and Pt-NPs- functionalized WO_3 NNs using AACVD method, onto flexible gas sensor substrates 70
4.2.3.1 Morphology and structures....70
4.2.3.2 Gas sensing characterization 72

Table of content

4.3 AACVD of WO_3 NNs functionalized with Au or Pt NPs grown via a cold wall reactor, onto alumina and MEMS-based gas-sensor platforms 76

4.3.1 Using alumina gas sensor substrates 77

4.3.2 Using MEMS-based gas sensor substrates 79

4.3.2.1 Thermal and electrical characteristics of the microheaters 79

4.3.2.2 Morphology and structures 80

4.3.2.3 Electrical properties 85

4.3.2.4 Gas sensor characterization 85

4.4 Summary 91

Chapter 5: Cu_2O and Pd nanoparticle functionalized tungsten oxide (WO_3) nanoneedles synthesized via aerosol assisted-CVD, and used for gas sensing application 92

5.1 Introduction 92

5.2 Cu_2O NPs functionalized WO_3 NNs synthesized via aerosol assisted-CVD and used for H_2S detection 92

5.2.1 Material characterization 93

5.2.2 Gas sensing characterization 99

5.2.3 Gas sensing mechanism 103

5.2.4 Humidity cross-sensitivity 106

5.3 Pd NPs functionalized WO_3 NNs synthesized via aerosol assisted-CVD and used for gas sensing application 108

5.3.1 Material characterization 108

5.3.2 Gas sensing characterization 116

5.4 Summary 121

Chapter VI. Conclusions and future works 123

References 128

Abstract

In this thesis, I have studied and developed aerosol assisted chemical vapour deposition (AACVD) methods for the direct growth of non-functionalized and functionalized tungsten oxide nanoneedles, onto different transducer substrates, for gas sensing applications. This technique gives the possibility to co-deposit metals with metal oxides nanostructures within a single step deposition.

The nanostructured material synthesis, device fabrication, material characterization and gas sensing performance have been investigated.

AACVD method was employed for the direct growth and integration of the sensing film onto ceramic (alumina), MEMS (silicon micro hotplates) and flexible polymeric substrates, demonstrating its compatibility and suitability for growing metal oxide nanostructures onto a wide spectrum of sensor substrates. Furthermore, AACVD based on the localized heating of substrates employing their embedded resistive microheaters has been also performed and developed for the growth of WO_3 nanostructures, using a cold wall reactor. All the synthesized films used in this doctoral thesis were composed of pure WO_3 nanoneedles or WO_3 nanoneedles functionalized with either gold (Au), platinum (Pt), cuprous oxide (Cu_2O) or palladium (Pd) nanoparticles.

Various analytical techniques were used to characterize the morphology, the structure and the composition of the produced films. The results showed that our method is effective for growing single crystalline WO_3 nanoneedles decorated with metals/metal oxides nanoparticles at moderate temperatures (e.g., 380 °C), with cost effectiveness and short fabrication times, directly onto transducers in view of obtaining gas sensors. The gas sensing studies performed showed that these hybrid nanomaterials have excellent sensitivity and selectivity compared to pristine WO_3 samples. Cu_2O/WO_3 and Pd/WO_3 nanocomposites have shown excellent sensitivity and selectivity toward H_2S and H_2 gases respectively.

Resum

En aquesta tesi, he estudiat i desenvolupat un mètode de deposició química en fase vapor assistit per aerosol (AACVD), per al creixement directe de nanoagulles d'òxid de tungstè funcionalitzades o intrínseques. Els dipòsits s'han realitzat sobre diferents substrats trasndcutors per a la seva aplicació a la detecció de gasos. Aquesta tècnica ofereix la possibilitat de co-dipositar els metalls amb els òxids metàl·lics emprant una sola etapa de deposició.

La síntesi del material nanoestructurat, la fabricació del dispositiu, la caracterització dels materials i la detecció de gasos han estat investigades.

El mètode AACVD es va emprar per al creixement i la integració directa de la pel·lícula sensible sobre substrats ceràmics (alúmina), MEMS (micro hotplates) i polimèrics flexibles, el que demostra la seva compatibilitat i idoneïtat per al creixement de nanoestructures d'òxid metàl·lics sobre una àmplia gamma de substrats transductors. A més, el mètode AACVD s'ha implementat també en un reactor de paret freda per créixer les nanoestructures de WO_3, emprant l'escalfament localitzat que permeten aconseguir les microresistencias calefactores integrades en alguns dels transdcutors emprats. Totes les pel·lícules sintetitzades en aquesta tesi doctoral es componien de nanoagulles de WO_3 pur o de WO_3 funcionalitzat amb NPs d'or (Au), platí (Pt), òxid de coure (Cu_2O) o pal·ladi (Pd). Es van utilitzar diverses tecnologies d'anàlisi per caracteritzar la morfologia, l'estructura i la composició de les pel·lícules produïdes. Els resultats van mostrar que el nostre mètode és eficaç per al creixement de nanoagulles cristal·lines de WO_3 decorades amb nanopartícules de metalls / òxids metàl·lics, a temperatures moderades (és a dir, 380 ° C), amb eficàcia en els seus costos i amb temps de fabricació curts, directament sobre l'element transdcutor amb vista a obtenir sensors de gasos. Els estudis de detecció de gasos han mostrat que aquest nanomaterial híbrid té una excel·lent sensibilitat i selectivitat en comparació amb mostres de WO_3 pur. A més, els nanocompostos

Resum

Cu_2O/WO_3 i Pd/WO_3 han demostrat posseir una excel·lent sensibilitat i selectivitat cap als gasos H_2S i H_2, respectivament.

Resumen

En esta tesis, he estudiado y desarrollado un método de deposición química en fase vapor asistido por aerosol (AACVD), para el crecimiento directo de nanoagujas de óxido de tungsteno funcionalizadas o intrínsecas. Los depósitos se han realizado sobre distintos sustratos transdcutores para su aplicación a la detección de gases. Esta técnica ofrece la posibilidad de co-depositar los metales con los óxidos metálicos empleando una sola etapa de deposición.

La síntesis del material nanoestructurado, la fabricación del dispositivo, la caracterización de los materiales y la detección de gases han sido investigadas.

El método AACVD se empleó para el crecimiento y la integración directa de la película de sensible sobre sustratos cerámicos (alúmina), MEMS (micro hotplates) y poliméricos flexibles, lo que demuestra su compatibilidad e idoneidad para el crecimiento de nanoestructuras de óxido metálicos sobre una amplia gama de sustratos transductores. Además, el método AACVD se ha implementado también en un reactor de pared fría para crecer las nanoestructuras de WO_3, empleando el calentamiento localizado que permiten conseguir las microresistencias calefactoras integradas en algunos de los transductores empleados. Todas las películas sintetizadas en esta tesis doctoral se componían de nanoagujas de WO_3 puro o de WO_3 funcionalizado con NPs de oro (Au), platino (Pt), óxido de cobre (Cu_2O) o paladio (Pd). Se utilizaron diversas tecnologías de análisis para caracterizar la morfología, la estructura y la composición de las películas producidas. Los resultados mostraron que nuestro método es eficaz para el crecimiento de nanoagujas cristalinas de WO_3 decoradas con nanopartículas de metales / óxidos metálicos, a temperaturas moderadas (es decir, 380 °C), con eficacia en sus costes y con tiempos de fabricación cortos, directamente sobre el elemento trasndcutor con vistas a obtener sensores de gases. Los estudios de detección de gases han mostrado que este nanomaterial híbrido tiene una excelente

sensibilidad y selectividad en comparación con muestras de WO_3 puro. Además, los nanocompuestos Cu_2O / WO_3 y Pd / WO_3 han demostrado poseer una excelente sensibilidad y selectividad hacia los gases H_2S y H_2, respectivamente.

Chapter 1: Introduction

1. Motivation

The chemical, pharmaceutical, food and automotive industries, petroleum production, natural gas processing and so forth, all have brought great benefits to our modern lifestyle. However, in the last decades, with the development of these industries, the human health has been negatively influenced, due to the emission of toxic gases in the environment and the frequent exposure to indoor gases whilst working.

For instance, hydrogen sulphide (H_2S) is a poisoning gas, which is released from sewage, manure, hot springs and petroleum production and refining. People exposed to a concentration above 10 ppm of this gas, can experience irritation of the eyes, nose, throat, and respiratory system, while higher concentrations (250 ppm) can cause nausea, shock, rapid unconsciousness, coma, and even death [1-4]. Benzene (C_6H_6), a volatile organic compound (VOC), is one of the air indoor or outdoor pollutants that can cause several diseases such as allergies, asthma, cancer and emphysema [5,6]. Nitrogen oxides (NOx) whose main component is NO_2 are coming principally from motor vehicle exhaust and stationary sources such as electric utilities and industrial boilers. They are considered as a major cause of the formation of ground level ozone in the stratosphere. The frequent exposure to concentrations that are higher than those existing in the ambient air can cause irritation of the lungs and lower resistance to respiratory infections such as influenza [7,8]. Moreover, flammable gases such as hydrogen, are very dangerous components, since under specific conditions they can produce unwanted explosion or fires and then pose risk to the safety of the human being.

Therefore, there is a need and a strong industry-driven demand for developing a new generation of reliable, robust, accurate and cost effective gas sensors with enhanced sensitivity

and selectivity, reduced moisture cross-sensitivity and fast response time to facilitate the early detection of such pollutants in the environment, before their concentrations reach potentially hazardous levels.

In the last few years, intensive research was oriented toward the fabrication of solid state gas sensor based mainly on metal oxide materials such as WO_3, ZnO, SnO_2, TiO_2, CuO etc. Owing to their low cost and their reliability in detecting various toxic gases with enough sensitivity and good reproducibility, metal oxide sensors have been used in various applications such as domestic gas alarms, food quality control, environmental monitoring and so forth. It is worth noting that in the past decades, significant advances in industrial and environmental monitoring were achieved owing to the use of these sensors. However, they also suffer from some drawbacks, which influence their usability, such as the lack of selectivity, the dependence of humidity under varying environmental conditions and the instability (i.e. drift).

With the advent of nanotechnology, one dimensional (1D) metal oxide nanostructures have called attention as a new generation of functional materials exhibiting several advantages for gas sensing applications [9-11]. A large amount of scientific papers on metal-oxide nanostructures is published every year. Specifically, the fields of materials and gas sensors have become one of the most active research areas within the nanoscience community.

Due to their unique properties, these materials have demonstrated their capability to improve the gas sensor performances, especially in term of sensitivity and response/recovery times. They are characterized by their high surface to volume ratio which provides more surface area for both chemical and physical interactions. They have high level of crystallinity, which positively influences the stability of sensor response. They possess quantum confinement effects, which impact the charge transport and electronic band structures, and then enhance the gas

sensing properties. Thus, all these advantages make them an excellent building-block for micro/nanoscale gas sensors, compared to their bulk counterparts [10,12].

Regarding the lack of selectivity, many works have shown that by adding catalyst nanoparticles onto the metal oxide matrix (i.e., surface functionalization of the low-dimensional metal oxide), the selectivity toward a target gas can be significantly increased, especially when the size of the metal nanoparticles is lower than 5 nm [13,14].

Numerous routes have been reported for the synthesis of low dimensional metal oxide nanostructures. These can broadly be classified into two categories: direct physical deposition methods and direct chemical deposition methods.

On one hand, the techniques belonging to the first category involve very sophisticated reactors with vacuum systems, which make them very expensive and not viable for a large scale commercial production. On the other hand, conventional CVD methods, which belong to the second category, require very elevated temperatures for the growth of metal oxide nanostructures, which prevents the use of microelectronic substrates (i.e. microhotplates) that are widely used in gas sensor production.

Moreover, most of the reported techniques concerning the growth of functionalized nanostructured materials, employ a multi-step approach, in which in the first step the nanostructured materials are synthesized. This is followed in the second step by a functionalization in which metal nanoparticles are deposited onto the surface of the previously grown nanostructures. In some cases, the process still needs a third step in which the as-deposited metal nanoparticles are oxidized. This involved, multi-step process can not be easily scaled up and, therefore, will hardly be adopted by the industry for mass production of sensors.

Consequently, aerosol assisted chemical vapour deposition (AACVD) method is proposed as one possible solution to overcome the cited problems. This technique offers a wide range of

advantages that are not found in conventional CVD methods. It is an inexpensive and industrially attractive technique. it is conducted at low temperatures, typically in a range between 350 and 500 ºC, which makes it suitable for the direct, bottom-up integration of gas-sensitive nanomaterials onto a wide spectrum of substrates including glass, ceramic, silicon micro electro-mechanical systems (MEMS) or even flexible polymeric. AACVD allows for the use of a wide range of precursors owing to its solution-delivery based principle. Furthermore, it is a suitable method for growing, in a single step, 1D metal oxide nanostructures decorated with metal nanoparticles.

2. Objectives

The objectives of the current research were as following:

1. To synthesize tungsten oxide (WO_3) nanoneedles (NNs) from a commercialized precursor, using aerosol assisted chemical vapour deposition method. Herein, several depositions will be performed in order to define the optimal conditions for high quality material growth.
2. To grow the nanostructured material in a wide spectrum of substrates (glass, ceramic, MEMs and polymeric) to test the flexibility of the AACVD method.
3. To functionalize pristine WO_3 NNs with either gold or platinum nanoparticles (NPs) via a single step AACVD method. The direct growth will be realized onto alumina and flexible polymeric substrates. After that, the fabricated sensors will be tested toward various concentrations of H_2 and Ethanol analytes, in order to examine the gas sensing properties of the synthesized films.
4. To synthesize pristine WO_3 and WO_3 NNs functionalized with gold or platinum NPs, using cold wall AACVD reactor and the self-heating capability of the sensor. Herein, the fabricated MEMs-based gas sensors will be used for Ethanol, CO and H_2 detection.

5. To fabricate hydrogen sulphide gas sensors using cuprous oxide (Cu_2O) NPs functionalized WO_3 NNs. The sensing film will be directly integrated onto MEMs-based gas sensor substrates via a single step AACVD method.

6. To study the optimal conditions for the modification of WO_3 NNs with palladium NPs. Herein, two different routes of functionalization will be used: one single step and double step AACVD method. After that, the fabricated sensors will be tested toward hydrogen.

7. To investigate the physical, chemical and electronic properties of all the synthesized films using various scientific instruments such as SEM, TEM, HRTEM, XRD, EDS, Raman, XPS and NEXAFS.

3. Thesis organization

This thesis has been organised in six chapters.

Chapter 1 gives an overview to the reader about the motivation for realising this research and its main objectives.

Chapter 2 presents the state of the art of metal oxide gas sensors. It includes the working principles and the characteristics of metal oxide gas sensors. It describes the structural properties of tungsten oxide material and its gas sensing applications. Next, it reviews 1D metal oxide nanostructures for gas sensing applications, the modification of the nanostructures by using nanoparticles of metals additives and the methods employed for the growth of these nanostructures. Finally, the last part of this chapter is dedicated to the AACVD method, its basic principles and its use for gas sensing applications.

Chapter 3 describes in its first part, the film deposition procedure, the AACVD reactors, the precursor characteristics and a summary of the experimental conditions used for the growth of all the films synthesised during this thesis. The second part outlines the methods employed for the characterization of the nanomaterials grown such as scanning electron microscopy, transmission

electron microscopy and so forth. The last part describes the fabrication of the different gas sensor transducers used in this thesis and the gas sensing characterization, which involves the measuring set up and the target gases.

Chapter 4 focuses on the growth of WO_3 NNs functionalized with gold or platinum NPs using AACVD method. Herein, the findings were grouped and presented in two parts: AACVD of WO_3 NNs functionalized with Au or Pt NPs grown via a hot wall reactor, onto Alumina and flexible gas-sensors platforms and AACVD of WO_3 NNs functionalized with Au or Pt NPs grown via a cold wall reactor, onto alumina and MEMS-based gas-sensor platforms. In each part, film analysis and gas sensing characterization are discussed.

Chapter 5 presents the results obtained from the functionalization of WO_3 NNs with either Cu_2O or Pd NPs using aerosol assisted-CVD method. The film analysis and gas sensing characterisation are discussed.

Chapter 6 presents the conclusions of this doctoral thesis and some suggestions for possible future work.

Chapter 2: Literature review

The word “sensor” is driven from Latin “sēnsus” which means perceived, from “sentīre” to perceive and to observe. Nowadays a sensor is a device that detects inputs from its environment, such as radiation, heat, pressure, displacement, acceleration, mass, magnetic field or the presence of chemical or bio-chemical compounds, and that converts the detected inputs into electronic or optical signal, which can be further processed, transmitted, stored and displayed by electronic systems and, eventually, recognized by human beings.

2.1 Semiconducting metal-oxide gas sensors

Metal oxide semiconductor (MOX) gas sensors known also as chemoresistive gas sensors, are important components in a wide spectrum of applications such as environmental monitoring, the control of industrial processes in general and of chemical processes in particular or personal safety at home and at the workplace, only to cite a few. These sensors can be described as a device, which upon exposure to a single gas or to mixture of gaseous compounds, undergoes a change in its electrical resistance. The resistance change of MOX sensors follows a potential law of the gas concentration [15].

The first report on semiconductor gas sensors was published in 1962 by Seiyama et al, in Japan [16]. They utilized the semiconductor catalysis mechanism, which is based on the change of the metallic oxide resistance (zinc oxide) upon absorption or desorption of a gas. In other words, when the sensor is surrounded by an oxidizing or reducing gas, this later tends to extract electrons from the sensor or to provide them to the sensor. Hence, the density of the charges carries is changing, which leads to a change in the resistance of the material. This finding has triggered an interesting pathway toward the development of new gas sensors by various groups. Among these, Taguchi, which has invented a gas sensor based on stannic oxide, later

commercialized these as household gas alarms in 1969 [17]. Since then, lots of efforts have been oriented toward the development of those sensors, to further enhance their sensing performance, to simplify their use for the safety of human beings and to bring down their costs.

Owing to their low cost, relative simplicity and their large number of detectable gases, n-type semiconductor metal oxides including tungsten oxide (WO_3), zinc oxide (ZnO), tin dioxide (SnO_2), titanium dioxide (TiO_2) and indium oxide (In_2O_3) are the most reported in the literature [7-9]. They possess a broad range of electronic, chemical, and physical properties (e.g. wide band gap, small activation energy, superconductivity, high dielectric constants, reactive electronic transitions, optical transparency etc.), that allow them to be widely used and investigated in the detection of volatiles and other gases [18].

The typical metal-oxide sensor device consists of the following parts: the sensing layer (metal oxide deposited active sensing material), the sensor substrate (normally it contains two electrodes on the front side -to enable measuring the resistance of the metal oxide film- and a heater track on the back side, which allows for the device to reach its optimal operating temperature that is in general well above room temperature) and the gas sensor support or package (allows the connection of this device to the global measurement system). To elaborate a reliable gas sensor device, the first important step is the synthesis and the deposition of the sensing material. This step represents a crucial part in the fabrication of the sensor. The processing techniques should be carefully chosen to provide the desired material with the oxide composition required.

2.1.1 Working mechanism of metal-oxides gas sensor

The sensing mechanism of metal oxide sensors involves two key functions as it is shown by Figure II.1: receptor function and transducer function [19].

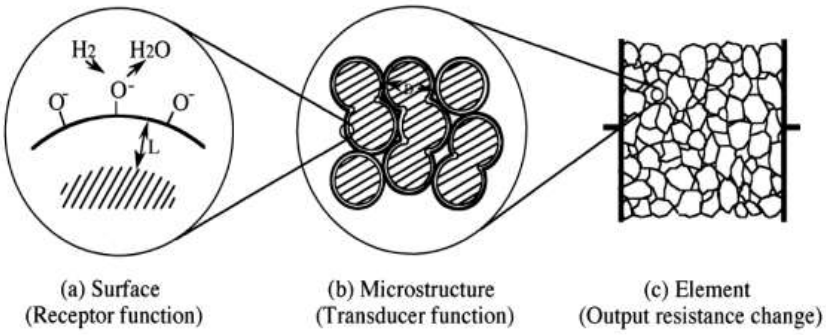

Figure II.1: Schematic diagram of the receptor and transducer functions of a semiconducting metal-oxide layer [19]

Receptor function

This function converts the chemical information obtained from the interaction between the target gas molecules and the surface of the sensitive layer, into the form of energy that can be measured by the transducer [20]. When the metal oxide film is exposed to air, oxygen molecules can adsorb on its grain surface and boundaries forming chemisorbed oxygen species such as O_2^-, O^-or O^{2-}. The nature of oxygen adsorbates depends on the operating temperature (Equation 1-4). Thus, it is believed that O^{2-} are the most dominant adsorbed species, since the majority of metal oxide gas sensors works at temperature of 300-450 °C [21]. Furthermore, oxygen adsorbates lead to a band bending and an electron depleted layer (i.e. space-charge layer), since they trap electrons from the conduction band of the n-type metal oxide film, which makes the material highly resistive. When the metal oxide is exposed to a reducing gas, the chemisorbed oxygen species can react with the reducing gas molecules, leading to a decrease of the band bending and the thickness of the space charge. This behaviour can be ascribed to the release of the initially trapped electrons (at oxygen adsorbates) back to the conduction band. In contrast, for an oxidizing gas, more electrons are extracted from the conduction band and the conductivity decreases further [22].

$$O_{2(g)} \rightarrow O_{2(ads)} \quad (1)$$

$$O_{2(ads)} + e^- \rightarrow O^-_{2(ads)} \quad < 100\ °C \tag{2}$$

$$O^-_{2(ads)} + e^- \rightarrow 2O^-_{(ads)} \quad 100 < T < 300\ °C \tag{3}$$

$$O^-_{(ads)} + e^- \rightarrow O^{2-}_{(lattice)} \quad > 300\ °C \tag{4}$$

Transducer function

The transducer function can be explained by the ability to transduce the change in the depletion width to a change in the electrical resistance. It is well known that the interactions between the target gas molecules and the metal oxides can happen at the surface and the boundaries of the grains. Thus, the electrons depleted from the conduction band can be easily transported through different grains, which produce an immediate change in the electrical resistance of the material.

Many works in the literature have demonstrated the dependence between the depletion width and the microstructure of the material [23] (i.e. grain size and /or the film porosity). It was reported that the ratio between the grain size (D) and the Debye length (L_D) (is the scale over which charge separation happens in a semiconductor) can mainly affect the magnitude of the conduction variation. The value of L_D is determined by the following equation [23]:

$$L_D = \sqrt{\frac{\varepsilon\varepsilon_0 kT}{e^2\rho}} \tag{5}$$

Ɛ: dielectric constant of the material; ρ: density of major charge carriers in the material.

If the grain size is significantly bigger than the Debye length (D >> 2LD), the depletion region only appears near the surface of the grain. The whole crystallites are unaffected by the gas interaction and the conductivity in this case is controlled by the space charge region between the grain boundaries (GB) (Figure II.2.a). As the grain size decreases the depletion region extends deeper into the grains and consequently the core region, which is relatively conductive with

respect to the depletion region adjacent to the surface, becomes smaller. When the grain size approach but still higher than $2L_D$ ($D \geq 2L_D$), the depletion region that surrounds each neck forms a constricted conduction channel within each aggregate. Consequently the conductivity depends not only on the grain boundary barriers but also on the cross section area of those channels (Figure II.2.b). When the grain size is extremely small ($D < L_D$), the depletion region is extended to the whole particles and the energy bands are almost flat all over the whole structure of the interconnected grains. Thus, no significant barriers are formed and the conductivity is governed by the crystallites, which results in an improvement of the sensitivity (Figure II.2.c) [23].

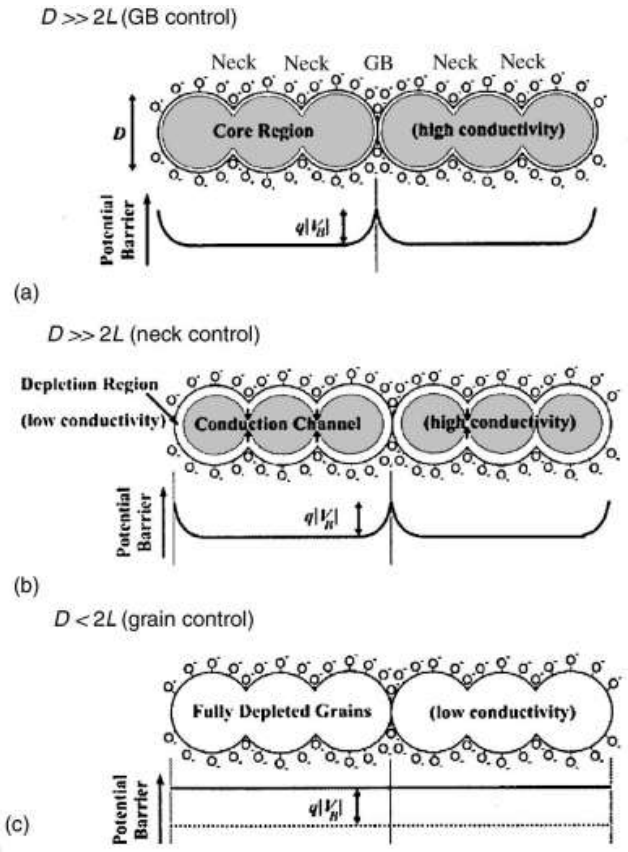

Figure II.2. Schematic model of the effect of the crystallite size on the sensitivity of metal-oxide gas sensors: a) D >> 2L (Grain boundary control); b) $D \geq 2L_D$ (neck control); D < 2L (grain control). [23]

2.1.2 Characteristics of metal oxides gas sensors

In order to qualify the output signal produced by metal oxide sensors, some specific parameters are generally used [24].

- **Sensor response**

At an equilibrium state in a gas sensor, the response is defined as a ratio between the resistance in air (R_{air}) and the resistance after subjection to the gas (R_{gas}). The response is expressed by:

$$S = \frac{R_{air}}{R_{gas}} \text{ (}n\text{-}type \text{ semiconductor)} \quad (6)$$

$$S = \frac{R_{gas}}{R_{air}} \text{ (}p\text{-}type \text{ semiconductor)} \quad (7)$$

- **Sensitivity**

It is a change of the measured signal per analyte concentration unit, i.e., the slope of a calibration graph, which is obtained by reporting the values of analyte concentrations and their corresponding response intensities on the abscissa and ordinate axis, respectively.

- **Selectivity**

It refers to the characteristics that determine whether a sensor can respond selectively to a group of analytes or even specifically to a single analyte.

- **Stability**

It is the ability of a sensor to maintain its properties for a certain period of time. This includes retaining the sensitivity, selectivity, baseline resistance value and response, and recovery time.

- **Response time**

It is the time required for an *n*-type sensor to reach a fixed percentage (e,g, 90%) of its steady-state resistance value when it is exposed to an oxidising gas (to 110% of its steady-state value when exposed to a reducing gas). A small value in its response time is a good characteristic for the sensor to have.

- **Recovery time**

It is the time taken by the sensor to return to a fixed value (e.g.10 % for the measurement of an oxidizing gas and 90% for a reducing gas) of the saturation value of its resistance when it is subjected to a clean air. This value should be also small to obtain a good sensor.

- **Detection limit**

It is the lowest concentration of the analyte that can be detected by the sensor under given conditions, particularly at a given temperature. Detection limit is generally determined by the sensitivity and the noise levels in sensor response. It is often assumed in gas sensor characterization that the limit of detection is reached when the response signal is three times higher than the noise level.

2.2 Tungsten trioxide (WO_3)

Tungsten is a Swedish term, which can be directly translated to English language as “heavy stone”. It is one of the heavy element that was formed in massive stars though energy consuming reactions. It was discovered at the end of the 18^{th} century by Juan Jose and Fausto Elhuyar [25]. Its origin name was “wolfram” and its symbol is W. Additionally, it is a hard transition metal, belonging to the refractories (Nb, Nb, Ta, Mo and Re). It has the second highest melting point and the lowest vapour pressure of all the elements [25]. Tungsten metal typically does not occur as a free element in nature and can exist in many forms in a wide spectrum of tungstic acids and a variety of different compounds such as tungsten trioxide, tungsten carbide, and ammonium

paratungstate. Furthermore, it can be found in many oxidation states such as W[0], W[2+], W[3+], W[4+], W[5+], and W[6+], many of which are non-stoichiometric.

2.2.1 Structural properties of WO_3

Tungsten trioxide (WO_3) structure consists of a three-dimensional network of corner-sharing WO_6 octahedron units, linked by W-O-W bonds. In this unit, the oxygen atoms are situated in the corners, while tungsten atom is located in the centre. The average distance between tungsten atom and oxygen atoms is about 1.90 Å, while this value remains modifiable regarding to different structures [26]. It was reported that the connectivity of this network exhibits the cubic perovskite-like structure (see Figure II.3), which is identical to ReO_3 and AMO_3 perovskite structure in the absence of an A cation [27]. However, it was found that the symmetry of WO_3 is lowered by two distortions: tilting of WO_6 octahedrons and displacement of tungsten from the centre of its octahedron. Depending on the temperature, these distortions result in the presence of tungsten oxide at different phases. Below -50 °C monoclinic (ε-WO_3), from -50 °C to 17 °C triclinic (δ-WO_3), from 17 °C to 330 °C monoclinic (γ-WO_3), from 330 °C to 740 °C orthorhombic (β-WO_3) and above 740 °C tetragonal (α-WO_3) [28]. It is worth noting that at the nanoscale, the phase transition temperatures are lower. The crystal structures are summarized in Table II.1.

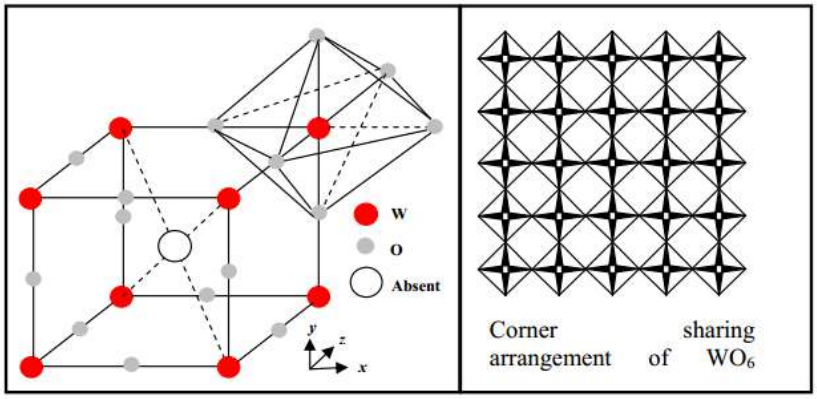

Figure II.3. Tungsten oxide (WO_3) crystal structure.

Table II.1. Summary of WO_3 crystal structures depending on the temperatures [28]

Temperature, °C	Crystal structure	Space group	Lattice constants, A°	Lattice angles, degrees
Below -50°C	monoclinic (ε-WO_3)	Pc-C^2	a=5.275 b=5.155 c=7.672	β=91.7º
-50 to 17 °C	triclinic (δ-WO_3)	P1 -C^1	a=7.30 b=7.52 c=7.69	α=80.85º β=90.82º γ=90.95º
17 to 330 °C	monoclinic (γ-WO_3)	$P2_1/n$	a=7.302-7.306 b=7.530-7.541 c=7.690-7.692	β=90.83- 90.88º
330 to 740 °C	orthorhombic (β-WO_3)	Pmnb-D^{16}	a=7.340 b=7.546 c=7.728	-
above 740 °C	tetragonal (α-WO_3)	P4/nmm-D^7	a=5.272 c=3.920	-

The electrical and chemical properties of tungsten oxide are vigorously dependent on the crystalline structure. It was reported that at room temperature, monoclinic (γ -WO_3) is the most stable phase [29]. Lattice oxygen vacancies represent one of the fundamental defects of tungsten oxides. The absence of an oxygen atom from the habituate lattice site leads to a partial replacement of W^{+6} by W^{+5} and W^{+4} and the formation of non-stoichiometric tungsten oxides WO_{3-x}. Consequently, the electronic band structure is modified and the conductivity of the material is increased [30].

2.2.2 Tungsten oxide (WO_3) thick/thin film for gas sensors applications

Tungsten trioxide is an n-type semiconductor with a variety of chemical and physical properties that have resulted in this material being widely used in gas sensing applications. The first WO_3 sensor was reported by *Shaver et al.* in 1967 [31]. They showed that the conductivity of Pd-activated WO_3 film is increased by one order of magnitude upon exposure to H_2 gas. Besides this finding and during the following 20 years, WO_3 did not attract the attention of many gas sensor research groups. On one hand, WO_3 was discovered as an active material for electrochromic applications, thus many attention was oriented toward its relevant electrochromic properties. On the other hand, at that time, TiO_2 and SnO_2 were the mainstream chemoresistive gas sensors, since they showed promising results and they were able to be commercialized. However, from 1990 onwards, a high number of papers studying WO_3 for gas sensing have been published. It has been found by many researchers, that tungsten oxide sensors exhibit excellent sensitivity toward NO_x (NO_2 and NO) the major culprits to the global warming [32]. It has also been reported that WO_3 sensors could be used to detect a variety of toxic gases, such hydrogen sulphide (H_2S), ammonia (NH_3), ethanol (C_2H_5OH), carbon monoxide (CO), hydrogen (H_2) and ozone (O_3). Table II.2, outlines important published works on WO_3 thick or thin films based gas sensor and their characteristics.

Table II.2. Important published works on WO_3 thick or thin films based gas sensor and their characteristics.

Material	Synthesis method	Concentration (ppm)	Sensor response	Reference
NO_2				
WO_3	Screen printing	100	210	[32]
WO_3	RF Sputtering	100	13.5	[33]
WO_3	Powder dip-coating	80	97	[34]
WO_3	Sol-gel process	3	226	[35]
WO_3	Sol-gel process	0.1	2.3	[36]

WO_3:Al	Reactive gas deposition	5	105	[37]
WO_3	Sol-gel process	1	100	[38]
WO_3:Au	Colloidal chemical method	10	430	[39]
H_2S				
WO_3:Au	Reactive gas deposition	35	55	[37]
WO_3	Powder dip coating	200	2	[40]
WO_3	Thermal oxidation	10	--	[41]
WO_3:Au	RF sputtering	3.5	46	[42]
WO_3	Arc discharge vaporization	10	10^4	[43]
WO_3	Advanced reactive gas deposition	10	10^3	[44]
H_2				
WO_3	RF sputtering	1000	13.6	[45]
WO_3:Pt	RF sputtering	200	2.2	[46]
WO_3:Pt	RF sputtering/dip coating	200	25.6	[47]
WO_3:Pd	Chemical synthesis	200	10	[48]
NH_3				
WO_3	-------	1000	6	[49]
WO_3	Thermal oxidation	100	7	[50]
WO_3:Pt	RF sputtering	1000	1000	[42]
WO_3:Pt	Sol-gel process	4000	12.5	[51]
WO_3:Mo	Aqueous soakage method	30	10.1	[52]
WO_3:MoO_3	Thermal decomposition	5	7	[53]
CO				
WO_3	Sol-gel process	100	14	[54]
WO_3	Thermal decomposition	1000	0.2	[55]
Ethanol				
WO_3	advanced gas deposition unit	20	3.3	[56]
WO_3:Pt	Aqueous solution preparation	100	90	[57]
WO_3:TiO_2	high-energy ball milling method	1000	21.6	[58]
WO_3	advanced gas deposition unit	100	76.4	[59]
Ozone				
WO_3:Au	Vapour deposition	0.8	78	[60]
WO_3	RF sputtering	0.8	4.8	[61]
WO_3:TiO_2:Au	Calcination	2.5	64	[62]

Different methods were used for synthesising small grained thick /thin films of tungsten oxide (see Table II.2). For example, screen printing and drop coating techniques, which they need the preparation of WO_3 powder paste and then printed or dropped to the sensor substrate. Sol-gel, is another technique for the synthesis of thick films. It is known also by wet-chemical process, and it is based on the hydrolysis of organometallic compounds or inorganic salts. When the sol is prepared, it can be coated to the substrate via spin coating or screen printing methods [35,36].

Regarding the synthesis of thin films sensing element, RF magnetron sputtering (pure tungsten target) is one of the most used techniques to produce thin films with small grain size. It is a physical vapour deposition, which involves ejecting the material from the target into the sensor substrate [42,61]. To obtain a high quality material with controlled thickness, stoichiometry and microstructure, thermal evaporation deposition is one of the techniques that offers better results. This method belongs to the physical vapour deposition category. It consists of the thermal evaporation of the source material inside a vacuum chamber. In addition, to obtain material with high purity, high temperatures with ultra-high vacuum ($< 10^{-9}$) are required [55, 60].

Besides the successful works mentioned above, conventional metal oxide gas sensors still suffer from some drawbacks such as low sensitivity (due to limited surface-to-volume-ratio) and high working temperature, since most metal oxide gas sensors must be operated at temperatures exceeding 350 °C and, sometimes reaching as high as 500 ºC in order to improve their sensitivity. Thus, in the recent years and with advent of nanotechnology, many scientists and research groups have oriented their efforts toward the development of nanostructured metal oxide gas sensors.

2.3 Nanostructured metal oxides for gas sensing application- one dimensional nanostructures

Nanostructured materials are those having properties defined by features smaller than 100 nm [12]. They can be divided into three groups depending on how many dimensions are on the nanoscale. Zero dimensional nanostructures 0D including nanoparticles or nanodots, one dimensional nanostructures 1D such as nanoneedles, nanowires, nanorods, nanofibers, nanocombs, nanoribbons etc., and two dimensional nanostructures which are called also films. These nanostructures offer a new category of materials with novel physical, chemical and biological properties that do not exist in their bulk counterparts (e.g. high surface to volume ratio, high crystallinity and stability of both structural and electro-physical properties). In addition, they can be produced either by using bottom-up or top-down techniques.

In the last 10 years, the activity in growth and characterisation of metal oxide nanostructures has increased exponentially and a large number of scientific papers have been published on metal-oxide nanostructures and specifically, in the field of nanostructured metal-oxides for gas sensing. This has become one of the most active research areas within the nanoscience and nanotechnology community. Moreover, new fundamental research is paralleled with original and inspired potential applications, including membranes for gas filtration and nanofiltration, next generation computer chips, hydrogen production by water photolysis and its storage, solar cell and nanowires for energy conversion and storage [63- 65]. Besides of these, they are also used in biological and medical applications such as in cancer treatment, drug delivery or bio labelling and bio tagging [66]. This chapter will be limited mainly to semiconducting devices with one-dimensional nanostructures such as nanoneedles and nanowires.

In 1991, Yamazoe and co-workers [19] showed that the reduction of crystallite size enhanced significantly the performance of gas sensors. Therefore, one dimensional (1-D) metal

oxide nanostructures (Figure II.4) including nanoneedles, nanorods, nanowires or nanotubes have emerged as a general platform for ultra-sensitive metal oxide gas sensors [11,12,65,66]. Due to their unique properties, these materials have demonstrated their capability to improve the gas sensor performances, especially in term of sensitivity and response/recovery times. They are characterized by their high surface to volume ratio, which means that an important area of the material will be exposed to the target gas. It was reported that at such small scale, most of the nanostructures atoms are surface atoms. Thus the number of reactive sites is amplified and the sensitivity is increased. Moreover, they are known by their radius, which is comparable to the Debye length (L_D) over a wide temperature and doping range. This distinctive characteristic strongly influences their electrical properties (the depth of the space-charge layer), which results in a better sensitivity and fast gas sensing kinetics. Moreover, 1D metal oxide nanostructures have highly improved crystallinity compared to multi-granular oxides, and this makes their sensor responses highly stable over a wide range of working temperatures [12,67-69].

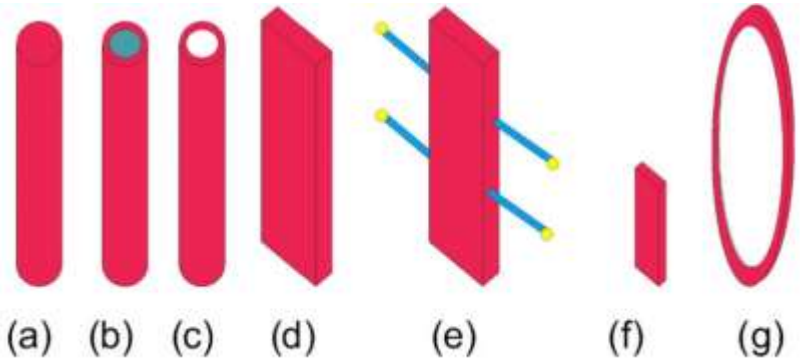

Figure II.4. Schematic drawing of some of the possible morphologies: (a) nanowire, (b) core shell nanowire, (c) nanotube, (d) nanobelt, (e) hierarchical structure, (f) nanorod and (g) nanoring [69].

According to the literature [70,71], it was reported that for gas sensing applications, nanowires (nanoneedles, nanofibers) are the most used form between all the studied one-dimensional nanostructures (40 %) followed by nanorods, nanotubes and nanobelts with nearly 20% per each form (see Figure II.5).

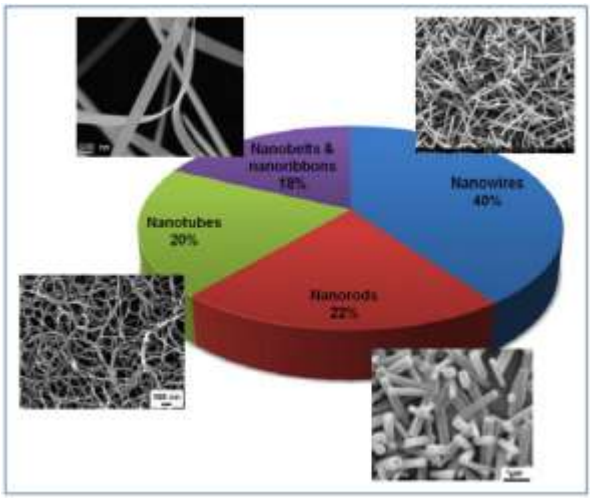

Figure II. 5. Morphology of the key one-dimensional nanostructures in gas chemiresistors (internet search of Web of Knowledge) [70].

Various metal oxide materials were successfully nanostructured and used for gas sensing applications and among them, 1D tungsten oxide has received much attention. Table II.3 lists some of the published works based on 1D tungsten oxide for gas sensing applications.

Table II.3. Some of the published works based on 1D tungsten oxide for gas sensing applications.

Mater	method of the growth	Target gas	Ref
Nanoneedles			
WO_3	AACVD	NO_2, H_2, EtOH, H_2S, CO, C_6H_6	[72-74]
WO_3	Electric field AACVD	NO_2	[75]
WO_3:Pt	AACVD	H_2, H_2S	[1,11, 76]
WO_3:Au	AACVD	Ethanol	[11,73]
Nanowires			
WO_3:CuO	Thermal evaporation	H_2S	[77]
WO_3:Pd	close-spaced chemical vapor deposition (CSVT)	H_2, Isopropyl, Methane, Acetone, Xylene	[78]
WO_3	Thermal evaporation	NO_2	[79]
WO_3	Hydrothermal method	NO_2	[80]
WO_3	Solvothermal method	NO, NO_2	[81]
WO_3	Thermal evaporation	NO_2	[82]
WO_3	hot-filament chemical	N_2O	[83]

	vapour deposition (HF-CVD)		
Nanorods			
WO_3	Hydrothermal method	NO_2	[84]
WO_3	CVD	NO_2	[85]
WO_3:TiO_2	Hydrothermal Method	acetone, ethanol, ether, methanol and formaldehyde	[86]
WO_3	Hydrothermal Method	Acetone	[87]
WO_3:C	Angle RF sputtering	NO_2	[88]
WO_3:Nb_2O_5	Hydrothermal Method	H_2, CH_4	[89]
WO_3:Au	ion-exchange + Hydrothermal	H_2	[90]
Nanofibers			
WO_3	Electrospinning	Acetone	[91]
WO_3	Electrospinning-Sol-gel	NH_3	[92]
WO_3	Electrospinning	NH_3	[93]
Nanotubes			
WO_3	Hydrothermal Method	Ethanol	[94]

2.3.1 Modified nanostructures

Despite the progress achieved by using 1D metal oxides in resistive gas sensors, the lack of selectivity and high working temperatures (250-350 °C) of metal oxides remain the biggest issues to overcome. In other words, metal oxides being poorly selective, they show responsiveness to a wide range of gases and such cross-sensitivity limits the widespread use of metal oxide gas sensors. Additionally, the high power consumption associated to the elevated operation temperatures, makes them unsuitable for battery operated sensor devices. Thus, to overcome these drawbacks, several research groups have shown that the addition of metal nanoparticles into the semiconductor metal oxide matrix (i.e. functionalization) helps dealing with the reported problems. They have corroborated this fact, pointing out the importance of using metal nanoparticle of reduced sizes< 5 nm and low concentrations of metal nanoparticles [14], which are thought to have a greater influence on the electronic structure of the support, in

creating new adsorption sites and show higher reactivity. It was presented by Vallejos et al. that the incorporation of Pt nanoparticles in WO_3 host matrix has increased the sensitivity toward H_2 by a factor of 9 [11]. Moreover, Lin et al. investigated the gas sensing properties of SnO_2 nanowires before and after the functionalization with Pt nanoparticles [95]. They found that the addition of Pt metal strongly enhanced the gas-sensing performance, including high sensitivity, fast response, and high recovery speed. Matsushima et al. have studied the beneficial effect of PdO doping in the optimal working temperature of SnO_2 sensors [96]. At 194 ppm of H_2, the working temperature was shifted from 300 °C for unloaded SnO_2 layer, to 150 °C for PdO functionalized SnO_2 films, with an increase in the response by a factor of 7.

To understand the reaction mechanism of metal additives with the target gas, Yamazoe et al. reported the presence of two sensitization mechanism: chemical sensitization and electrical sensitization [19], which are shown in Figure II.6.

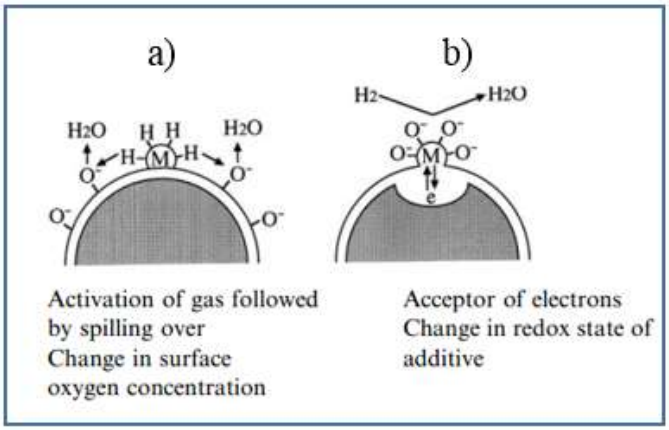

Figure II.6. Mechanism of sensitization by metal or metal oxide additive: a) Chemical sensitization and b) electronic sensitization [19].

In chemical sensitization, metal additives facilitate the activation of the target gas (in this example H_2) into H, and these later will be spill over to the semiconductor surface to react with the adsorbed oxygen. Hence, the additives are responsible in the enhancement of the reaction rate.

Electronic sensitization occurs due to the effect of metal additives on the space charge layer near to the metal oxide. At the oxidation state, the metal additives become strong acceptors of electrons from the metal oxide and start to induce the space charge layer near to the metal oxide, which is already depleted from electrons. When the target gas is in contact with the metal additives, the electrons are released again to the metal oxide and the space charge layer is relaxed. Thus this electronic interaction between the metal oxide and the metal additives is responsible for the enhancement of the gas response.

Various conceptual routes to functionalized 1D metal oxide nanostructures are available, based either on the synthesis and combination of the components separately (multistep) or by direct synthesis of the functionalized material (single-step). Palgrave et al. have reviewed the different strategies to incorporate or functionalize metal oxide nanostructures with metal additives [97]. They regrouped the methods in five routes of functionalization, as it is shown in Figure II.7. Route 1- synthesis of the metal oxide matrix in the first step then followed by the addition of the nanoparticles in the second step. In this way of functionalization, we can find spin coating and dip coating techniques, which they need the preparation of the solution nanoparticles. Route 2- synthesis of the metal oxide matrix in the first step then followed by the addition of metal ions in the second step. Example of this synthesis: Ion implantation and spin coating with a solution of metal ions followed by photocatalytic reduction or heat treatment. Routes 3- herein both the metal oxide matrix and the metal nanoparticles are synthetized in a single step. Examples include multitarget magnetron sputtering deposition, chemical vapour deposition using a separate precursor for each phase and sol-gel using a semiconductor and nanoparticle precursors. Route 4- in this category, the synthesis is made by multi-layer deposition (layer-by-layer) of metal oxide matrix and the metal nanoparticles. As an example; we find laser ablation technique, which use alternate metal and semiconductor targets. Route 5-

in-situ surface functionalization or deposition of metal nanoparticle/semiconductor composite thin films.

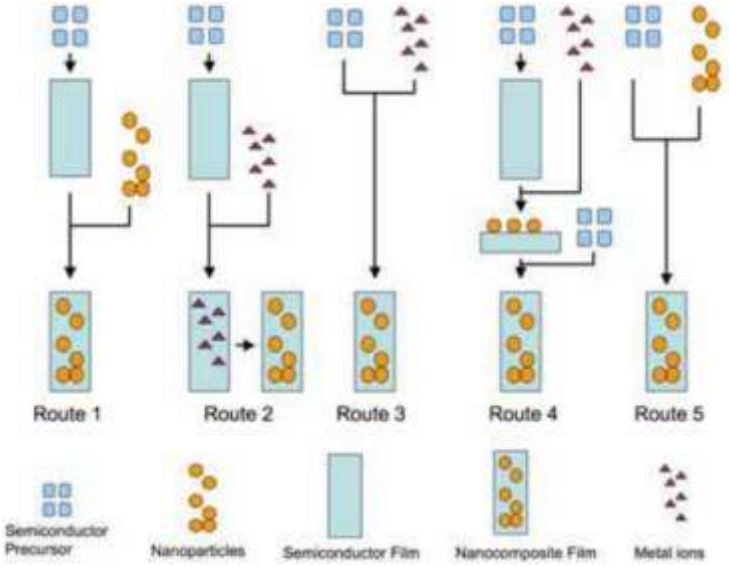

Figure II. 7. Routes to nanocomposite thin films [97].

2.3.2 Deposition techniques for 1D metal-oxides gas sensors

It is well known that the size and the shape of 1D metal oxide nanostructures can affect strongly their physical and chemical properties. Consequently, the choice of the technique used for their synthesis with goals of identical shape, uniform size, perfect crystal structures and homogenous stoichiometry remain important details to be taken into account. Various methods have been developed and successfully employed to produce 1D metal oxide nanostructures. These can broadly be classified into two categories: i) direct physical deposition methods ii) direct chemical deposition methods [12]. Most of the methods included in the first category are in line with the "top-down" approach, while the direct chemical deposition methods are used for the "bottom-up" approach. In the top-down approach, the method are usually based in the etching and lithography of the bulk materials to form functional devices at the nanometre scale. However, in the bottom up approach, the synthesis of the nanostructures is based in the assembly of well-defined chemically synthesized building blocks; the synthesis commenced from the

bottom: atom-by-atom, molecule-by-molecule and cluster-by-cluster. It is worth nothing that each method has its merits and disadvantages for the synthesis of 1D metal oxide nanostructures. In this section, we briefly describe some of the physical and chemical deposition methods used for the synthesis of 1D metal oxide nanostructure.

2.3.2.1 Direct physical deposition techniques

Thermal evaporation or physical vapour deposition (PVD) is one of the widely used route for the synthesis of 1D metal oxide nanostructures. In this technique, elevated temperatures and high vacuum environment are very important. As it is shown in Figure II.8, the bulk metal oxide material is placed inside the tube furnace. At high temperature, the atoms or molecules of the bulk material started to escape from its surface and sublimate into metal oxide vapour. When this later reaches to the substrate, it starts to condense in the form of 1D metal oxide nanostructures [12].

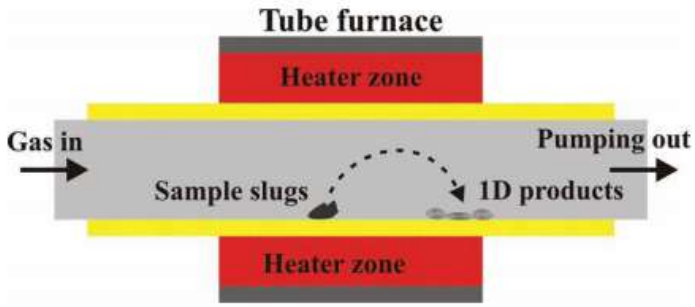

Figure. II. 8. Schematic diagram of tube furnace for synthesis of 1D nanostructures [12].

Molecular beam epitaxy, sputtering, and laser ablation are also variants of PVD technique [12]. In molecular beam epitaxy and laser ablation, the metal oxide vapour is produced by the high energy of the photons and electrons that are normally focused toward the surface of the bulk material. In contrast, for sputtering deposition, the metal oxide vapour is sublimated by the bombardment of the bulk oxide surface with argon ions.

Template based synthesis is one of the physical direct deposition techniques [12]. It is based on the confinement growth of nanomaterial in the 1D freedom nanoscale space. It has become one of the common methods for the synthesis of 1D metal oxide nanostructures due to their easy fabrication process. Various templates were successfully used and reported in the literature; for instance, porous anodic aluminium oxide (AAO) plates.

Electron-beam lithography, focused-ion-beam lithography, and dip-pen nanolithography have also been used and reported for the synthesis of 1D metal oxide nanostructures [12]. They belong to the top-down approach. They have demonstrated their capability to fabricate a large scale of well aligned metal oxide nanostructures, with well-defined bodies. In addition they have open a new pathway for the fabrication of various designed-geometries on solid substrates. Moreover, it was reported that lithography techniques can be used for the fabrication of specific geometry templates for the growth of 1D metal oxide nanostructures. For example, the growth of 1D metal oxide material on preferential sites, such as V-grooves [12], cleaved edges [12] and step edges [12]. Besides the advantages shown by these methods, the high costs and prolonged preparation times are the major drawbacks still to be overcome.

2.3.2.2 Direct chemical deposition methods

Chemical vapour deposition is a generic name of various techniques that involve the growth of solid material from a gaseous phase. CVD techniques include atmospheric-pressure, hot-filament, thermal-active, metal-organic, microwave-plasma, plasma-enhanced, low-temperature, aerosol assisted and photo-assisted types [12]. Their basic principle lies in the dissociation and the reaction of the volatile precursors at the surface of the heated substrate, using specific flow rates and different pressures to produce the desired material. CVD techniques have demonstrated in many reported works, their capability to produce high performance nanostructure materials with high quality and excellent purity. In this thesis, the synthesis of the 1D metal oxide material

were obtained by aerosol assisted CVD method, which will be described and detailed in the next section.

Hydrothermal and Solvothermal techniques are important branches of inorganic synthesis. The difference between the two techniques being in the precursor solutions [12]. In hydrothermal method, the synthesis occurs in aqueous solution above the boiling point and under high pressure. On the other hand, for solvothermal technique, the reaction happens in a solvent solution at moderate temperature and also under high pressure. For both the reported techniques, the reaction takes place in a stainless still autoclave. It involves the addition of metal organic precursors and suitable reagents to either water or solvent solutions, depending to the used technique. Various 1D metal oxide nanostructures were grown by using the reviewed methods [12]. Furthermore, it was reported that for solvothermal synthesis, the control of the shape, the size and the crystallinity of the produced 1D nanostructures can be realized by varying the working temperature, the reaction time, the solvents and the precursors employed.

Sol-gel is a wet-chemical process, usually used for the synthesis of thick films. However, in recent years, many works have investigated this technique for the fabrication of 1D metal oxide nanostructures [12]. It involves the preparation of a sol, which is a colloidal solution of integrated inorganic networks. After that, the formation of a gel, which is obtained after the drying of the sol. The precursors used in the preparation of the sol are often alkali metal oxides or metal salts and the liquids are water or diluted acids. Figure II. 9 illustrate the growth of 1D metal oxide nanostructures using sol-gel technique. As it is shown by Figure II.9. a and b, the colloidal solution (sol) is prepared by dissolution of the alkali metal oxide or metal salts in solvents and then placed in a spinning substrate. After that, the precursors start to undergo various process of hydrolysis and condensation reactions. As the sol starts to gelatinize, the colloidal suspension starts to gather and forms the 1D metal oxide nanostructure (i.e. the self-

assembly effect). Finally, by heating the gel, the residue of water or diluted acid is removed and the 1D metal oxide nanostructures are obtained (see Figure II.9.c).

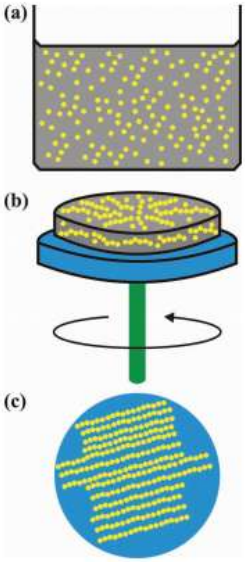

Figure II.9. Schematic diagrams of the sol-gel technique: a) the colloidal suspension in the sol is represented by yellow spots; b) sol is spun to form a gel; and c) after the heat treatment 1D metal-oxide nanostructures grow on the substrate [12].

2.3.2.3 Growth mechanism of 1D metal oxide nanostructures

Either in physical or chemical deposition techniques, the growth mechanism of 1D metal oxide nanostructures is essentially based in the following points [12]:

- Physical or chemical reactions
- Nucleation
- Assemblies
- Crystallization

The physical and chemical reactions are directly related to the experimental setup. Thus any change in the reaction can strongly affect the next step which is the nucleation. This later plays a primordial role in the growth of the nanostructures, since it can be considered as seeds of the growth. Their size, number and shape have huge effects in the assembly of the atoms, molecules

and ions. Finally, from the assemblies, we can conclude the crystallinity and the morphology of the synthetized 1D metal oxide nanostructure [12].

Overall, based on the four cited points, the growth mechanism of 1D metal oxide nanostructures can be divided into three essential mechanism: vapour-liquid-solid (VLS), vapour-solid (VS), and solution-liquid-solid (SLS) growth mechanisms [12].

VLS mechanism: herein the catalysts are an important factor for the growth of 1D metal oxide nanostructures. They are considered as sites for adsorbing the reactive vapours. Figure II.10 displays the schematic representation of the VLS mechanism. First, the metallic particles are deposited on the top of the substrate (Figure II.10.a). After that, at a certain temperature, the metallic particles become eutectic alloys with the reactive vapours (Figure II.10.b). By the continuous delivery of this later, the liquid alloys become supersaturated and at this point the growth of the nanostructures begins (Figure II.10.c). Finally, the growth will continue as long as the alloy remains liquid and the reactive vapour is delivered. Consequently, the obtained 1D metal oxide nanostructures from VLS mechanism have a catalyst particle in their end with sizes usually comparable to their diameter (Figure II.10.d) [12].

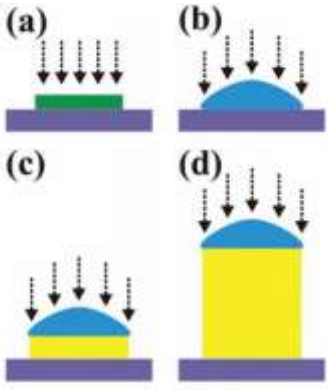

Figure II.10. Schematic diagrams showing the VLS growth mechanism [12].

VS mechanism: It is also called self-catalyst mechanism, since there is no need for the catalyst to assist in the synthesis of the material. Thus, only the vapour phase and the solid phase

are contributing in the growth of 1D metal oxide nanostructures, and the crystalline solids assemble the material directly from the vapour phase [12].

SLS mechanism: the studied mechanism is one of the favourable approaches for the growth of metal oxide nanostructures with high quality and well controlled morphology. It is similar to the VLS mechanism. The only difference lies in the growth inside an active solution, as it is indicated in Figure II.11.

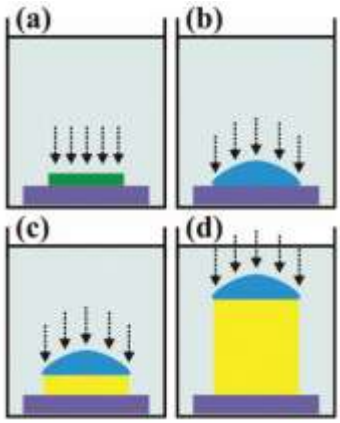

Figure II.11. Schematic diagrams of the SLS growth mechanism. The metallic particles (highlighted in green) are used as catalytic seeds to become liquid eutectic alloys (highlighted in blue), when the active solution (represented by dashed arrows) is continuously supplied. The 1D nanostructure (highlighted in yellow) grows during the solute saturations [12].

2.4 Aerosol assisted chemical vapor deposition (AACVD) method

Given its simplicity, its relative low cost of setting and operation and its scalability, AA-CVD is an industrially attractive technique. Since the technique runs at atmospheric pressure, the deposition rate is typically several orders of magnitude higher than that of high vacuum techniques, which has a direct impact on the energy required per gram of produce. Unlike in conventional CVD, where precursors must be volatile and thermally stable, AACVD allows for

the use of a wide range of precursors owing to its solution-delivery based principle. Furthermore, the AACVD process is conducted at lower temperatures than CVD, typically in a range between 350 and 600 ºC, which makes it suitable for the direct, bottom-up integration of gas-sensitive nanomaterials onto a wide spectrum of substrates including glass, ceramic, silicon micro electro-mechanical systems (MEMS) or even flexible polymeric.

AA-CVD offers a useful route to produce films, coatings, and other CVD products, when the precursors for conventional CVD prove to be non-volatile or thermally unstable for synthesising the specific materials [97,98]. Via this method, the synthesis of nanostructures, the decoration with metal nanoparticles and the integration in the structure of a device take place in a single step of the process and, this is not only industrially advantageous but also represents a more environmentally sustainable way of producing nanodevices. The AA-CVD technique possesses several advantages that are not always found in other techniques often employed in the fabrication of nano/microsensors. Among these, its flexibility for depositing different metal oxides and nanoparticles of different metals, high deposition rate, which may be obtained from a high mass-transport rate of the precursor, and the possible improvement of precursor selection. Additionally, it offers a more flexible reaction environment, since AA-CVD can be operated under low pressure, atmospheric pressure, or even in an open atmosphere [99-101]. The technique is low cost and compatible with Microsystems technology.

2.4.1 Basic principal of AACVD

AA-CVD is based on the atomisation of a liquid precursor solution into fine sub-micrometre-sized aerosol droplets. These later are transported by a flow of a carrier gas to the heated reaction zone. At the increased temperature, the solvent undergoes rapid evaporation and/or decomposition, forming the precursor vapour. After that, the precursor vapour is transported to the heated substrate and there it starts to react and decomposes to form the desired

product. Concerning the exhaust, it is vented via an extraction system [98-102]. A schematic representation of AA-CVD process is given by Figure II.12.

If the aerosol droplet reaches the heated substrate before complete evaporation and vaporisation, a spray pyrolysis process will take place rather than a true CVD reaction [98].

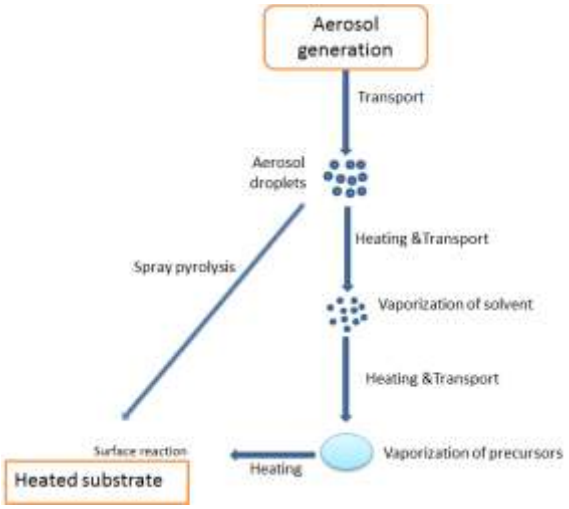

Figure II. 12. A schematic representation of the basic principle of the AA-CVD process.

In the heated zone, two kinds of chemical reactions may occur to form the desired materials: heterogeneous reaction and/or homogeneous reaction. Heterogeneous reaction involves the decomposition of the vaporised precursor in the gas phase, followed by the adsorption and the reaction of these vapours onto the surface of the heated substrate. However, homogenous reaction happens when the temperature is too high and an earlier decomposition and/or chemical reaction of the precursor vapour will take place. As a result, homogeneous nucleation with fine particles are formed and can undergo heterogeneous reaction on the surface of the substrate, forming porous films. In the AA-CVD process, the presence of solid particles in the gas phase affects the quality and the properties of the deposited films, impacts the deposition rate and changes their morphology [98].

The major criteria for the selection of solvents are high solubility of the precursor, low vapour pressure and low viscosity. The atomisation of the precursor solution can be realised by using different types of aerosol generators such as pneumatic aerosol jet, electrostatic atomisation and ultrasonic aerosol generation. Ultrasonic generation is the option adopted in our application. Concerning the carrier gas, nitrogen and argon are the most commonly used inert carrier gases. Compressed air is used for the deposition of oxide products, while reactive gases such as H_2 may also be used with other primary carrier gases to help the CVD reaction [98].

2.4.2 Aerosol-assisted CVD – applications for gas sensors

In the last 10 years, many works have been devoted to the study and improvement of the synthesis of metal-oxide nanostructures by using AA-CVD as an alternative method to conventional CVD. Owing to its delivery system, a wide range of metal oxides were deposited, such as WO_3, ZnO, TiO_2, SnO_2, InO_2, Ga_2O_3, Cr_2O_3, etc. In addition, various nanostructures were successfully obtained including nanoneedles, nanowires, nanorods, nanofibers and nanotubes. Apart from this, AACVD has demonstrated its capability to grow in a single step deposition nanocomposites films such as Au /TiO_2, Pt/WO_3, Au/WO_3, etc. In Table II.4, examples of the successful growth of either pure or functionalize metal-oxide active sensing materials by using AACVD methods are presented.

Table II.4. Summary of successful growth of a pure and functionalize metal-oxide active sensing materials by using AACVD methods.

Active material	Material morphology	Sensor Substrate	Target gas	refe
WO_3	Polycrystalline Nanoneedles	MEMS	NO_2, H_2, EtOH, , CO, C_6H_6	[72]
Pt/WO_3 Au/WO_3, Au/Pt/WO_3	Nanoparticles/ Nanoneedles	MEMS	EtOH, CO, H_2, H_2S	[11]

Cu/SnO_2	Clusters	Alumina	H_2S	[102]
SnO_2	Nanoparticles	Alumina	NO_2	[103]
In_2O_3 Ta/In_2O_3 Ti/In_2O_3	Clusters	Alumina	EtOH	[104]
TiO_2	Spherical particles	Alumina	EtOH	[105]

Chapter 3: Experimental section

3.1 Film deposition

In order to fabricate the sensing element, pure and functionalized WO_3 nanoneedles (NNs) were deposited via aerosol assisted chemical vapour deposition (AACVD). The growth was performed in two different reactors which will be detailed in this section.

3.1.1 AACVD reactors

In the AACVD technique, both hot and cold wall reactors can be used. A hot wall reactor, is when the entire reactor chamber is heated and the deposition occurs on the top of the substrate as well as on the reactor walls. In contrast, in a cold wall reactor, the substrate is the only part of the whole apparatus that is heated and growth occurs only on the heated substrate. During this thesis, we have used both types of reactors for the growth of the sensing layers.

3.1.1.1 Hot wall reactor

This AACVD reactor was fabricated in our workshop. It was made from two stainless steel cylindrical pieces. One is the cover and the other one is the base of the reactor. Figure III.1 represents a detailed schematic drawing of the reactor chamber. As it is shown, each cylindrical piece has a diameter of 95 mm and a height of 20 mm. Two heater cartridges (8 mm - diameter, 23.45 W/cm^3 WATLOW) were integrated in parallel under the substrate placement, and a type K thermocouple (1.6 mm - diameter and 152 mm - length, WATLOW) was vertically introduced under the substrate placement too. Furthermore, the reactor inlet was positioned horizontally on the cover, while the outlet or the exhaust was positioned vertically from the base. In addition, the distance between the substrate and the cover was

about 7 mm. For the control of the reactor temperature, a PID power controller (EUROTHERM, model 3216) and a temperature controller (single-phase thyristor unit, EUROTHERM, model 7100A) were connected to the deposition system. It is worth noting that the maximum temperature that could be reached by the heating system was up to 650 °C.

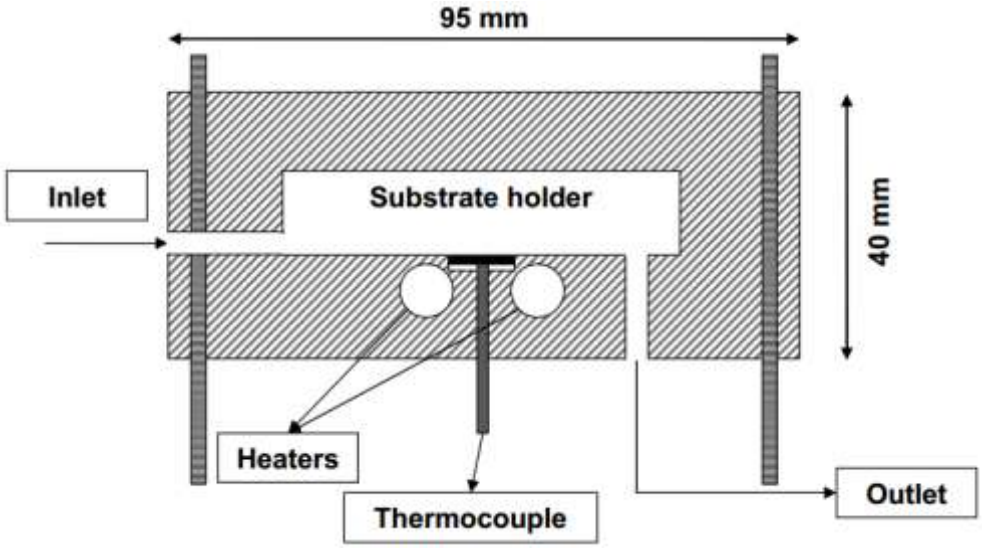

Figure III.1. Schematic drawing of the reactor chamber.

Figure III.2 displays the experimental set up of the AACVD system. The liquid precursor solution is usually contained in a round glass flask (250 mL capacity, Afora). The cover of this glass flask is fitted with two small tubes made from PTFE material. One is used to introduce the carrier gas and the other one is connected to the inlet of the reactor. To convert the precursor solution to an aerosol, i.e. to generate small droplets of the precursor and solvents, the flask was immersed and positioned in the centre of an ultrasonic atomizer tank (frequency ~1.5 MHz, CHICCO), containing 300 mL of water. As it was mentioned in the previous chapter, the formation of an aerosol is required for the AACVD delivery process mechanism. The produced aerosol was then transported via the carrier nitrogen gas (N_2 Premier, Carburos Metálicos) into the heated zone inside the reactor, where the substrate is placed. The gas flow was controlled by using the needle valve of a gas flow meter (Key

Instruments, model 3A14), with measuring range of up to 5 L/min ±4%. All gas-handling lines were made of PTFE material with 3.45 mm internal and 6.35 mm external diameter. All the AACVD experiments were performed inside a fume-cupboard.

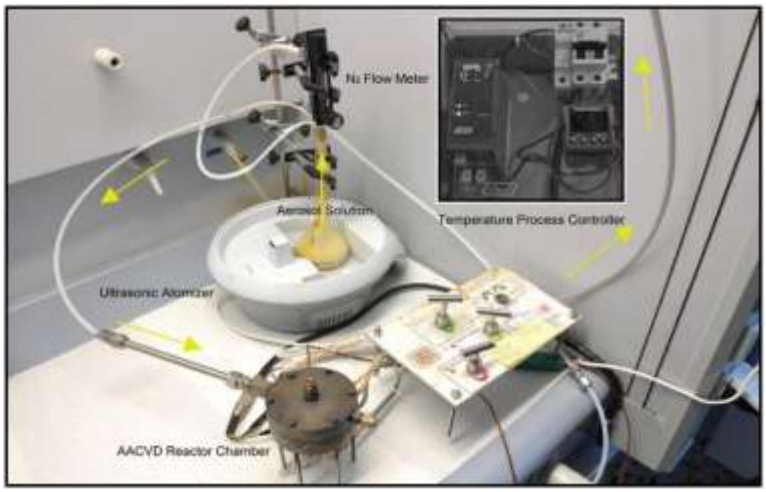

Figure III.2. AACVD experimental set up.

3.1.1.2 Cold wall reactor

The cold wall reactor was totally different from the hot wall one. It was made from Teflon and it had a holder in which the sensor substrate was inserted (see Figure III.3). The direction of the gas flow was horizontal to the substrate. The inlet and the outlet were at the same level as the sensor substrate and the distance between this later and the reactor cover was 6 mm. Furthermore, the temperature was generated by the sensor heating element, which was connected to an external power supply. The required growth temperature was reached and kept by applying a constant voltage to the heating element. In addition, during the deposition, the reaction chamber was maintained at room temperature.

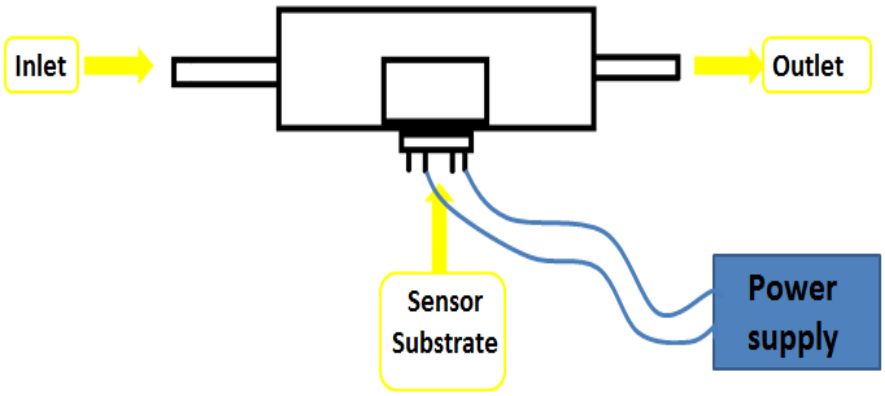

Figure III.3. A schematic representation of a cold wall reactor.

The reactor design is strongly dependent on the configuration of the sensor substrate used. Accordingly, we have fabricated two different reactors, since we have used two different sensor substrates: alumina and silicon micro hotplate (MEMS) sensors.

a) Cold wall reactor adapted for alumina gas sensors

Figure III.4 displays the picture of the AACVD cold wall reactor adapted for alumina sensor substrates. It was made from a single piece of Teflon, with dimensions of 57 mm × 41 mm × 22.5 mm. Furthermore, it has a sensor holder in the back with a diameter of 15 mm and a printed circuit board was used to connect the sensor heater to the external power supply. Moreover, the reaction chamber design (i.e. inside the reactor) has a shape of a cone and the diameter of the inlet was the double of the one of the outlet. This specific design was made with the aim to retain for as long as possible the precursor mist inside the reaction chamber.

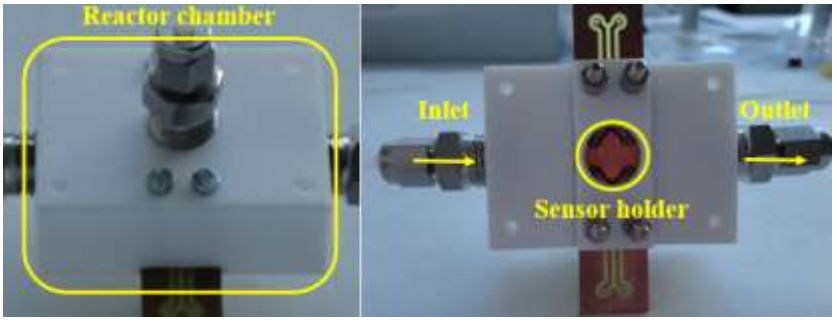

Figure III.4. AACVD cold wall reactor adapted for alumina sensor packaging.

b) Cold wall reactor adapted for MEMS-based gas sensors

The second cold wall reactor is shown in Figure III.5. It was designed for the use of MEMS sensors. The reactor was made from Teflon. It consists of two rectangular pieces with dimensions of 50 mm × 37 mm per each, used as the base (bottom) and the cover (top) of the reactor. The inlet and the outlet were positioned horizontally in the cover. The distance between the sensor substrate and the cover was about 6 mm. In order to generate the temperature necessary for the reactions, a PCB was connected to the sensor holder, at the bottom of the reactor.

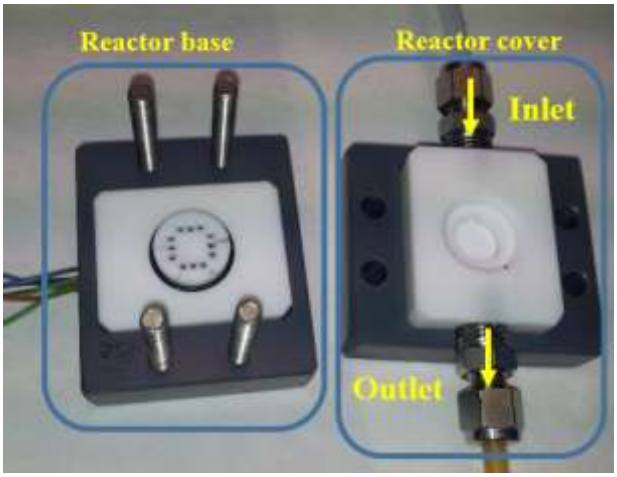

Figure III.5. AACVD cold wall reactor adapted for MEMS sensor packaging.

It is worth noting that exception made of the reactor chamber, which changes for the cold wall or hot wall set-up, the remaining experimental set-up is identical for both systems and equal to the one described above in section 3.1.1.1.

3.1.2 Precursor characteristics

For the synthesis of WO_3 layers, we have used two different precursors: commercially available tungsten hexacarbonyl and lab-made tungsten hexaphenoxide.

Tungsten hexacarbonyl [$W(CO)_6$], with a white colour and 97% purity, was purchased from sigma-Aldrich. It has the appearance of small powder or crystallites and it is toxic if swallowed, in contact with skin or if inhaled.

Tungsten hexaphenoxide [$W(OPh)_6$] (Ph = C_6H_5), with a dark red colour, was obtained from the reaction of tungsten hexachloride in toluene (250 cm^3) and Phenol (14.1 g, 0.150 mmol) under nitrogen atmosphere using standard Schlenk techniques [106]. The resulting product was recrystallized in ether (200 cm^3) and washed with ca. 5% NaOH (3x100 cm^3) to remove the entire undissolved residue. After that, the ether was removed by using a vacuo and the obtained red solid was dissolved in acetonitrile and then filtered. Detailed studies of the synthesis, crystallography and element analysis of this precursor are reported in [106-107].

Table III.1. Summary the crystallographic data of [$W(CO)_6$] and [$W(OPh)_6$].

Crystallographic data	Tungsten hexacarbonyl	Tungsten hexaphenoxide
Empirical formula	C_6O_6W	$C_{36}H_{30}O_6W$
Formula weight	351.9	742.45
Form	solid	solid
Density (g/L)	$2.65\ 10^3$	$1.6\ 10^{-6}$
Melting point °C	150	n/a

3.1.3 Active sensing layer deposition

3.1.3.1 General procedure

All chemicals were used as received without further purification. For the preparation of the precursor solution, three simple steps were followed:

First, a specific quantity of a solid precursor should be weighed using an analytical balance (resolution 0.1 mg, A&D Instruments, model GR-120-EC) and then kept in a glass flask.

After that, an organic solvent or a mixture of solvents should be added to the solid precursor. The solvent was weighed in a graduated cylinder (graduation 1 mL, Duran). Finally, the flask should be placed in an atomizer bath for 10 to 15 min depending on the solubility of the precursor used. In Table III.2 the properties of the organic solvents and the precursors used in this work are presented.

Table III.2. Properties of the organic solvents and the precursors used in this work.

Properties	Organic Solvents				Precursors				
	Acetone	Toluene	Methanol	Chloroform	Gold(III) chloride hydrate	Chloroplatinic acid hydrate	copper (II) acetylacetonate	Palladium(II) acetylacetonate	Ammonium hexachloropalladate(IV)
Provider	Sigma-Aldrich	Sigma-Aldrich	Sigma-Aldrich	Sigma-Aldrich	Sigma-Aldrich	Sigma-Aldrich	Sigma-Aldrich	Sigma-Aldrich	Sigma-Aldrich
Purity, %	99,8%	99,8%	99,6%	≥99%	99.999%	≥99.9%	97%	99%	99.99%
Molecular formula	C_3H_6O	$C_6H_5CH_3$	CH_3OH	$CHCl_3$	$HAuCl_4•3H_2O$	$H_2PtCl_6•xH_2O$	$C_{10}H_{14}CuO_4$	$C_{10}H_{14}O_4Pd$	$H_8C_{l6}N_2Pd$
Molar mass (g/mol)	58.08	92.14	65	119.38	339.79	409.81	261.76	304.64	355.21
Boiling point (°C)	56	110-111	32.04	60.5-61.5	----	----	----	----	----

Before starting the AACVD process, the substrate was cleaned with ethanol (Sigma-Aldrich, ≥99.6%) and then with acetone (Sigma-Aldrich, ≥99.6%), dried with air (Premier, ≥ 99.99%) and then placed inside the reactor, which should be securely closed. After this, the temperature controller was adjusted at the growth temperature and the precursor solution, which was kept in a glass flask, was placed in the ultrasonic atomizer tank. When the desired temperature was reached, the nitrogen carrier gas was allowed to flow through the reaction chamber and the ultrasonic atomizer was switched on. In that way, the aerosol generated (i.e. small droplets of precursor and solvents) was transported to the reactor heated zone via a nitrogen gas flow and there it started to evaporate and decompose. The exhaust was vented directly into the extraction system of a fume cupboard and the deposition continued until all the precursor had passed through the reactor. Finally, the temperature controller and the ultrasonic atomizer would be switch-off and the nitrogen flow was maintained until the reactor had cooled down to room temperature.

In the case of a cold wall reactor, the temperature was generated by applying a constant voltage to the sensor heater. Since, a rather high growth temperature was needed (i.e. up to 600 °C), the voltage should be increased slowly to avoid the destruction of the sensor heating element. Similarly, when the AACVD process was finished, the voltage source should be reduced gradually.

For the hot wall reactor, the nitrogen flow usually was set at 0.5 L/min, while in a cold wall reactor, it was varied between 0.2 to 0.4 L/min, depending on the reactor used. In Table III.3 we summarise the general conditions required for the growth of all the sensing layers produced in this thesis work.

Table III.3. General conditions required for the growth of all the sensing layers produced in this thesis work.

Reactor used	Sample name	Main precursor		Functionalizing precursors		Deposition temperature (°C)	Nitrogen Flow (L/min)	Substrate	Deposition time (min)
		Precursors (mg)	Solvent (mL)	Precursors (mg)	Solvent (mL)				
Hot wall reactor	WO_3 NNs	$W(OPh)_6$);150	A 12.5+ T; 12.5	----	----	450	0.5	Alumina sensors-1	45
	Pt NPs/WO_3 NNs	$W(OPh)_6$);150	A; 25	($H_2PtCl_6 \cdot xH_2O$); 10	M; 5	350	0.5	Alumina sensors-1	45
	Au NPs/WO_3 NN_S	$W(OPh)_6$);150	A; 25	($HAuCl_4 \cdot 3H_2O$); 10	M; 5	350	0.5	Alumina sensors-1	45
	WO_3 NPs	$W(CO)_6$; 25	A;7 + M, 3	----	----	380	0.5	Polymeric micro-hotplate	20
	Pt NPs/WO_3 NNs	$W(CO)_6$; 25	A; 9	($H_2PtCl_6 \cdot xH_2O$); 3.6	M; 3	380	0.5	Polymeric micro-hotplate	20
	Au NPs/WO_3 NNs	$W(CO)_6$; 25	A; 9	($HAuCl_4 \cdot 3H_2O$); 3.6	M; 3	380	0.5	Polymeric micro-hotplate	20

	WO_3 NNs	$W(CO)_6$; 50	A; 15 + M; 5	----	----	500	0.5	MEMS Micro-hotplate	45
	Cu_2O NPs/WO_3 NNs	$W(CO)_6$; 50	M; 16	$Cu(acac)_2$; 7	C; 4	380	0.5	MEMS Micro-hotplate	45
	Pd/WO_3(Ac-1SD)	$W(CO)_6$; 50	A; 15	$Pd(acac)_2$; 5	M; 5	400	0.3	Glass	45
	Pd/WO_3(Am-1SD)	$W(CO)_6$; 50	A; 15	$(NH_4)_2PdCl_6$; 5.8	M; 5	400	0.3	Glass	45
	Pd/WO_3(Ac-2SD)	$W(CO)_6$; 50	A; 15 + M; 5	-----	----	500	0.3	Glass	45
		-----	-----	$Pd(acac)_2$; 10	M; 10	400	0.3		20
	Pd/WO_3(Am-2SD)	$W(CO)_6$; 50	A; 15 + M; 5	-----	----	500	0.3	Glass	45
		-----	-----	$(NH_4)_2PdCl_6$; 11.5	M; 10	400	0.3		20
	WO_3	$W(CO)_6$; 50	A; 15 + M; 5	-----	----	500	0.3	MEMS Micro-hotplate	45
	Pd/WO_3(Ac-1SD)	$W(CO)_6$; 50	A; 15	$Pd(acac)_2$; 5	M; 5	400	0.3	MEMS Micro-hotplate	45

	Pd/WO_3(Ac-2SD)	$W(CO)_6$; 50	A; 15 + M; 5	-----	----	500	0.3	MEMS Micro-hotplate	45
		-----	-----	$Pd(acac)_2$; 1.5	M; 5	400	0.3		16
	Pd/WO_3(Am-2SD)	$W(CO)_6$; 50	A; 15 + M; 5	-----	----	500	0.3	MEMS Micro-hotplate	45
		-----	-----	$(NH_4)_2PdCl_6$; 2.2	M; 5	400	0.3		16
Cold wall reactor	WO_3 NNS	$W(OPh)_6$; 40	A; 4 + T; 4	-----	-----	550	0.35	Alumina	20
	WO_3 NNs	$W(CO)_6$; 20	M; 5	-----	-----	580		MEMS Micro-hotplate	45
	Pt NPs /WO_3 NNs	$W(CO)_6$; 20	M;5	$(H_2PtCl_6 \cdot xH_2O)$; 1	-----	580	0.2	MEMS Micro-hotplate	45
	Au NPs/ WO_3 NNs	$W(CO)_6$; 20	M;5	$(HAuCl_4 \cdot 3H_2O)$; 1	-----	580	0.2	MEMS Micro-hotplate	45

Legend: A: Acetone; M: Methanol; T: Toluene.

3.1.3.2 Annealing process

After the AACVD depositions, all substrates were subject to an annealing at high temperature in the presence of air. For samples produced by hot wall reactor, the substrates were kept inside a horizontal tube furnace (Carbolite model GHA, max.temp.1200 ºC), at a temperature of 500 °C during 3h. The typical temperature profile applied during the annealing is shown in Figure III. 6. Air flow was fixed at 200 ml/min.

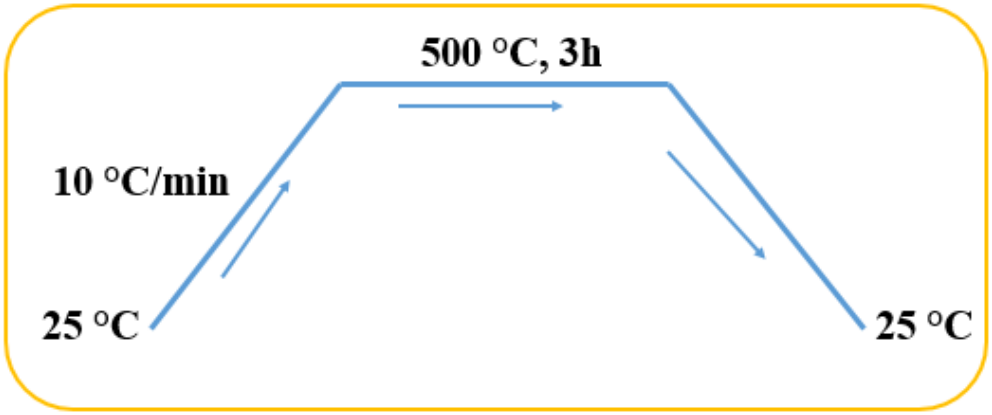

Figure III.6. A typical temperature profile used for conducting the annealing of samples.

Regarding the samples obtained by cold wall reactor, a localized annealing i.e. using the heater of the sensor, was carried out at 580 ºC for 2 h with a constant flow of synthetic air (50 sccm, Praxair, 99.99%). The annealing of the films was performed in order to clean the surface from deposition residues and to stabilize and crystallise the structure of the nanomaterials grown.

3.2 Material characterization

Surface morphology of the samples was investigated using a scanning electron microscope (SEM-FEI Quanta 600) and transmission electron microscopes (TEM Jeol JEM 1011, operating at 100 kV and Jeol 2100 operated at 200 kV) while the structure of the deposited film was studied by X-ray diffraction (XRD) (Bruker, AXD D8-Discover, using Cu

K α radiation operated at 40 kV and 40 mA) and RAMAN (Renishaw in Via, laser of 514 nm, ion argon — Novatech, 25 mW).

The elemental and chemical composition determination were performed by X-ray photoelectron spectroscopy (XPS) (Physical Electronics, VERSAPROBE PHI 5000, using monochromatic Al K α radiation with 0.7 eV energy resolution; a dual-beam charge neutralizer composed of an electron gun (≈ 1 eV) and an argon-ion gun (≤ 10 eV) for charge compensation; all of the binding energies were calibrated to the C 1s peak at 284.5 eV).

To study the electronic structure of a single wire, near-edge x-ray absorption fine-structure spectroscopy (NEXAFS-TXM) was performed with the full-field transmission x-ray microscope installed at the undulator beamline U41-SGM at the electron storage ring BESSY II operated by the Helmholtz-Zentrum Berlin. The spectra were recorded at room temperature in a transmission mode by taking a sequence of images over a range of photon energies covering the investigated absorption edges with a spectral resolution larger than 5000. The used zone plate allowed a spatial resolution of 25 nm. The NEXAFS spectra were normalized since the photon flux varies as a function of photon energy (h·υ) and position in the object field (x, y). The normalization was performed by dividing the function I(x, y, h·υ) recorded on the sample by the photon flux curve I0(x+Dx, y+Dy, h·υ) recorded in its sample free proximity at position (x+Dx, y+Dy). Both I(x, y, h·υ) and I0 (x, y, h·υ) were recorded in the same image stack, since near each studied nanostructure bare regions permit the measurement of I_0.

3.3 Gas sensor fabrication

3.3.1 Alumina gas sensors-1

Sensor substrates were fabricated by thick-film technology onto alumina substrates. On the front side, interdigitate gold electrodes (with 700 µm electrode gap) were printed. A Pt heater and temperature sensing resistive meander were printed onto the backside. The procedure for the fabrication of these substrates is as follows. In the first step, interdigitate gold electrodes were deposited by using a commercial conductive paste (ESL 8884). Once printed, the substrates were left at room temperature for levelling, in order to eliminate defects in the structure before firing. After levelling, the substrates were dried (15 min at 125ºC) and fired in a belt-furnace during 1 h with a peak temperature of 950ºC. In the second step, a heating element and a temperature sensing meander were printed using a commercial platinum paste (Heraeus C3657). After levelling at room temperature, the substrates were dried (20 min at 150ºC). Gold pads were printed and the firing of the Pt-heater, the sensing resistance and gold pads were performed during 1 h. The peak temperature was set to 875ºC. Figure III.7 shows a picture of the substrate employed. After coating the electrode area with tungsten oxide nanoneedles, the substrates were wire bonded to a PCB employing an Ag soldering paste.

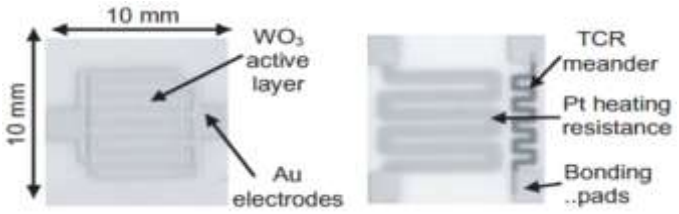

Figure III.7. Image of the sensor substrate prior to wire bonding and encapsulation. Left: Front side of the substrate with Au electrodes coated with WO_3 nanoneedles. Right: Backside of the substrate.

3.3.2 Flexible polymeric sensors

Flexible polymeric sensor substrates were also used in this doctoral thesis. They were fabricated at the EPFL-IMT SAMLAB, Neuchâtel, Switzerland. They consist of two different transducer designs, made employing different technologies.

a) Flexible polymeric sensors-1

The first one is depicted in Figure III. 8. It was fabricated by means of evaporation and lift off techniques. The substrate consisted of a fifty micrometre thick Upilex-50S polyimide foil from UBE Industries, Ltd. This material was chosen since it can withstand high temperatures up to 450 °C. The sensor consists of a double spiral shape-heater (Ti/Pt (20 nm/130 nm)) deposited on the substrate by sputtering and patterned by a lift-off technique. The heater resistance was ~101 Ω and the temperature coefficient was 1.7×10^{-3}/ºC. A 700 nm thick photo-definable polyimide layer was spin-coated on the top of the heating area to electrically insulate the heater from the electrodes. And finally, Ti/Pt interdigitated electrodes with a gap of 5 µm and square shape, were deposited on the top of the insulated film by sputtering and patterned by lift-off [108,109].

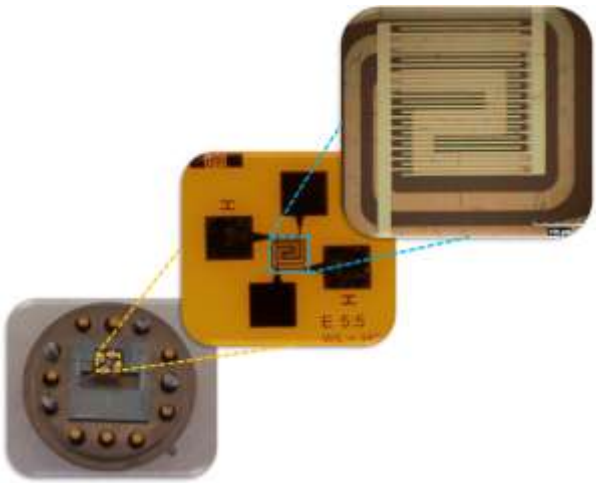

Figure III. 8. Photographs of the flexible polymeric gas sensor before and after wire bonding to a TO-8 package for testing.

For the connexion and the assembly of the sensor, a TO-8 package was used as it is shown in Figure III. 8. Firstly, four platinum wires with diameter of 50 µm were soldered to the pads of the sensor, using a liquid silver paste. After that, the assembled sensor was inserted in a ceramic dish and then in the oven, at 150 °C during 15 min. Finally, the sensor was held up by connecting the platinum wires to the pins of the TO-8 package, using a solder machine.

b) Flexible Gas sensor-2

The second type of the flexible polymeric transducer was fabricated by using inkjet-printing method. This sensor consists of interdigitated inkjet-printed gold electrodes, with an electrode area of 7530 µm x 2830 µm. The material substrate was Kapton 200EN polyimide film with a thickness of 50 µm. The novelty of this design is the simultaneous double functionality of the heater electrode, since it works as a heater and drains the sensing current at the same time. Whereas, the other electrode is used to read the current variations related to the atmosphere changes over the sensing surface. Figure III. 9 shows optical images of the obtained inkjet-printed two electrodes transducers. The heater resistance is 30 Ohms, the gap between the electrodes varies between 90 to 120 µm, while the width of both heater and electrode is 630 µm and 340 µm respectively.

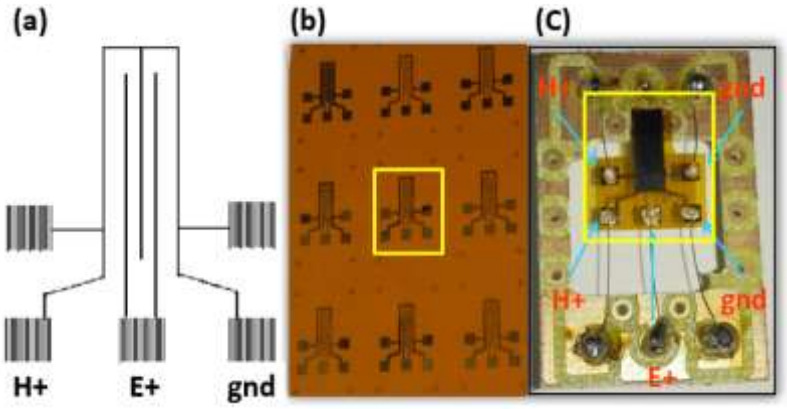

Figure III. 9. (a) Electrodes layout, (b) Various printed electrodes over Kapton film and (c) One sample device after AACVD deposition.

The sensor was connected to a printed circuit board (PCB) by using the assembly method described above (section 3.3.2.a). The PCB was fabricated in the workshop of the Department of Electronicss, its dimensions were 20 mm×25 mm. Moreover, the heater electrode has two additional pads, which can be used for implementing four-point resistance measurements if desired.

For the two types of flexible sensor substrates, a contact shadow mask was used to avoid the connexion between the pads of the heater and those of the electrodes during the growth of the sensing layer.

3.3.3 Alumina gas sensors-2

The alumina gas substrates were obtained from the School of Engineering and Materials Science, Queen Mary University of London (purchased from City Technology). Each substrate consisted of a 3×3 mm^2 alumina, with interdigitated Au electrodes on the front side and a Pt heating resistor on the back side. The heater resistance was ~5 Ohms and its temperature coefficient was 3.7 10^{-3} /°C. The electrodes were formed by laser trimming to produce an interdigitated section with a gap width of 150 µm and finger widths of 50 µm. Furthermore, the contacts were made by using platinum wires with diameter of 50 µm. They were spot-welded to the gold contacts and then used to suspend the sensor onto stainless steel pins in a moulded polyphenylene sulphide housing. Figure III. 10 displays a schematic of the alumina sensor transducer and a picture of a wire bonded to its package (b).

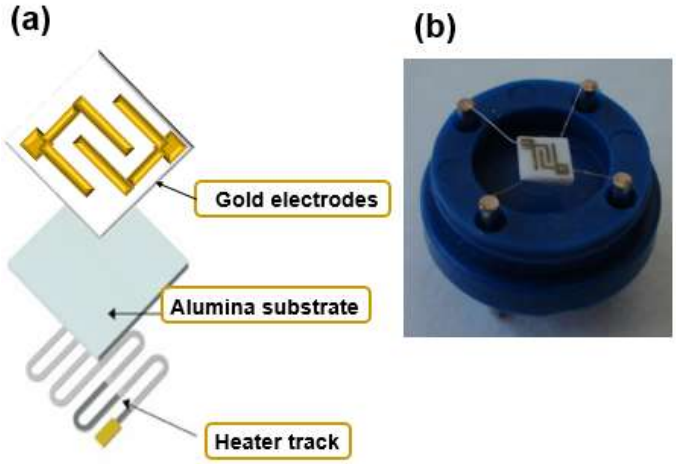

Figure III. 10. Schematic of the sensor transducer (a), photograph of the alumina sensors (b).

In this doctoral thesis, these sensors were employed in the cold wall reactor (the one described in section3.1.1.2.a) for the growth of metal oxide nanostructures. They were chosen due to their ability to reach very high temperatures without experiencing virtually any drift in their heating resistance. Indeed, platinum is one of the best materials for sensor heating elements, since it ensures the stability of the heater even at high operating temperatures (e.g. 600 °C).

Moreover, it should be noted that a dielectric layer (dielectric glaze 4913-G from ESL/Agmet) was painted to the heater track with the aim to avoid any contact between the heater and the grown WO_3 films.

3.3.4 MEMS-based gas sensors

MEMS-based microsensor platforms were fabricated in the clean room of the CNM (National Center of Microelectronics, Bellaterra Spain) using various microfabrication steps including implantation, photolithography, metallization, lift-off and rear side etching of the substrate to define the membranes. The design and fabrication of such substrates is not the object of this doctoral thesis.

Figure III.11 shows an array of microsensors implemented in a double side polished p-type <100> Si substrates with a 300 µm thickness. In one chip, four membranes with dimension of 1 mm × 1 mm, were grown via LPCVD technique. Each membrane comprised of a $POCl_3$-doped polysilicon meander shaped resistive heater and platinum electrodes, isolated by an interlevel silicon oxide layer (800 nm thick). The heater had a thickness of 0.47µm and resistance of 16 Ω/sq with temperature coefficient of 6.79×10^{-4}/ºC. The spacing between the interdigitated electrodes was 50 µm, the thickness of the fingers was 0.2 µm and the electrodes area was 400 µm × 400 µm. Each chip consisted of an array of four microsensors bounded and mounted on a standard TO-8 package [72]. Furthermore, to avoid the contact between the heater and the electrodes pads (contacts), a contact mask was used during the AACVD deposition (using hot wall reactor).

It is worth noting that the second cold wall reactor (Cold wall reactor (b)) was designed specifically for these sensors. Owing to their embedded heater, the temperature was well controlled during the AACVD process.

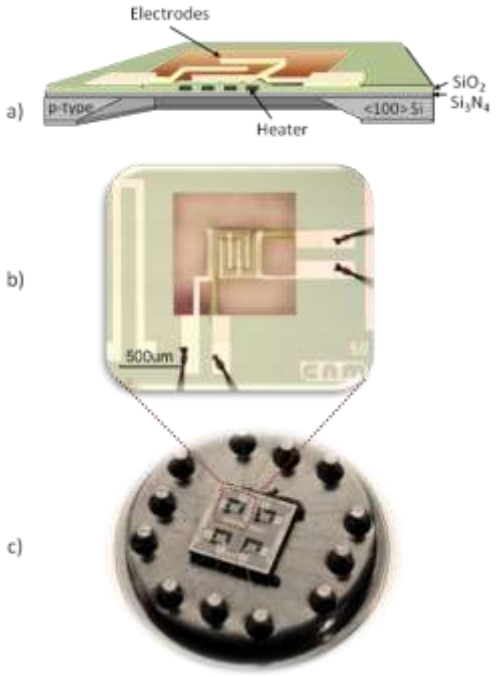

Figure III. 11. Schematic view (not to scale) of the microsensor platform section (a) and

photograph of an individual microsensor platform showing the sensing-active area (b). Array of microsensors mounted on a standard TO-8 package (c).

3.4 Gas sensors characterization study

3.4.1 Measuring set up

Gas sensing tests were carried out by monitoring the electrical resistance changes of the films towards various analytes at different operating temperatures. The measurement set up consisted of different elements as it is shown in Figure III. 12.

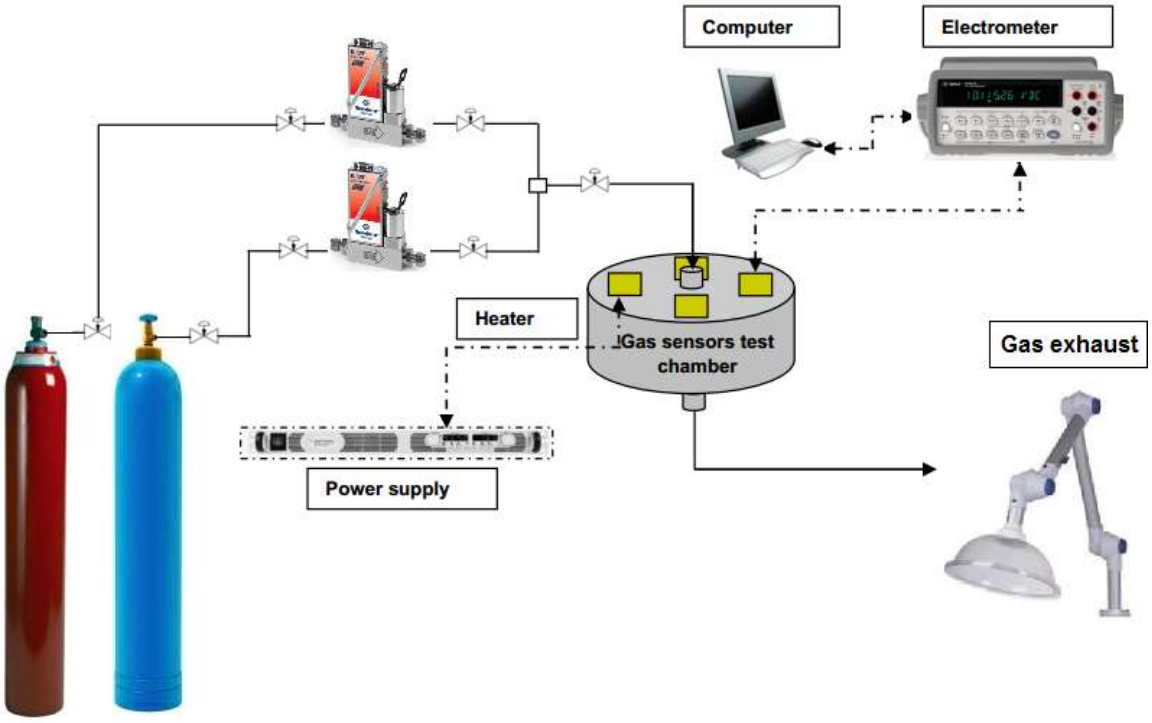

Figure III. 12. Measurement set up.

The gas delivery system included mass flow controllers, pressure regulators and required electronics in order to control gas flow inside the test chamber. It was dedicated to control and measure the necessary flow for the sensor characterization. The main carrier gas was chosen to be dry synthetic air. The measured concentration was obtained by diluting a specific target

gas concentration (contaminant gas) in the main carrier gas (dry air). The concentration was adjusted to desirable levels by a PC using the Bronkhorst High-Tech V 6.32.0.4 software.

Regarding humidity measurements, they were performed using an Environics, Series 4000, which allowed us to automatically mix up to three individual gases in a balance gas (air, pollutant gas and humidity).

The test chamber with a volume of 2×10^{-2} dm^3, was made from Teflon/stainless steel. It had an inlet, which was connected to the output of the mass-flow controller system and an outlet, which was connected to a fume hood. Additionally, it possessed four slots for placing sensors chips. All of them were connected to specific PCBs for monitoring of films and heater resistances, respectively.

The electrical resistance of the films was monitored by using either an Agilent-34970A multimeter or Keithley Instruments (Inc electrometer, model 6517A), while the sensor operating temperature was set by connecting the sensor heaters to an external power supply (Agilent, model N5700). In table III.4 a characterization of the heaters for all the sensor types used in this doctoral thesis is presented.

Table III.4. Heater characterization of all the studied sensors.

	Alumina sensors		MEMS-based 4 microsensors		Flexible sensors-1		Flexible sensors-2	
T °C	Volt, V	P, mW	Volt, V	P, mW	Volt, V	P, mW	Volt, V	P, mW
150	1.1	131	3.8	20	2.47	63	4.25	350
200	1.51	311	4.7	28	3.23	90	5	440
250	2	491	5.5	36	4	120	5.8	530
300	2.4	671	6.4	45	4.7	150	6.5	620
350	2.9	851	7.2	53	5.5	180	7.2	710

400	3.3	1030	8	61.64	---	---	---	---

Legend: Volt: Voltage; P: Power.

3.4.2 Target gases

In Table III.5, a summary of all the gases or vapours (and their concentrations) employed in this thesis is given. The sensors were exposed to each analyte for 10 minutes in a continuous flow of 200 sccm. Subsequently the chamber was purged with clean air until the initial baseline resistance was recovered. The sensor response (R) was defined for a reducing gas as R=Ra/Rg, and for an oxidising gas as R=Rg/Ra, where Ra represents the sensor resistance in air at stationary state and Rg is the sensor resistance after 10 minutes of gas exposure.

Table III. 5. Target gases and their concentrations.

Target gas	Concentration in ppm
Hydrogen (H_2) (reducing)	40, 80, 100, 200, 250 and 500
Ethanol (EtOH) (reducing)	40, 80, 100, 200 and 500
Nitrogen dioxide (NO_2) (oxidizing)	0.04
Carbon monoxide (reducing)	50, 60, 80, 100, 200 and 500
Hydrogen sulphide (reducing)	0.3, 0.5, 1, 3 and 5

Chapter 4: Au and Pt nanoparticles functionalized tungsten oxide nanoneedles synthesized via aerosol assisted-CVD, and used for gas sensing application

4.1 Introduction

This chapter reports the results obtained from the functionalization of tungsten oxide nanoneedles (NNs) with either gold or platinum nanoparticles (NPs), using a single step AACVD method. The findings are grouped and presented in two parts, as it is shown below. In each one, film analysis and gas sensing characterization are discussed.

- AACVD of WO_3 NNs functionalized with Au or Pt NPs grown via a hot wall reactor, onto Alumina and flexible gas-sensors platforms.
- AACVD of WO_3 NNs functionalized with Au or Pt NPs grown via a cold wall reactor, onto alumina and MEMS-based gas-sensor platforms.

4.2 AACVD of WO_3 NNs functionalized with Au or Pt NPs grown via a hot wall reactor, onto alumina and flexible gas-sensors platforms

In this section, the results (film analysis and gas sensing results) obtained from the growth of pristine WO_3 NNs and WO_3 NNs functionalized with Au or Pt NPs, by AACVD method onto alumina gas sensor substrates are presented (for the details of the experimental set up, please see chapter III, section 3.1). The main precursor was tungsten hexaphenoxide $W(Oph)_6$, which is reported in chapter III, section 3.1.2. This study was aimed at verifying the reproducibility of the AACVD technique, since the AACVD growth of Au or Pt decorated

WO_3 NNs had been performed before by our colleague Dr. Vallejos at University College London [11].

After that, the optimal conditions for the growth of WO_3 NNs by using a commercially available tungsten hexacarbonyl ($W(CO)_6$) precursor are discussed. The SEM and XRD results are shown and compared with those achieved employing the lab-made precursor ($W(Oph)_6$).

Finally, the last part of this section was dedicated to study the film analysis results and the gas sensing characterization of either Au or Pt NPs functionalized WO_3 NNs, grown via AACVD method onto flexible polymeric micro-hotplate sensor substrates.

4.2.1 Single step deposition of Au- and Pt-NPs- functionalized WO_3 NNs using AACVD method onto alumina gas sensor substrate

Pristine WO_3 NNs or WO_3 NNs functionalized with Au or Pt nanoparticles were obtained from AACVD using pure $W(OPh)_6$ or $W(OPh)_6$ mixed with $HAuCl_4$ $3H_2O$ and/or H_2 $PtCl_6 \cdot x$ H_2O precursors. The solution preparation and the experimental conditions are illustrated in Table III.3 (lines 1-3). The films that resulted from the process were uniform and adherent to the alumina substrates. Furthermore, they were characterized by a dark black colour when as-deposited, which after annealing became yellow for tungsten oxide (W), pale violet for gold-functionalized tungsten oxide (Au/W) films, and white for platinum (Pt/W) functionalized tungsten oxide films. Dark blue films are indicative of reduced tungsten trioxide stoichiometry (WO_{3-x}, x = 0-0.3) and yellow films are indicative of fully oxidised WO_3, as it was reported in [11].

4.2.1.1 Morphology and structure

To investigate the morphology of the synthesised nanostructures, scanning electron microscopy (SEM) was used. SEM imaging of these films (Figure IV.1) showed a high density of non-aligned NNs with uniform diameter ranging between 60 and 100 nm, while their length was about a few micrometres (≈ 8µm). This is consistent with Dr. Vallejos previous work on the deposition of W Au/W and Pt/W films on MEMS-based substrate grown in the AACVD reactor at University College London [11].

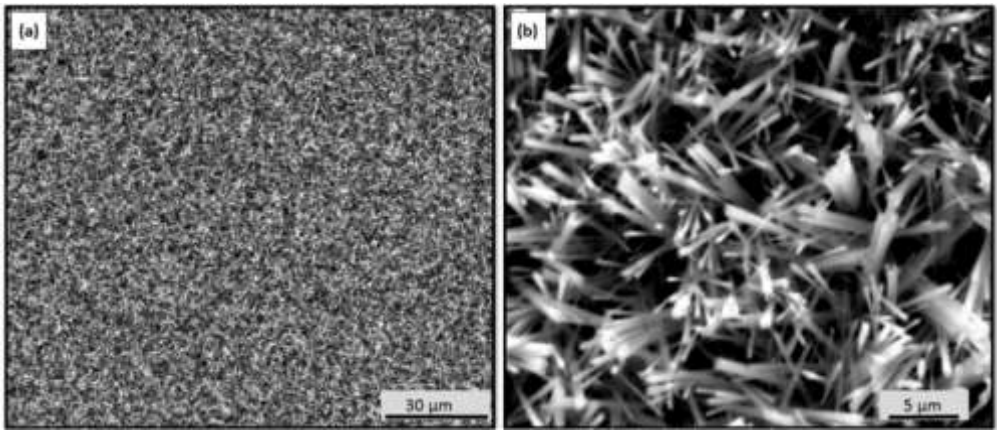

Figure IV.1. Film morphology observed by SEM images at low (a) and high (b) magnification. Non-functionalized (W) and functionalized NNs films with gold (Au/W), platinum (Pt/W) show the same morphology.

The crystalline structure of the films was studied by XRD analysis. The results revealed the presence of monoclinic-phase WO_3 in both non-functionalized and functionalized films (Figure IV.2), consistent with results reported in [11]. The patterns of the films were identified by using P21 /n space group, ICCD card no. 72–0677 and the lattice parameters were *a*= 7.306 Å, *b*= 7.540 Å, *c*= 7.692 Å, and β=90.88°. Overall, all the patterns indicate a preferred orientation in the [020] direction, showing intense diffraction peak at 23.46° 2θ, which corresponds to the monoclinic phase. Gold and/or platinum diffraction peaks were not observed in functionalized films. This can be explained by the small amount of the produced

Au and Pt NPs. Moreover, green-coloured peaks present in all the patterns are characteristic of corundum (Al_2O_3), which is typically found in the alumina substrates used. As we can see, these peaks resulting from the alumina substrate are very intense in comparison to those peaks related to WO_3.

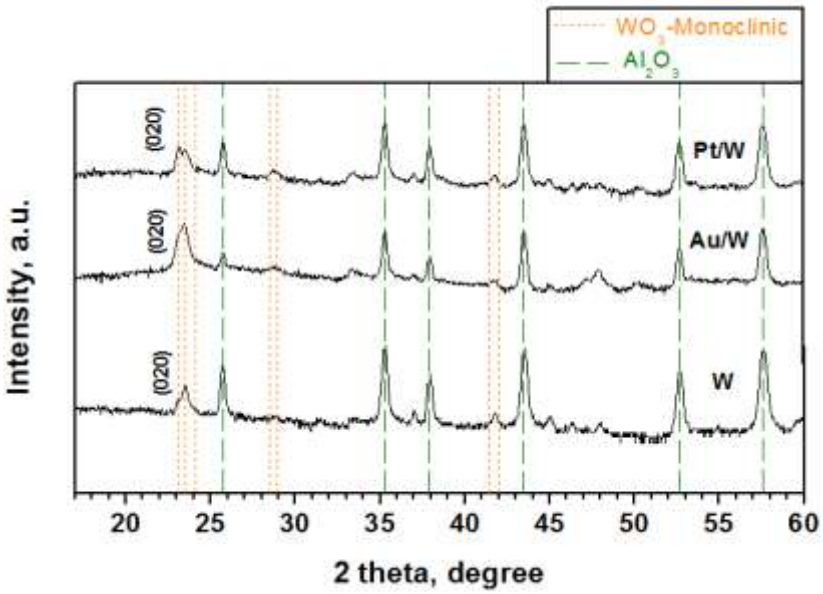

Figure IV.2. XRD patterns of the non-functionalized (W), and functionalized films with gold (Au/W) or platinum (Pt/W) NPs.

To verify the presence of nanoparticles, transmission electron microscopy (TEM) was employed, the samples were prepared by 10 min ultrasonication in methanol of the substrates in which NNs had been grown and subsequent drop of the removed NNs onto TEM grids. The TEM imaging of NNs showed the presence of well-dispersed metal nanoparticles (Au or Pt) along the surface of the NN. The particles displayed approximately spherical morphologies, with sizes between 4–10 nm and 1–4 nm for Au and Pt, respectively (total population of 20 particles were analysed), consistent with results seen previously for gold and platinum-NP functionalized tungsten oxide NNs on MEMS-substrates [11]. The difference observed in the size of Au and Pt NPs can be attributed to many effects including the surface oxidation of platinum NP which was detected in the XPS analysis [11], the inverse relationship between

the size of the metal NPs after high temperature treatment and the melting point of the metal (i.e., 1336 K for Au and 2042 K Pt) or to the presence of traces of residual chlorine when precursors containing chlorine are employed [11]. This is the case of $HAuCl_4$, in which residual Cl could cause an increase in the Au NP size [11].

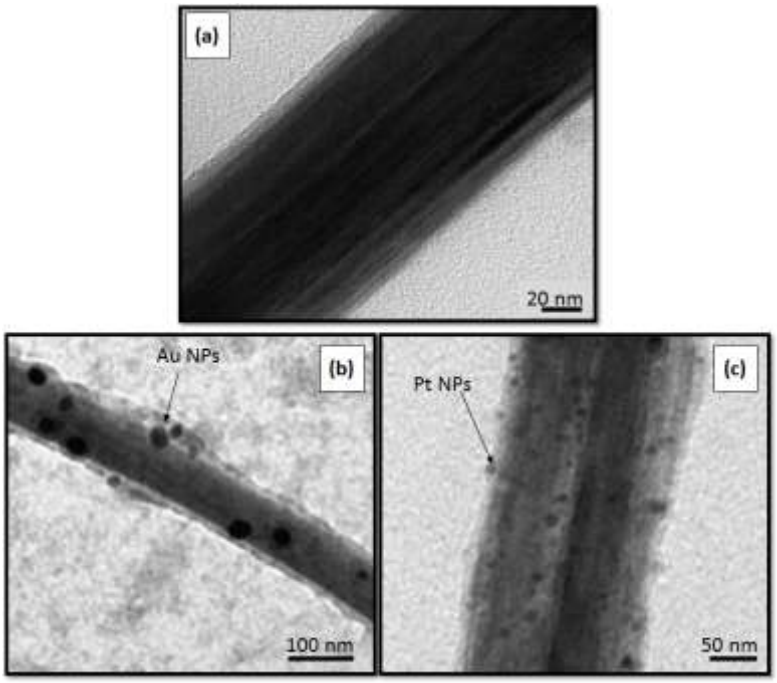

Figure IV. 3. TEM of the non-functionalized (a) and functionalized samples with gold (b), and platinum (c) after annealing.

4.2.1.2 Gas sensing characterization

In this thesis, annealed films were used in the sensor devices. This was done to stabilize the morphology of the films. To study the effect of the operating temperature on the sensor response, we have exposed our sensors (Au/W, Pt/W and W) towards 40 ppm of ethanol vapour at three different working temperatures 150 °C, 200 °C and 250 °C. A comparison of the response trend of the sensors is shown in Figure IV.4, which suggests that the temperature dependence of the response is not influenced by the film composition. Overall, at 150°C, the functionalized and non-functionalized sensors showed unsaturated responses with drift in

their baseline resistance. In contrast, at temperatures exceeding 150 °C, all the sensors showed stable responses with complete recovery of the baseline resistance within 400 s after analyte removal. From Figure IV.4 we can conclude that all the sensors show the highest response at 250 °C, which we have considered as the optimal working temperature for the subsequent studies.

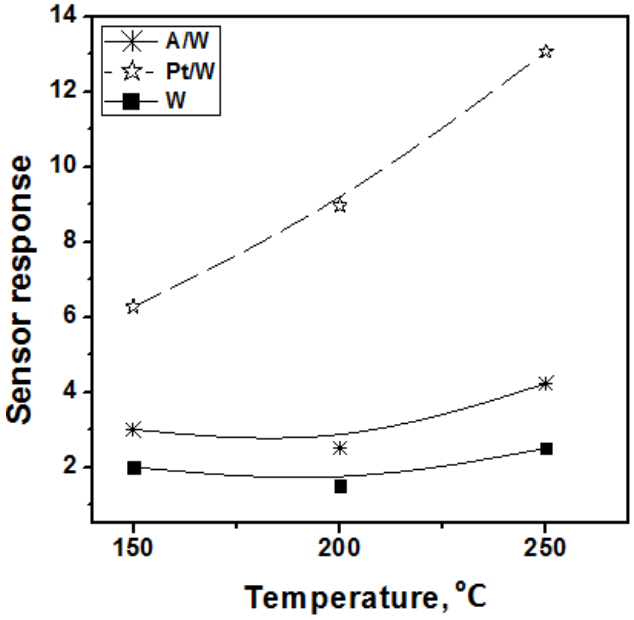

Figure IV.4. Sensor responses towards 40 ppm of EtOH, as function of the sensor operating temperature.

Figure IV.5 depicts the film resistance change of pristine WO_3 NNs and WO_3 NNs functionalized with Au or Pt NPs films, toward 40 ppm of EtOH at 250 °C. As we can see, the sensors exhibit an *n-type* semiconductor behaviour, i.e. increasing resistance upon exposure to air and decreasing resistance upon exposure to reducing gas. Furthermore, for five measurement replicates, the sensors responses remain stable with good reproducibility and fast detection of the gas. The response and/ recovery times for Au/W, Pt/W and W films were 73s / 164s, 257s / 337s and 35s / 79s respectively. From our results we observe that an enhancement in the kinetics of response does not necessarily contribute to an improvement of the sensor response.

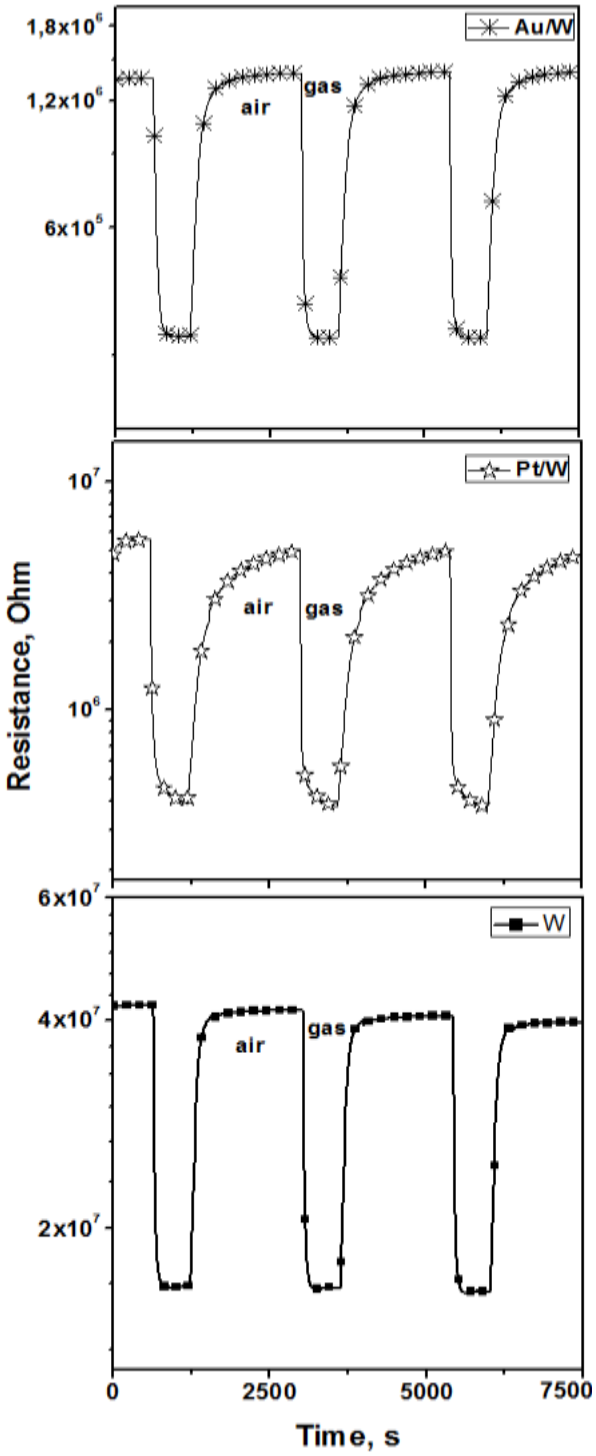

Figure IV.5. Film resistance change to 40 ppm of EtOH at 250 °C.

To study the dependence between the sensor response and the analyte concentrations, we have tested our sensors toward various concentrations of EtOH, ranging from 20 to 500 ppm.

From Figure IV.6, it is evident that an increase in the analyte concentration produces an increase in the sensors response, which is the normal behaviour of metal oxide gas sensors. Moreover, functionalized films exhibit high responses compared to pristine ones.

The mechanisms explaining the role of additives in gas sensing are based on three ideas. The first, related to an enrichment of the MOX surface with reactive species through catalysis 'spill-over', the second, to changes in the chemical state of the additives with the analytes 'Fermi-level control' and the third, recently noticed in palladium and platinum NPs supported on SnO_2, that suggest a 'local/surface site effect' highly dependent on the distribution of additives at the surface of the MOX [110-112], discrimination of the presence of these mechanisms and the degree of their contribution to the sensing response are not straightforward from current results. Comparing these results with the ones reported in [11], the sensing properties shown by Au/W, Pt/W and W alumina gas sensors are quite similar to the ones grown in MEMS-based sensors and the decrease observed in the sensitivity can be related to the gas sensor platform used. Consequently, AACVD technique has demonstrated its ability to reproduce films with very similar characteristic both in the morphology, the structure and in the gas sensing properties.

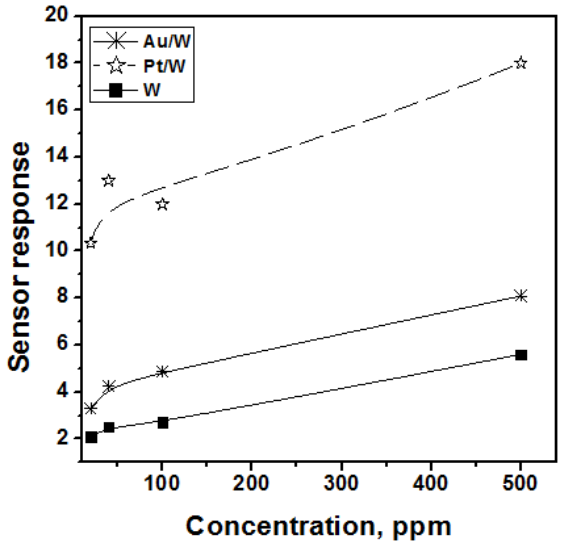

Figure IV.6. Sensors response as a function of the gas concentration (20, 40, 100 and 500 ppm).

4.2.2 Deposition via tungsten hexacarbonyl (W $(CO)_6$) precursor using a hot wall reactor

During this doctoral thesis, we have started our work using tungsten hexaphenoxide as the main precursor to produce tungsten oxide NNs. As it was mentioned in chapter III, section 3.1.2, this precursor is not commercially available and it was delivered from our collaborators at UCL. Thus, it was necessary to find a commercialized precursor, which could be used for synthesizing the nanomaterial with similar properties. Tungsten hexacarbonyl ($W(CO)_6$) was identified as a good candidate precursor and purchased from Sigma-Aldrich. Table IV.1 illustrates the experimental conditions using this precursor for the growth of WO_3 NNs.

Table IV.1. Experimental conditions used for the growth of WO_3 NNs from $W(CO)_6$.

Substrate	Precursor (mg)	Solvent (mL)	Temperature (°C)	Flow (L/min)	Morphology obtained
Glass	50	20 methanol	500	0.5	NNs
	50	20 Acetone	500	0.5	NNs
	50	15 Acetone+ 5 Methanol	500	0.5	NNs
Alumina	50	20 methanol	500	0.5	NPs
	50	20 Acetone	500	0.5	NNs
	50	15 Acetone+ 5 Methanol	500	0.5	NNs
Silicon oxide	50	15 Acetone+ 5 Methanol	500	0.5	NNs

As we know from the previous studies, the increase in the deposition temperature encourages the growth of the NN structure. For this reason, we have set the growth temperature at 500 °C. Moreover, we started with toluene and we found that this solvent was

not capable to completely dissolve the $W(CO)_6$ precursor. Next, we tried with methanol, acetone and a mixture of methanol and acetone using a glass substrate (Table IV. 1). The precursor was soluble in all these solutions and the obtained films were composed of a thick layer of long and non-aligned NNs. However, when we used alumina substrates, the results were not the same for methanol. For this solvent the films were composed of an agglomeration of spherical WO_3 particles (see Figure IV.7. a & b). Besides this, the nanoneedles grown from acetone were short and not well defined (Figure IV.7. c). In contrast, when we used a mixture of acetone and methanol, the films were composed of long and well defined NNs (Figure IV.7.d). Furthermore, we used this mixture of solvents for the growth of NNs on silicon oxide substrates and the results were satisfactory (see Figure IV.7. e). Thus, for subsequent studies, we adopted the deposition of tungsten oxide NNs from $W(CO)_6$ by using a mixture of acetone and methanol (see Table IV.1, line 3 and 6).

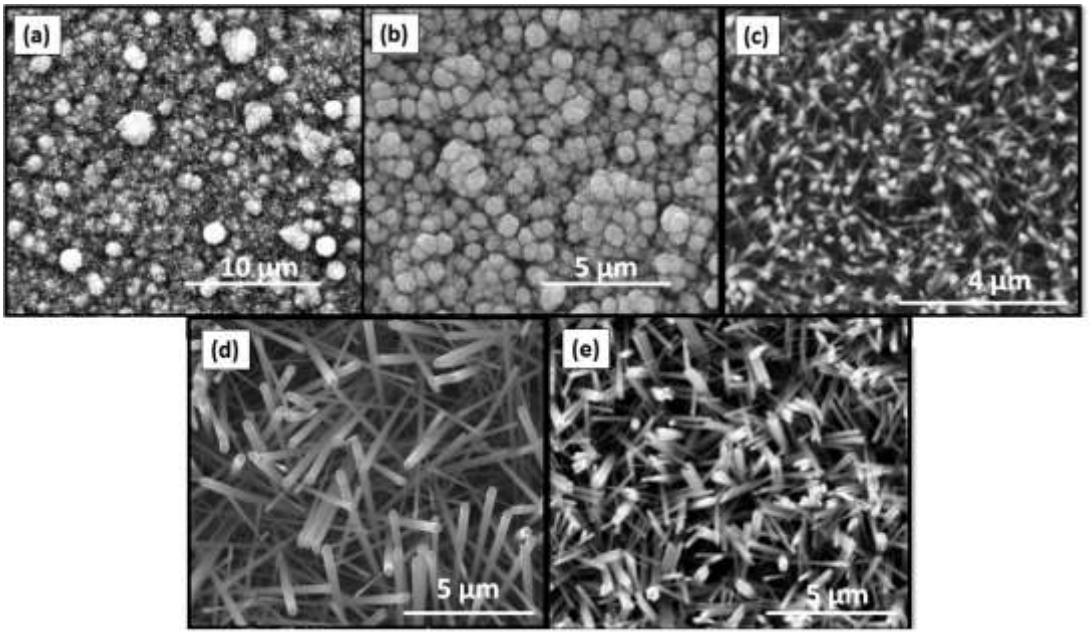

Figure IV.7. SEM images of the WO_3 NNs grown in alumina substrate: (a) and (b) using methanol, (c) using acetone (d) using a mixture of methanol and acetone and on silicon oxide substrate (e) using a mixture of methanol and acetone.

To check the crystalline structure of the obtained WO_3 NNs, XRD analysis was investigated. Figure IV.8 displayed an example of the XRD pattern recorded from WO_3 NNs grown onto a MEMs based gas sensor substrate. The results revealed the formation of monoclinic WO_3 phase (P21/n (14) space group, with typical cell parameters of a= 0.729 nm, b=0.7539 nm, c=0.7688 nm, and β=90.91º; ICCD card no. 72-0677), with preferred orientation in the (002) direction, showing an intense diffraction peak at 23.10° 2θ. Additionally, a strong platinum reflection at 39.9° 2θ was observed, which was coming from the electrodes.

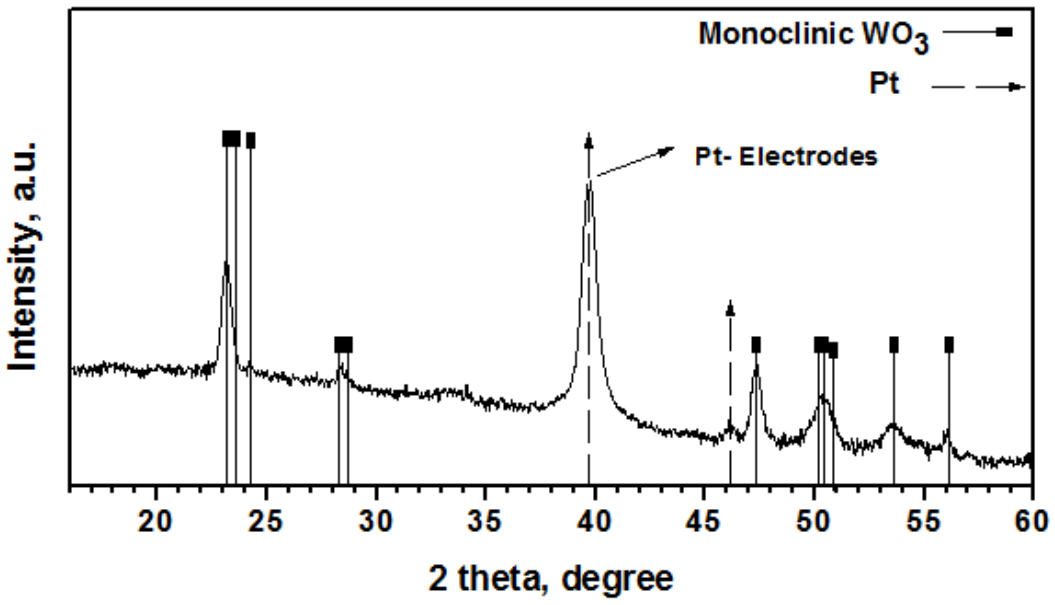

Figure IV.8. XRD pattern of tungsten oxide NNs grown from $W(CO)_6$ precursor.

Hence, WO_3 NNs were successfully grown from the AACVD of $W(CO)_6$ precursor. Morphology and the structure results are in good agreement with those obtained in previous work, where $W(OPh)_6$ had been used as precursor [11,73,74].

4.2.3 Single step deposition of Au- and Pt-NPs- functionalized WO_3 NNs using AACVD method, onto flexible gas sensor substrates

Owing to their low cost, lightness, flexibility, easiness of processing and conformability, electrically and chemically inert polymeric or plastic sheets represent an interesting opportunity for the fabrication of a new generation of gas sensors to be integrated in widespread, portable devices and smart objects. Aerosol assisted CVD, as shown by our prior results [73], is a flexible, inexpensive and high-yield technique for growing metal oxides with remarkable gas sensing properties. Here we show the success of this technique in the growth of low-dimensional metal oxide nanostructures directly onto flexible polymeric substrates, e.g. suitable for integration in low cost tags. Furthermore, we show that the resulting devices exhibit a highly enhanced sensitivity towards hydrogen and ethanol, which represents a clear improvement in comparison to our previous works.

4.2.3.1 Morphology and structures

As it was mentioned in chapter III, section 3.3.2, we have worked with two flexible polymeric transducers. Herein we will focus in the results obtained from the one described in 3.3.2.a.

AACVD using $W(CO)_6$ or $W(CO)_6$ co-reacted with $HAuCl_4 \cdot 3H_2O$ and/or H_2 $PtCl_6 \cdot x$ H_2O precursors resulted in the formation of adherent uniform films of tungsten oxide NPs, or tungsten oxide NNs functionalized with Au or Pt NPs. The films were grown at a temperature of 380°C to avoid damaging the polymeric sensor transducers. The detailed experimental parameters employed for the AACVD deposition are cited in Table III.3 (lines 4-6).

Overall, the as-deposited films were characterized by a dark blue colour, while after annealing, the colour changed and became white for pristine and Pt functionalized WO_3 films, and blue-violet for Au functionalized WO_3 films. This is consistent with our previous results

on rigid substrates [73]. Figure IV.9 displays the SEM images of pristine WO_3 NPs and WO_3 NNs functionalized with Au or Pt NPs. As we can see, there is a clear difference between non-functionalized and functionalized films. Pristine WO_3 layers were composed of spherical nanoparticles homogenously distributed over the substrate, whereas, functionalized samples were composed of a thicker layer of well-defined and non-aligned nanoneedles. In fact, this difference is attributed to the growth temperature, which plays an important role in controlling the resulting morphology via the type of chemical reactions that take place during the deposition process. To obtain pure WO_3 NNs structures, we need higher growth temperatures compared to the temperatures needed for growing metal-decorated WO_3 NNs. The metal precursors undergo a homogenous nucleation in the gas phase to form NPs, whereas the main WO_3 precursor must undergo some degree of heterogeneous reaction on the substrate surface [113]. Besides to this, it has been reported that the presence of metal precursor plays an active role for the growth of WO_3 NNs at lower temperatures [113]. Recently, Vallejos and co-workers reported that the use of methanol solvent helps to obtain NNs from $W(CO)_6$ at lower temperatures [114]. However, in our case as it was mentioned above, the growth of NNs from methanol was difficult, which can be related to other parameters that influence the growth of NNs, such as the geometry of the reactor used, the concentration of the reactants and the carrier gas flow.

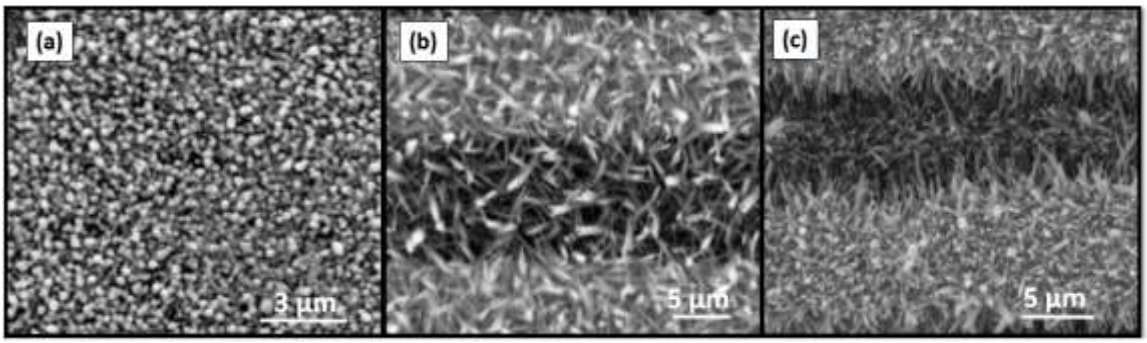

Figure IV.9. SEM images of (a) pristine WO_3 NPs, (b) Au/WO_3 NNs and (c) Pt/WO_3 NNs grown directly onto flexible polymeric microhotplates.

Figure IV.10 shows the XRD patterns recorded from either Au or Pt NPs functionalized WO_3 NNs. The results revealed the formation of monoclinic WO_3 in both samples (P21 /n space group, ICCD card no. 00-043-1035 and lattice parameters of a= 7.297 Å, b= 7.539 Å, c= 7.688 Å, and β= 90.91°). Moreover, the patterns exhibit preferred orientation in the (010) direction showing intense peaks at 23.6°and 48.1° 2θ, which correspond to (020) and (040) reflexions of the monoclinic phase, consistent with the results reported in [114].

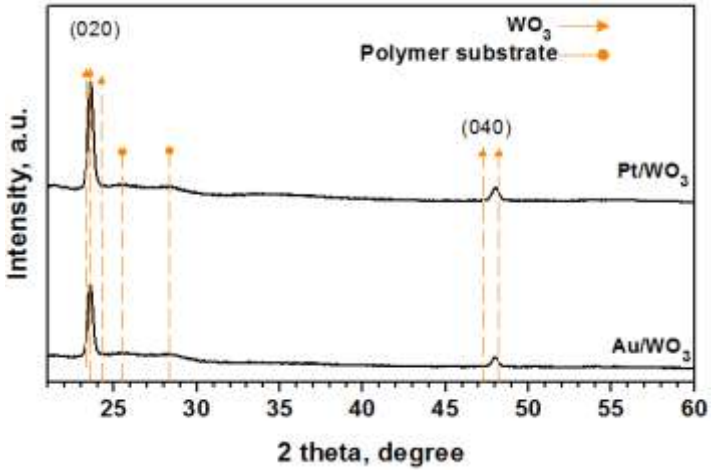

Figure IV.10. XRD patterns of either Au or Pt NPs functionalized WO_3 NNs.

4.2.3.2 Gas sensing characterization

Gas sensing tests were carried out to check EtOH and hydrogen responses at temperatures ranging between 200 °C and 320 °C. Figure IV.11 shows the temperature dependence of the response for each sensor (i.e. based on Au/W and Pt/W films). The temperature dependence of the response both for EtOH and H_2 is influenced by the film composition. The response to EtOH exhibits the maximum at 320°C for Au/WO_3 sensors, while the maximum response was achieved by Pt/WO_3 films in a broad temperature range (i.e., from 240 to 320°C). Additionally, the response to H_2 displayed the maximum at 320°C for Au/WO_3 sensors and at 200 °C for Pt/WO_3 sensors. Moreover, from the gas sensing

results (Figure IV.11) it is clear that for both analytes, Pt/WO_3 sensors showed higher responses than Au/WO_3 sensors.

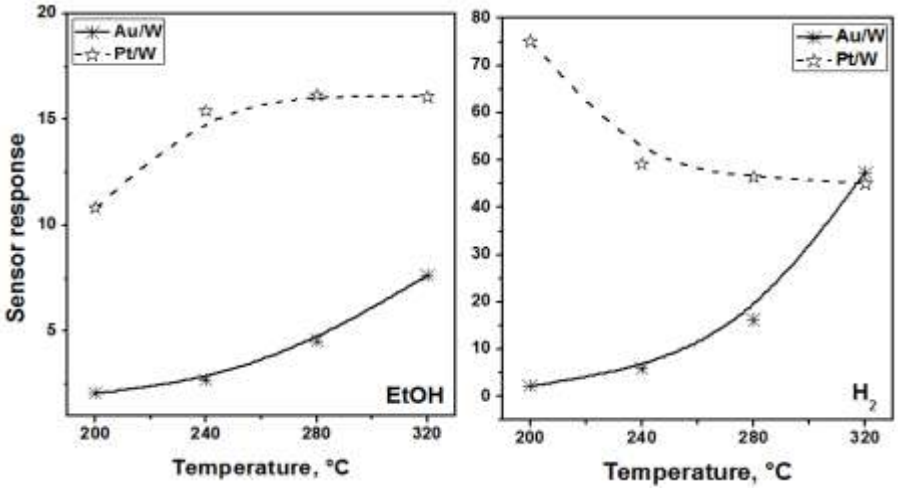

Figure IV.11. Au/W and Pt/W sensor responses towards 80 ppm of EtOH and 500 ppm of H_2, as function of the operating temperature.

Figure IV.12 displays an example of Au/W and Pt/W film resistance changes toward 500 ppm of H_2 at their optimal working temperatures. The sensor responses displayed a typical n-type semiconductor behaviour, i.e. increasing electrical resistance when exposed to air and decreasing electrical resistance when exposed to a reducing gas such as H_2. Generally, the sensors showed stable and reproducible responses, with a tendency to reach a stationary state, or a saturated sensor response, after 100 s of exposure to an analyte, with complete recovery of the baseline resistance within 700 s after analyte removal. The response and/ recovery times for Au/W and Pt/W films were 54 s / 37 s and 42 s / 290 s respectively.

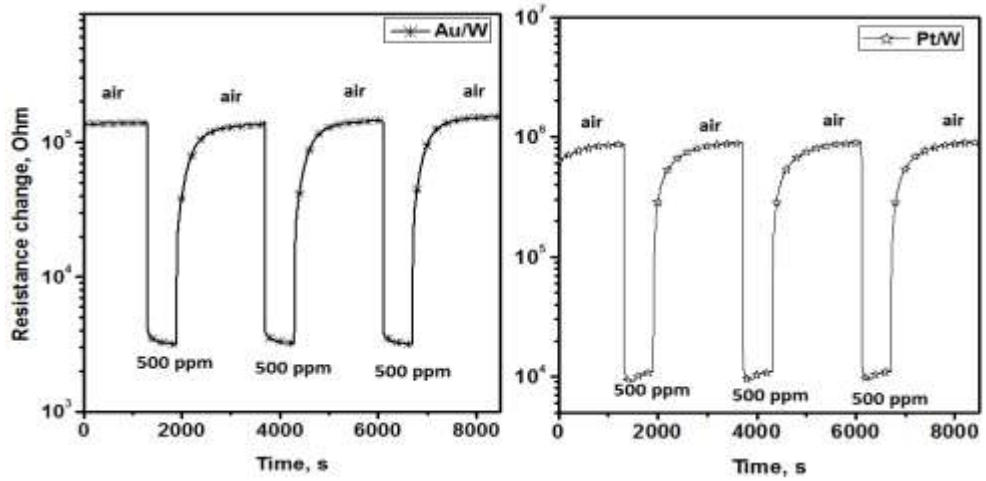

Figure IV.12. Au/W and Pt/W film resistance changes toward 500 ppm of H_2 at their optimal working temperature.

Table IV.2 summarises the responses obtained from the studied polymeric microhotplate sensors and the ones reported by Vallejos and co-worker, toward 500 ppm of H_2 [11]. By comparing these results, it is clear that polymeric microhotplate sensors showed higher responses than MEMs-based sensors. The responses toward H_2 have been increased by 7 and 2 times for Au/WO_3 and Pt/WO_3 polymeric microhotplate sensors, respectively. Moreover, the highest response toward 500 ppm of H_2 was achieved at the lowest operating temperature tested (200°C).

Table IV.2. A comparative study between the responses of flexible polymeric microhotplate sensors and MEMs-based sensors toward 500 ppm of H_2.

Sensor transducer	Au/W response	Pt/W response
Flexible polymeric sensors	47.4 at 320 °C	75.4 at 200 °C
MEMs-based sensors	6 at 250 °C	35 at 250°C

After the good results shown by these sensors and once the ability of AACVD method to grow metal oxide nanostructures onto flexible polymeric substrate had been demonstrated, a new flexible sensor design (see chapter III, section 3.3.2.b) was explored. The novelty of this design is the simultaneous double functionality of the heater electrode, since it works as a

heater and drains the sensing current at the same time. Whereas, the other electrode is used to read the current variations related to the changes in the chemical environment close to the sensing surface. The main objective was to test the functionality of this new gas sensor architecture. For this reason, we have chosen Pt NPs functionalized WO_3 NNs as a sensing film, and H_2 as target gas. The sensing film was directly deposited onto the sensor substrate via AACVD method. The morphology and the structure of the obtained films are similar to the ones described above. The working temperature was fixed at 200 °C and the sensor was exposed to consecutive pulses of H_2 gas. Figure IV.13 displays the current change of a Pt/WO_3 film toward different concentrations of H_2. The results revealed that the sensor exhibits an n-type semiconductor behaviour, i.e. increasing the current when exposed to H_2 (i.e. a reducing gas) and decreasing the current when exposed to air. Moreover, the responses were very stable with complete recovery of the baseline current when the sensor is exposed to clean air. Furthermore, the sensor has demonstrated it capability to discern between the different concentrations of H_2.

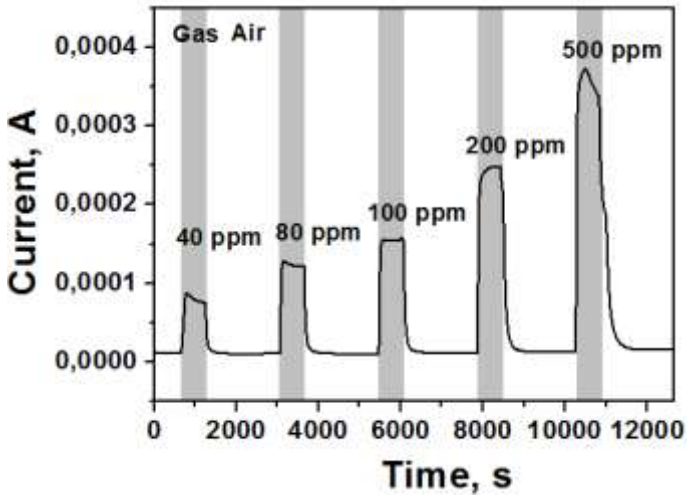

Figure IV. 13. Current change of Pt/WO_3 based flexible sensor exposed to different concentrations of H_2 gas at temperature of 200 °C.

Figure IV.14.a shows the sensor response (I_0/I) as a function of H_2 concentration. As we can see, by increasing the gas concentration, the response is increased. The sensor responses toward 40, 80, 100, 200 and 500 °C were 7.5, 11.6, 14.62, 23 and 31 respectively. Furthermore, comparing these results with the ones described in Table IV.2, these responses are in the same order of magnitude as the ones observed from MEMs-based gas sensors [11]. Besides to this, the sensor response and recovery times (Figure IV. 14. b) are quite similar to the ones shown by flexible polymeric microhotplate sensors.

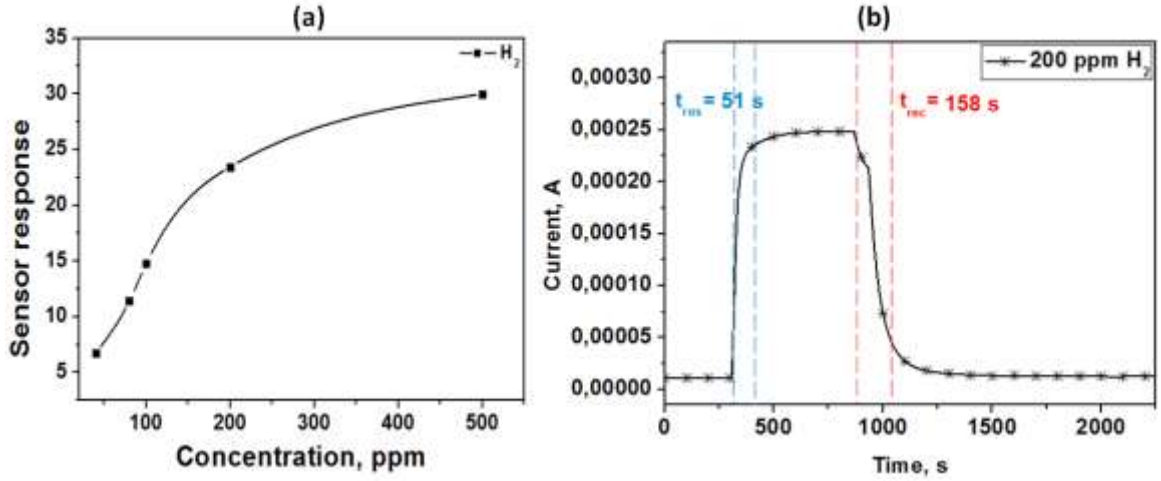

Figure IV.14. (a) Sensor response (I/I_0) as a function of H_2 concentrations at operating temperature of 200 °C, (b) the response and recovery time recorded from the sensor when exposed to 200 ppm of H_2.

4.3 AACVD of WO_3 NNs functionalized with Au or Pt NPs grown via a cold wall reactor, onto alumina and MEMS-based gas-sensor platforms

Recently, localized heating for CVD synthesis has emerged as a viable technique to confine the required thermal environment for both the decomposition of the vapour-phase reactants and the growth kinetics of nanostructures (NSs) to a microscale area [115], with the promise to reduce significantly the power consumption of high temperature reactors (i.e. 'hot-

wall' reactors) and the processing time, as sensors heaters offer faster temperature response with low power consumption. The use of localized heating for CVD is expected to increase deposition efficiency and reduce contamination avoiding deposition of precursors on the reaction chamber walls. AACVD, as an evolution of conventional CVD, has the peculiarity of forming functional NSs at relatively low temperatures, at atmospheric pressure, high deposition rates and without requiring the use of volatile precursors [116,117], which highlights the advantages of this method for the vapour-phase synthesis of MOX-NSs via localized heating [118].

Here, localized AACVD is developed using the self-heating capability of the sensor to produce a thick layer of non-functionalized and functionalized tungsten oxide layers. Two cold wall reactors were set, each one developed for a specific sensor transducer (i.e. alumina or MEMs transducers). Moreover, SEM, XRD, TEM and Raman analysis were employed to investigate the morphology and the structure of the produced layers. After that, H_2, EtOH and CO were used as target gases to test the gas sensing properties of the fabricated sensors; the results are discussed below.

4.3.1 Using alumina gas sensor substrates

At the beginning of this study, we fabricated a cold wall reactor, which was adapted for alumina gas sensors. The reactor and the sensor used are described in chapter III, section 3.1.1.2.a and 3.3.3 respectively. By applying a constant voltage to the sensor heater, the substrate temperature was set to 550ºC while the reactor temperature was maintained at ambient temperature. Moreover, to avoid any electrical contact between the heating element and the grown material, a dielectric layer was coated to the sensor heater. More details about the experimental conditions are described in Table III.3, line 17.

Morphology and structure

The AACVD reaction of tungsten $W(OPh)_6$ in a mixture of toluene and acetone using a cold wall reactor, results in the formation of non-uniform layers of either WO_3 NNs or WO_3 NPs. The layers were characterized by two different colours: dark-blue or dark black colour. It was reported that dark blue or black colours are indicative of partially reduced WO_{3-x}, with blue films characterized by formation of quasi-one dimensional nanostructures such as NNs. Figure IV.15 displays SEM micrographs of the obtained morphologies. It is worth noting that the experimental conditions were similar in all these AACVD depositions.

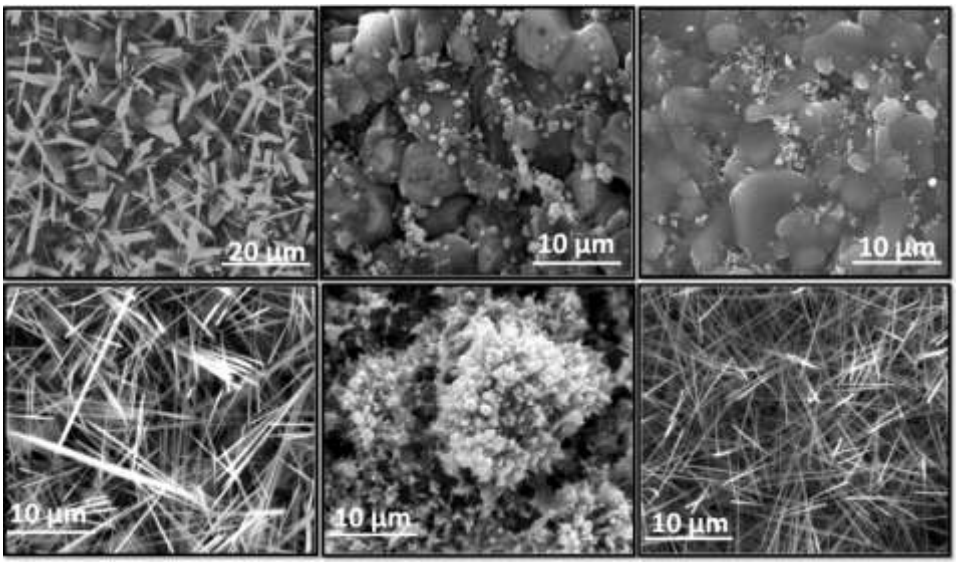

Figure IV.15. SEM images of the obtained morphologies using AACVD cold wall reactor and alumina gas sensor.

The obtained nanostructures varied between agglomerations of small NPs and thick layers of well-defined NNs. This difference in morphology is attributed to growth temperature variations, since temperature was not well controlled by the sensor heater. In fact, during the experimental deposition, we have noticed that at the initial stages of the AACVD process, the current through the sensor heater starts to increase exponentially and then influences the growth, by decreasing the substrate temperature. Consequently, in the next section, we have considered using different gas sensor platforms with the specificity of having the heating

elements embedded within electrically insulating layers to avoid any contact between heater and the surrounding atmosphere. This is the case of MEMs substrates.

4.3.2 Using MEMS-based gas sensor substrates

Herein, MEMs based gas sensors were used for the synthesis of pristine WO_3 and WO_3 functionalized with Au or Pt NPs using an AACVD cold wall reactor. For more details about the reactor or the sensors used, see chapter III, sections 3.1.1.2.b and 3.3.4.

4.3.2.1 Thermal and electrical characteristics of the microheaters

To evaluate the temperature distribution at the microsensor, electro-thermal simulations were performed biasing the heater at various voltages. Overall, results obtained from the simulations using different voltages showed a symmetric temperature profile along the membrane and a uniform thermal distribution at the sensing-active area of the microsensor, which is attributed to the double loop design of the microheater (Figure IV. 16).

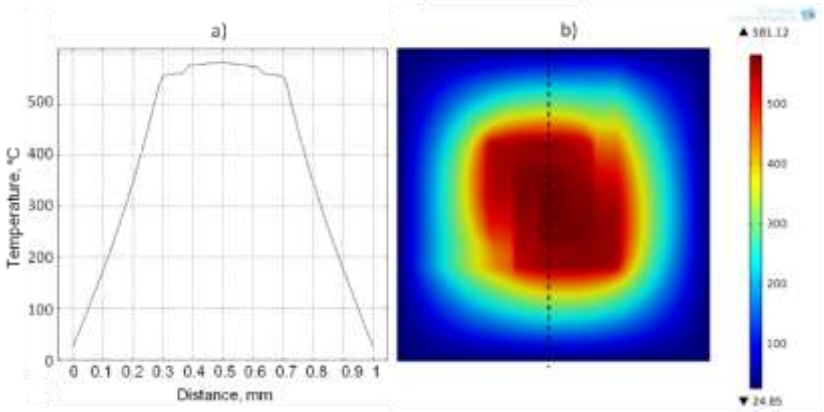

Figure IV.16. Simulated thermal profile (a) and temperature distribution (b) at the sensing active area.

Prior to AACVD and annealing of the sensing films (i.e. non-functionalized and either Au- or Pt- functionalized tungsten oxide NSs), the membranes were subjected to an aging

process at 580 °C using the self-heating capability of the microheaters in order to thermodynamically relax and stabilize the multiple layers comprising the membrane. During this process, the electrical resistance of the microheaters experienced a drift up to 12%, respect to the initial electrical resistance, reaching stabilization after 45 min. Subsequent intermittent tests of the microheater after AACVD, annealing process, and gas testing showed no drift of the microheaters' electrical resistance.

4.3.2.2 Morphology and structures

Localized AACVD of $W(CO)_6$ and $W(CO)_6$ with either $HAuCl_4 \cdot 3H_2O$ or $H_2PtCl_6 \cdot xH_2O$ at various temperatures (between 300 ºC and 580 ºC) resulted in the formation of adherent uniform films confined on the membrane. These films were characterized by a dark colour as-deposited, becoming white after localized annealing at 580 °C, which suggest a diminution of carbon residues from decomposition of the solvent used to form aerosol.

Low magnification SEM imaging of the films (non-functionalized and functionalized), for each deposition temperature studied, indicated the material grows over the membrane forming rings with different degrees of agglomeration (Figure IV.17.a). Thus, four regions are clearly distinguished, showing consistency with the temperature rings observed in the simulations (Figure IV.16.b). At higher magnification, these regions showed particle-like morphologies, for films grown at temperatures below 540 ºC (i.e. the effective temperature in the sensing-active area of the microsensors), with a concentration of smaller particles along the sensing-active area, as opposed to the outer regions. In contrast, the films (non-functionalized and functionalized) grown at 580 ºC showed a mixture of non-aligned uniformly distributed hollow-nanotube (NTs) and nanoneedle (NNs) structures (Figure IV.17. b & c) along the sensing-active area, with a modification of these structures on the subsequent temperature rings until they result in round-shaped particle films on the outermost ring.

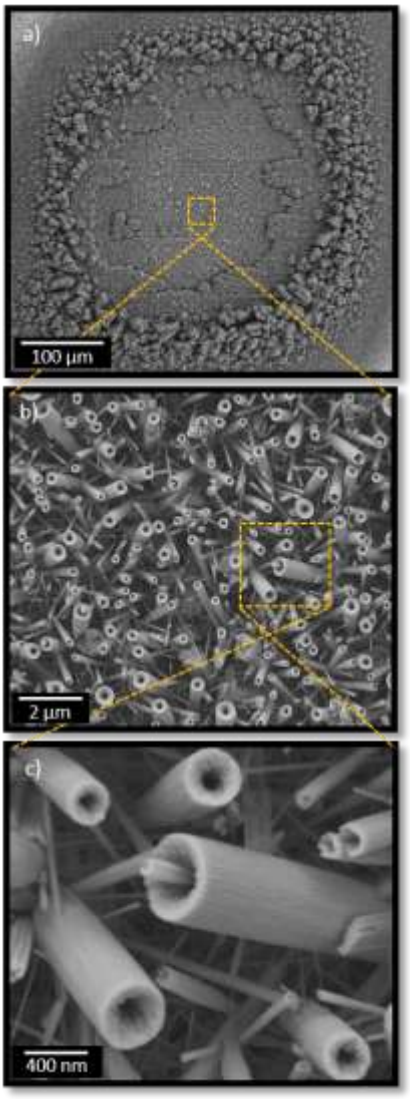

Figure IV.17. Film morphology observed by SEM images at low (a) and high (b and c) magnification.

These morphological transformations result from the temperature gradients at the membrane, and are similar to those observed when growing tungsten oxide via AACVD in a 'hot wall' reactor [11], although, it was noticed that the onset temperatures for the formation of nanostructured films are apparently higher compared to those determined before for AACVD in a 'hot-wall' reactor [119]. The different onset temperatures for the formation of NSs using AACVD via localized heating or 'hot-wall' reactors may be related to a change in the relation between the heated volume and the residence time of the droplets within this

volume, with the volume heated locally, becoming several times smaller compared to that of the 'hot-wall' reactor. SEM imaging of the films grown at 580 °C and annealed locally at the same temperature (i.e. 580 °C) showed unchanged morphologies in both non-functionalized and functionalized films. Monitoring of the electrical resistance of the films during annealing showed an increase of resistance, which reached a stationary stage after 120 min. The increase of the film resistance during annealing suggests a reduction of the concentration of oxygen vacancies in the structure.

TEM analysis (Figure IV.18) of the films removed from the membrane by sonication and dropped onto TEM grids displayed structures with different diameters, between 20 to 350 nm, which is in agreement with the mixture of the structures (NTs and NNs) observed by SEM.

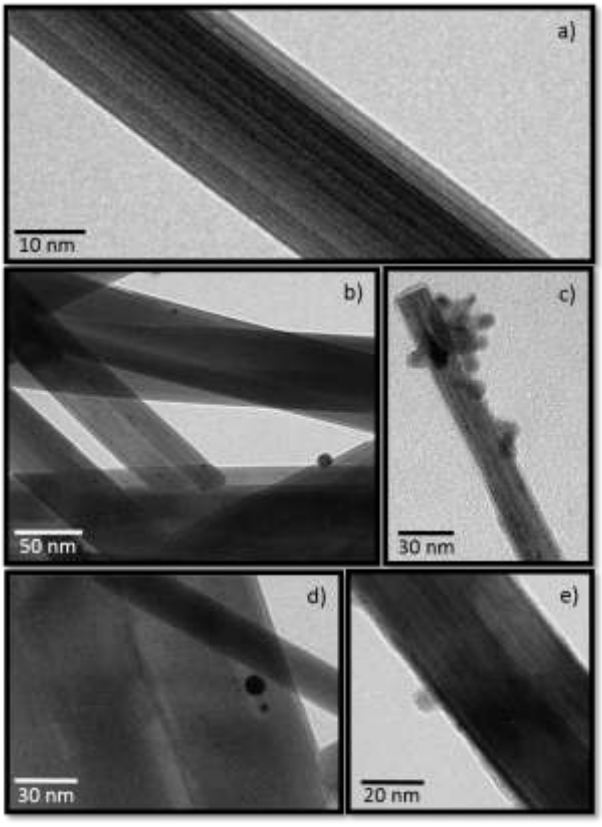

Figure IV.18. TEM of the non-functionalized (a) and functionalized NSs with gold (b and d) and platinum NPs (c and e).

The presence of relatively thick structures, including those coming from the membrane and the NTs, obstructed the visualization of the NPs distribution and the observation of the metal NPs incorporated in the structure. Overall, the particles, observed in the thinner structures, displayed approximately spherical morphologies, with sizes between 5–20 nm, 5–12 nm for the structures functionalized with Au and Pt, respectively, which is consistent with similar functionalized structures grown in a 'hot-wall' reactor [11]. According to the thermal decomposition profiles of the metal precursors ($HAuCl_4$ [120] and H_2PtCl_6 [121]) used for the functionalization of tungsten oxide, metallic gold and platinum should be obtained at the temperature required for the formation of tungsten oxide NSs via localized heating. Several depositions (15 for each material, i.e. non-functionalized and functionalized) were run at 580 °C, with good reproducibility of the morphology observed in the sensing-active area of the sensor. Consequently, these sensors (i.e. with nanostructures deposited at 580 °C) were used for the gas sensing characterization.

XRD analysis of the membranes, with the non-functionalized and functionalized tungsten oxide NSs grown onto them, are shown in Figure IV.19.a. As the main diffractions in these patterns are close to those reported for monoclinic (ICCD card no. 72-0677) and orthorhombic (ICCD card no. 71-0131) tungsten oxide, a clear discrimination between these phases is not straightforward from these results. However, based on previous XRD studies, in which similar tungsten oxide structures grown in 'hot-wall' reactor AACVD showed regularly monoclinic phases at similar deposition temperatures, it is likely the tungsten oxide structures grown via localized AACVD show the presence of a monoclinic-phase with two different stoichiometry: WO_3 (P21/n space group, a= 7.306 Å, b=7.540 Å, c=7.692 Å, and β=90.88º; ICCD card no. 72-0677) and WO_2 (P21/n space group, a= 5.575 Å, b=4.899 Å, c=5.561 Å, and β=118.86º; ICCD card no. 32-1393). The platinum and boron nitride (BN) diffraction peaks observed in the patterns come from the electrodes and the membrane, respectively.

Gold diffraction peaks were not observed in the films functionalized with gold, likely due to the low gold loadings incorporated. As standard XRD gives information about structural properties averaged over relatively large areas (~3 mm in *x* direction), the XRD patterns in Figure IV.19.a show not only the diffractions of the sensing-active area (400 µm × 400 µm) of the MEMS-based microsensor, but also those from the material deposited in the outer rings of this area, where the morphological features of the film are degraded, hence, the presence of diffraction patterns with different stoichiometry.

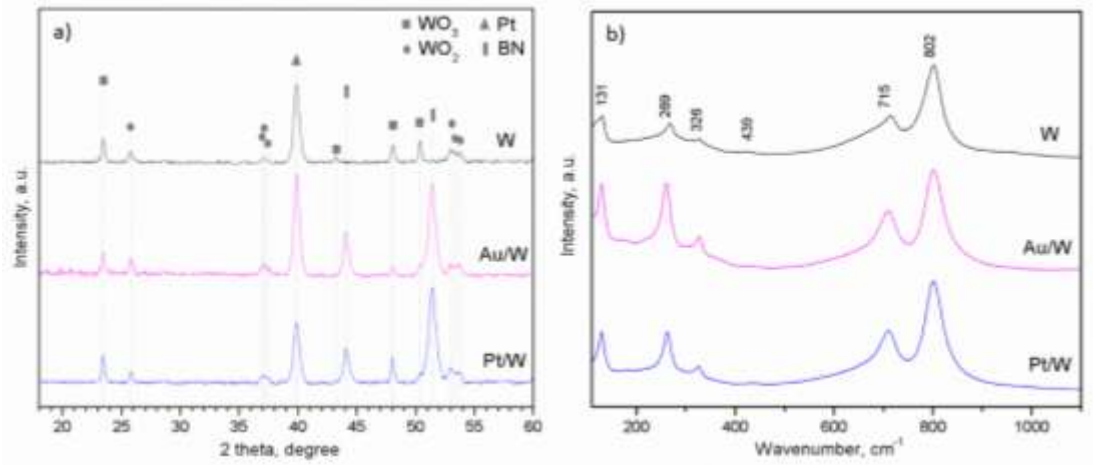

Figure IV.19. XRD patterns (a) and Raman spectra (b) recorded on the microsensors based on non-functionalized (W) and functionalized tungsten oxide NSs with gold (Au/W) and platinum (Pt/W) NPs.

In this context, Raman analysis (Figure IV.19.b) was used to determine the properties of the materials grown on the sensing-active area of the sensors. These results indicated well-defined Raman bands at 270, 326, 715 and 803 cm^{-1}. These bands fall close to the wave numbers of the four strongest modes of monoclinic tungsten oxide [122-124]. The bands at 270 and 326 cm^{-1} are assigned to bending modes of the bridging oxygen, whereas the bands at 715 and 803 cm^{-1} are assigned to the stretching modes. The weak bands at around 439 cm^{-1} and the lattice modes below 200 cm^{-1} are typical bands of the crystalline tungsten oxide. These results demonstrate that the films grown onto the sensing-active area are characterized by a monoclinic-phase WO_3 and without structural transformations due to the incorporation of

gold and platinum NPs. Interestingly, Raman analysis in different points of the sensing-active area showed consistently higher intensity peaks for the functionalized film (~10 %) compared to non-functionalized films, which could indicate that the incorporation of metal NPs induces defects and oxygen vacancies in the tungsten oxide structure.

4.3.2.3 Electrical properties

The work functions of gold (4.5 – 4.8 eV) [125], platinum (5.2 – 5.4 eV) [125], and tungsten oxide (4.3 – 4.9 eV) [126], indicate nano-Schottky barriers are formed at the interface of tungsten oxide and gold or platinum NPs. Considering the direct relation of the depletion depth and surface potential barrier [127], it is likely that the functionalized sensors experience different depletion depths for the same reactive species at the surface, affecting the electrical properties of tungsten oxide. Estimation of the activation energy for the electrical conduction based on conductivity measurements between 190 and 300 ºC in air revealed different apparent energies for non-functionalized (0.22 eV), Au-functionalized (0.25 eV) and Pt-functionalized sensors (0.15 eV). The apparent energy for non-functionalized sensors is in good agreement with earlier results reported for tungsten oxide [11]. Moreover, the change in the apparent energy of functionalized sensors is consistent with results reported in [11]. These results suggest gold and platinum NPs are effectively co-deposited with tungsten oxide by heating locally the microsensor, also, indicate the presence of strong electronic interaction between the NPs and the nanostructured support, particularly for Pt-functionalized structures [128].

4.3.2.4 Gas sensor characterization

Gas-sensing tests were carried out towards H_2, CO and EtOH, three analytes that could be involved in different processes, such as the production of hydrogen from fossil fuels, or the conversion of EtOH into H_2 in proton-exchange fuel cells.

To understand the effect of the temperature on the response of non-functionalized and functionalized sensors, gas-sensing tests to H_2, CO and EtOH, were performed at various temperatures, in the range from 160 to 390 ºC. Overall, the sensor response showed an n-type semiconductor behavior, i.e. decreasing electrical resistance when exposed to these reducing gases. Besides, the sensor response displayed quite stable and reproducible responses along the test cycles showing standard errors below ±3% for operating temperatures equal or exceeding 220 °C, in contrast to those obtained below 220°C, which showed small and unsaturated responses with slower response and recovery times as typically noticed in MOX-based gas sensors at low temperatures. A comparison of the tendency of the sensor response with temperature for each microsensor (Figure IV.20) suggests the response is influenced by the composition of the sensing film and the tested analyte. Also, it suggests that the temperatures for a maximum-sensor response magnitude for each analyte are shifted according to the composition of material. Consequently, results for non-functionalized sensors showed the highest sensor responses at operating temperatures between 280 ºC and 390 ºC to EtOH, and at 330 ºC and 390 ºC to H_2 and CO, respectively. Similarly, Pt-functionalized sensors showed the highest responses between 330°C and 390 ºC to H_2 and EtOH, and at 330 ºC to CO, whereas Au-functionalized sensors showed their highest responses at the same temperature (390 ºC) to H_2, CO or EtOH.

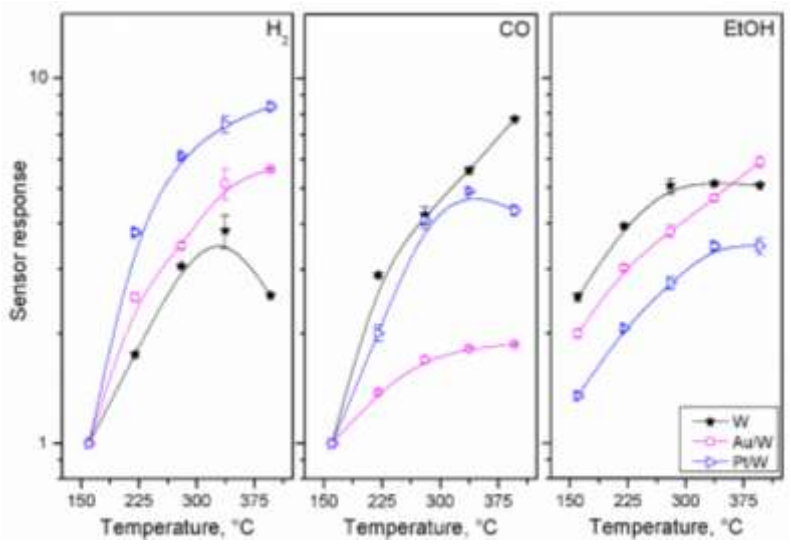

Figure IV.20. Sensor responses and error bars to 500 ppm of H_2, 500 ppm of CO and 80 ppm of EtOH as a function of the operating temperature.

The relationship between the sensor response and concentration at 330°C for H_2 and 390°C for EtOH, and CO is illustrated in Figure IV.21. These results show an exponential change of the response with respect to the gas concentrations, suggesting a saturation of the response as the analyte concentration increases, which represents a normal behavior in MOX-based gas sensors. Results in Figure IV.21 also show that the response of non-functionalized sensors is enhanced to H_2 and EtOH by its functionalization with gold NPs and platinum NPs, respectively, whereas results for CO show the opposite behavior.

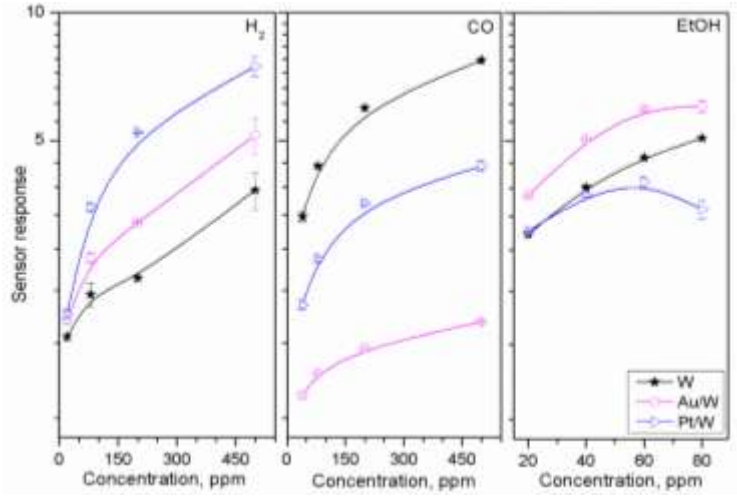

Figure IV.21. Sensor responses to various concentrations of H_2, CO and EtOH.

From the results presented in Figure IV.20 and Figure IV.21 it is difficult to select one of these materials as the best option either for EtOH, H_2 or CO detection, due to the fact that the magnitude of response varies differently for each type of material with temperature. However, taking into account the higher operation temperatures, where the dynamics of the sensor response are faster, results suggest that non-functionalized tungsten oxide sensors are more suitable to sense CO, whereas Au-functionalized sensors are better for EtOH and Pt-functionalized sensors for detecting H_2 [128]. This is in line with previous observations for non-functionalized and functionalized tungsten oxide, grown in a 'hot-wall' reactor, in which it was noticed the same affinity between these materials and analytes [11]. The slightly smaller response magnitudes for sensors fabricated via localized heating compared to those in 'hot-wall' reactor could be related to the differences (i.e. size of the membrane, heater design and heating material) of the microsensor platform, although it is worth noting that the response registered with these sensors to H_2, CO and EtOH is in the same order of magnitude than those reported in the literature [42, 46]. Figure IV.22 displays an example of the response and repeatability of the sensors to H_2, CO and EtOH operating at the maximum temperature studied (the base resistance of the sensors at this temperature were ~203KΩ for WO_3 , ~427 KΩ for WO_3/Au and ~321 KΩ for WO_3/Pt, showing low drifts during the testing period with standard errors below ±7%).

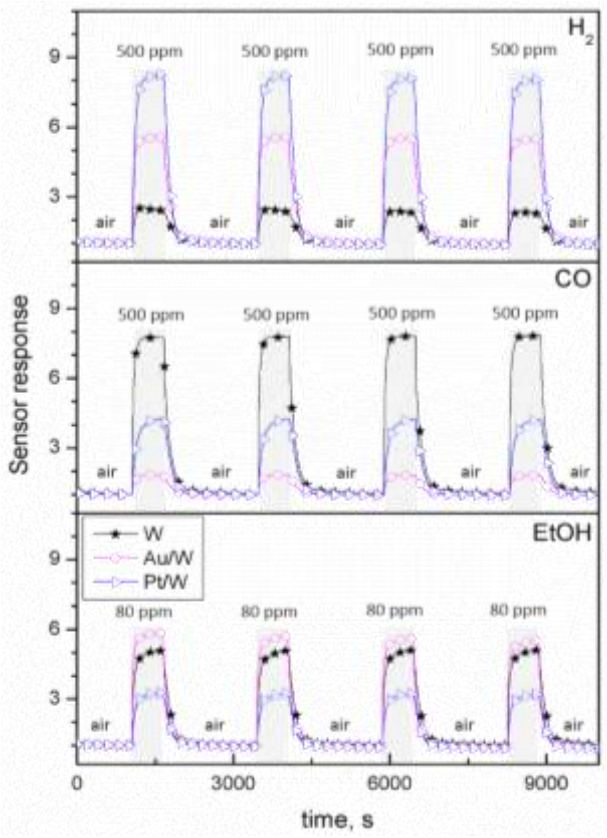

Figure IV.22. Film-resistance changes towards H_2, CO and EtOH, at 390 °C.

Humidity tests were performed for CO at 390 °C in the presence of 50% and 90% of relative humidity (RH). Overall these results were characterized by stable baseline resistances with reproducible resistance changes when exposing the sensors to 500 ppm of CO, similarly to those observed for test under dry air (Figure IV.22). However, the sensor response showed different magnitudes, compared to those recorded for the same gas and concentration tested in dry air, and for instance, at 50 % of RH, the response of the sensors was increased by 18 % for WO_3, 35 % for WO_3/Au and 140 % for WO_3/Pt. These results suggest humidity interferences for these sensors, as noticed before for other MOX-based sensors [15, 128].

Gas-sensing tests show that single microsensors, either employing non-functionalized or functionalized nanostructures, present relatively high cross-sensitivities among H_2, CO and EtOH, which confirms that a selective detection of these analytes using only one sensing element is not possible. In contrast, the cross sensitivities for the same analytes (H_2, CO and

EtOH) become much lower among different microsensors, including non-functionalized and functionalized elements, which suggest analytes could be selectively detected by correlating the response of these microsensors. Consequently, to evaluate the correlation between sensor responses and selectivity of the microsensors, a principal component analysis (PCA) was performed using an autoscaled pre-processing technique to the dataset of the sensor response replicates to each analyte and concentration (48 measurements × 3 variables). A visual appraisal of the discrimination of each analyte and its concentration using the array of microsensors (i.e. based in non-functionalized and functionalized with gold and platinum NPs) is depicted by the scores (Figure IV.23.a), that is, the projections of measurements in an orthogonal base of PCs, and although the loading of each microsensor to the principal components (Figure IV.23.b) show the sensors have a certain degree of correlation, it can be noticed that the differences in the sensing properties of each sensor provide complementary information to discriminate H_2 and EtOH from CO. Carbon monoxide is a typical contaminant gas that arises in the production of H_2 from natural gas or ethanol (e.g. proton-exchange fuel cells) and its selective detection could be particularly important in this growing market, in which gas sensors based on semiconductors are attracting much interest [128].

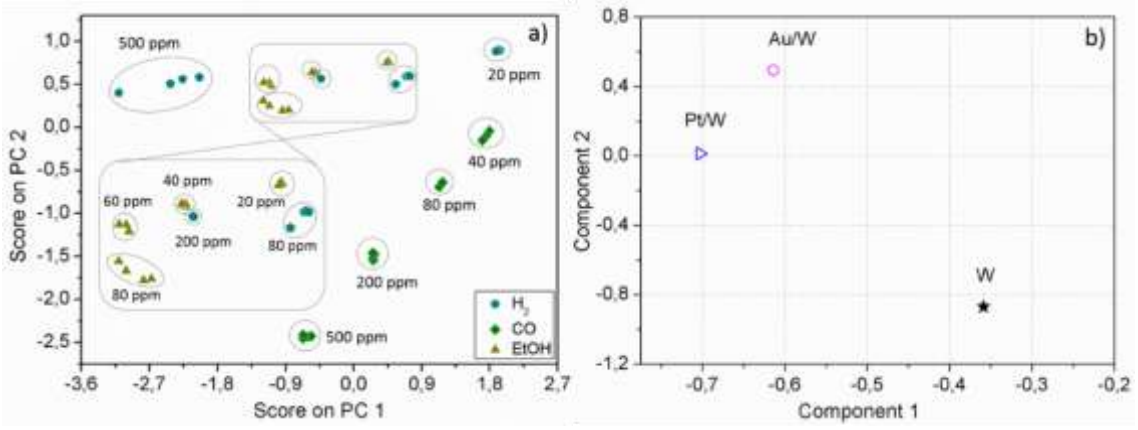

Figure IV.23. PCA analysis of the sensor response displaying the scores or projections of measurements in an orthogonal base of PCs (a) and loading of each sensor to the PCs (b).

4.4 Summary

In summary, AACVD technique has shown its ability to reproduce functionalized and non-functionalized WO_3 NNs with very similar characteristic both in the morphology, the structure and in the gas sensing properties. Moreover, $W(CO)_6$ has shown its suitability and conformability to successfully synthetizes WO_3 NNs via AACVD method. The morphological and structural results are in good agreement with those obtained in previous work where $W(OPh)_6$ had been used as precursor.

Owing to the lower temperature used in AACVD, compared to CVD methods, flexible polymeric substrates were successfully coated by a direct growth of either Pt or Au NPs functionalized WO_3 NNs. The morphology and the structures of the obtained materials were similar to the ones reported for alumina sensors, while the gas sensing results were highly enhanced toward H_2 and ethanol.

AACVD induced by localized heating of the microsensor devices has demonstrated its capability to grow locally into the sensing active area non-functionalized (WO_3) and functionalized nanostructures with gold or platinum NPs (WO_3/Au and WO_3/Pt). The use of this method has simplified the processing steps, has optimised the material usage and consequently has reduced the processing time. Tests of these microarrays towards various concentrations of reducing gases show stable and reproducible responses, with the highest responses (R) for WO_3 to carbon monoxide (e.g. R=4.3 to 80 ppm), for WO_3/Au to ethanol (e.g. R=7 to 80 ppm) and for WO_3/Pt to hydrogen (e.g. R=3.6 to 80 ppm). Principal component analysis of the sensor response replicates to each gas and concentration suggest that the differences in the sensing properties of each element of the array provide the complementary information to discriminate H2 and EtOH from CO.

Chapter 5: Cu_2O and Pd nanoparticle functionalized tungsten oxide (WO_3) nanoneedles synthesized via aerosol assisted-CVD, and used for gas sensing application

5.1 Introduction

The growth of functionalized, nanostructured materials employs various conceptual routes based either on the synthesis and combination of the components separately (multi-step) or by direct synthesis of the functionalised material (single-step). Herein, we study the functionalization of WO_3 NNs with either cuprous oxide (Cu_2O) or palladium (Pd) NPs, using different routes of AACVD method. In the first part of this chapter the results on the film analysis and gas sensing characterization of Cu_2O NPs functionalized WO_3 NNs are discussed, whereas, the second part was dedicated to study the optimal conditions for the growth of high quality WO_3 NNs decorated with well dispersed Pd NPs. Furthermore, the gas sensing characterization toward H_2 is reported.

5.2 Cu_2O NPs functionalized WO_3 NNs synthesized via aerosol assisted-CVD and used for H_2S detection

The use of n-type metal oxide nanomaterials functionalized with p-type, cupric oxide nanoparticles has been reported to be advantageous for detecting hydrogen sulphide. Herein, we report on the direct growth of WO_3 NNs decorated with p-type Cu_2O nanoparticles onto MEMS hotplates in a single step, by using AACVD. To the best of our knowledge, CVD

routes have not been used before to grow WO_3 NNs and simultaneously decorate them with nanoparticles of copper oxides, all in a single step and avoiding a further oxidation step. SEM, XRD, TEM, HRTEM, XPS and NEXAFS-TXM, have been employed to determine phase composition, morphology and microstructure of the as nanoneedle mats. Their gas sensing properties toward H_2S both in dry and humid backgrounds have been studied, together with their response to other gases or vapours. Finally, in light of the experimental findings, a sensing mechanism for hydrogen sulphide in Cu_2O-decorated WO_3 NNs is introduced and discussed.

5.2.1 Material characterization

Pure WO_3 NNs were obtained from the AACVD of $W(CO)_6$ at 500 °C. WO_3 NNs decorated with Cu_2O were grown in a single step, at a moderate temperature of 380 °C from the AACVD of a mixture of $W(CO)_6$ and $Cu(acac)_2$. The as-deposited films (WO_3 and Cu_2O/WO_3) were strongly adherent to the substrate, with dark blue and dark maroon-blue colour, respectively. After annealing at 500 °C for 3 h, the colour of both samples changed, and became white-yellow. The morphology of the synthesized materials was characterized by scanning electron microscopy. Figure V.1 depicts the SEM images obtained from the as-deposited layers. The results confirm the formation of a thick layer of non-aligned nanoneedle-like structures, with high density and homogenous distribution over the substrate. The nanoneedles of pure tungsten oxides (Figure V.1.a and c) were ~11 microns long and their diameter varied between 50-100 nm. Cu_2O/WO_3 nanoneedles (Figure V.1.b and d), were 5 microns long with a thicker diameter that ranged between 50 and 240 nm, agglomerates of two, three or more nanoneedles are also visible. This difference in the morphology of the nanoneedles grown in functionalized and non-functionalized samples could be attributed to the growth temperature and/or the solvent used [129].

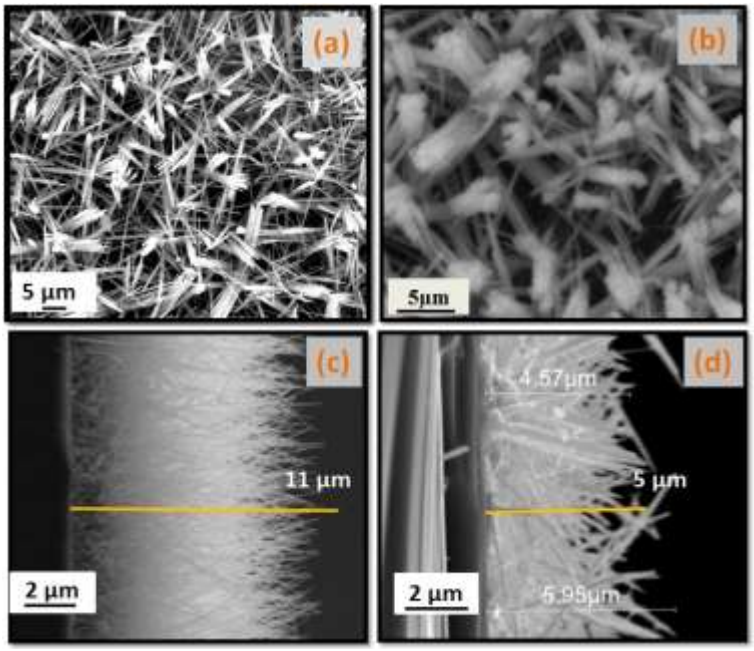

Figure V.1. SEM images of the as-deposited (a) pure WO_3 NNs, (b) Cu_2O functionalized WO_3 NNs, (c) cross-section of pure WO_3 NNs, and (d) cross-section of Cu_2O functionalized WO_3 NNs.

X-ray diffraction (XRD) analysis (Figure V.2) of the different samples indicated the formation of monoclinic-phase WO_3 nanoneedles (P21/n (14) space group, with typical cell parameters of a= 0.729 nm, b=0.7539 nm, c=0.7688 nm, and β=90.91º; ICCD card no. 72-0677). From the pure WO_3 pattern, it is clear that the nanoneedles were strongly oriented in the (002) direction, showing an intense diffraction peak at 23.10° 2θ. Furthermore, a strong platinum reflection at 39.9° 2θ was observed, which was coming from the electrodes. For the pattern recorded from the functionalized sample, the nanoneedles were randomly oriented, with the absence of any reflections from copper oxides.

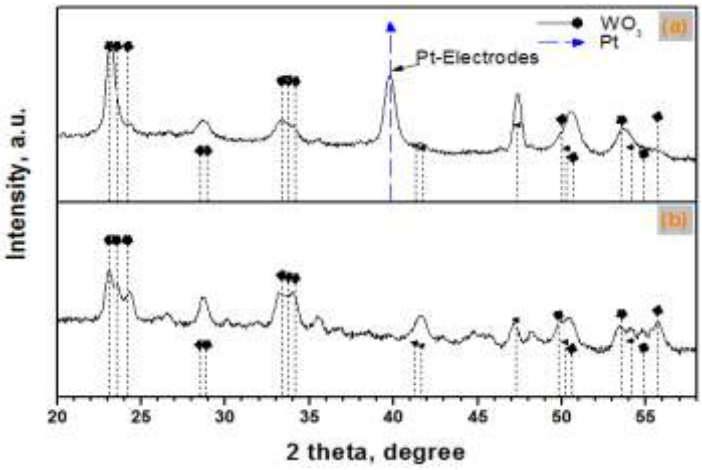

Figure V.2. XRD patterns of (a) pure WO_3 NNs, and (b) Cu_2O functionalized WO_3 NNs.

Elemental and chemical characterizations of the films were performed by XPS. Here, we do not show the XPS and HRTEM results obtained from pure WO_3 film, since they were similar to the ones reported in a previous paper from my group [130]. Figure V.3.a shows the W 4f XP spectrum recorded on a Cu_2O/WO_3 sample and its fitting analysis. To reproduce the spectrum, two doublets, a singlet and the Shirley background were employed. The component centred at 38.6 eV is due to photoelectrons emitted from the W 5p3/2 core level. The highest intensity doublet peak (W 4f7/2), centred at 35.5 eV, is generated by photoelectrons emitted from W atoms with the oxidation state +6, i.e., stoichiometric WO_3 [131]. Therefore, the W ions have their 5d shell empty, i.e., there are no cation d-electrons available to be transferred to adsorbates. The second W 4f doublet, found at 2 eV lower binding energy, is generated by photoelectrons emitted from W atoms with the oxidation state +4 [132]. In this case, the d-electron orbitals on adjacent cations are partially occupied. These reduced cations provide active sites for chemisorption and catalytic activity, i.e., determine the gas-sensing activity of the films [133]. From the area ratio of the components used to fit the W 4f peak we evaluated that near 35% of the tungsten atoms have the oxidation state +4, thus contributing to gas detection. This result is supported by the analysis of the O 1s XP spectrum that is reproduced by two singlets (Figure V.3.b), the first component is centred at 530.5 eV and it is assigned to

the oxygen atoms that form the strong W¼O bonds in the oxide [134]. The second component at about 531.7 eV (37% of the total O 1s area) has been attributed to O atoms in sub-stoichiometric WOx (x<3) structures [129,135].

Figure V.3.c shows the Cu 2p core level spectrum, which consists of two sets of peaks: a low intensity doublet at 942.6 eV and 962.8 eV, which corresponds to CuO, and a more intense doublet which components are centred at 932.6 and 952.3 eV, which corresponds to either Cu metal or Cu_2O.

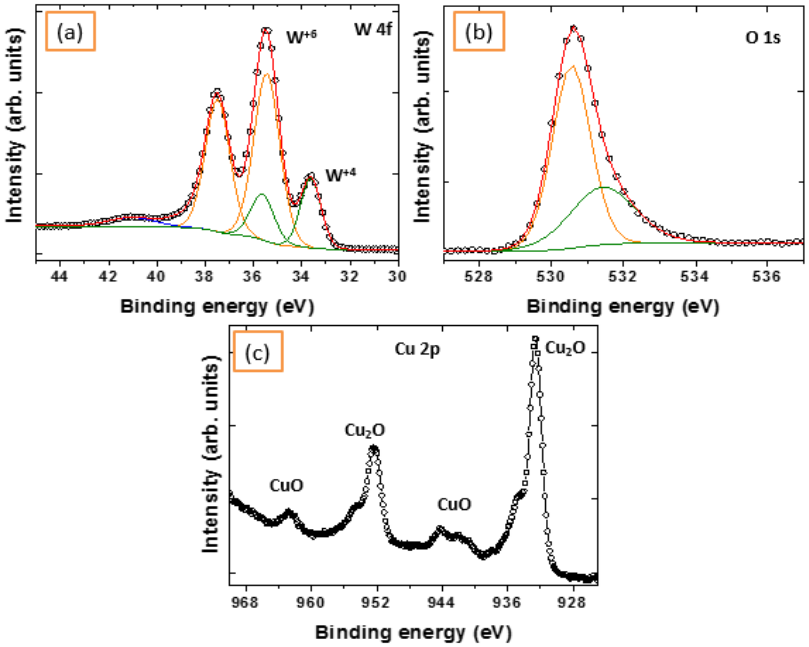

Figure V.3. Typical XPS spectra of the Cu_2O nanoparticles decorated WO_3 NNs (a) W 4f, (b) O 1s, and (c) Cu 2p.

In order to experimentally clarify to which oxidation state belongs this doublet, we have analyzed our sample by NEXAFS-TXM. NEXAFS probes the density of states (DOS) of partially filled or completely unfilled electronic states and is very sensitive to the local bonding environment, particularly to the number of valence electrons, the symmetry and coordination number of the material structural unit cell [136]. Figure V.4 illustrates the copper L-edge NEXAFS spectrum, which is characterized by a low intensity feature at ~ 930.8 eV

attributed to CuO and two relative intense features at ~ 932.8 and ~ 953.5 eV. These two intense features that arise from the dipole transitions of the Cu 2p3/2 and Cu 2p1/2 core levels into the empty d-states were associated to the presence of Cu_2O as reported in [137]. Therefore XPS and NEXAFS analysis together testify for the presence of CuO and Cu_2O in the sample, with 88% of the Cu atoms in the Cu_2O form and 12% in the CuO form [129].

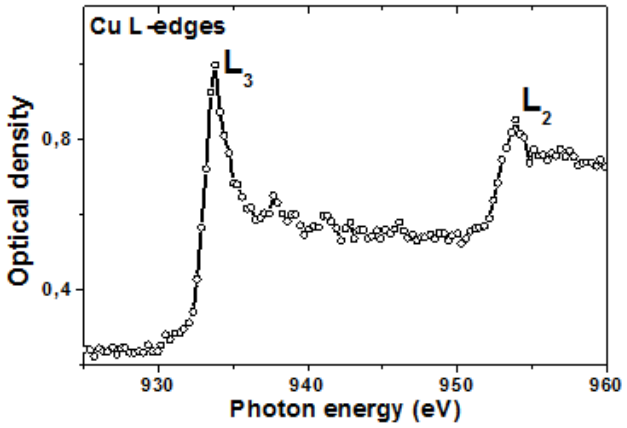

Figure V.4. NEXAFS-TXM spectrum of Cu L-edges of nanoparticles decorated WO_3 NNs. The energy separation between L_3 and L_2 is 21.0 eV which is characteristic for Cu_2O.

Details of morphological and structural features of Cu_2O decorated WO_3 nanoneedle mats were studied by TEM and high resolution TEM. Figure V.5.a and b display the low-magnification TEM images of Cu_2O/CuO nanoparticles decorating the nanoneedles. The formation of nanoparticles with average diameter of about 2-3 nm, and the existence of few bigger ones with diameter about 7 nm can be observed. In addition, a thin amorphous layer surrounding the nanoneedles can also be seen, the formation of which can be associated to the combustion of the solvents during the AACVD process. The analysis of high resolution TEM images (Figure V.5.c and d) reveals the coexistence of Cu_2O and CuO crystallites in the Cu_2O/WO_3 nanoneedle mats [129].

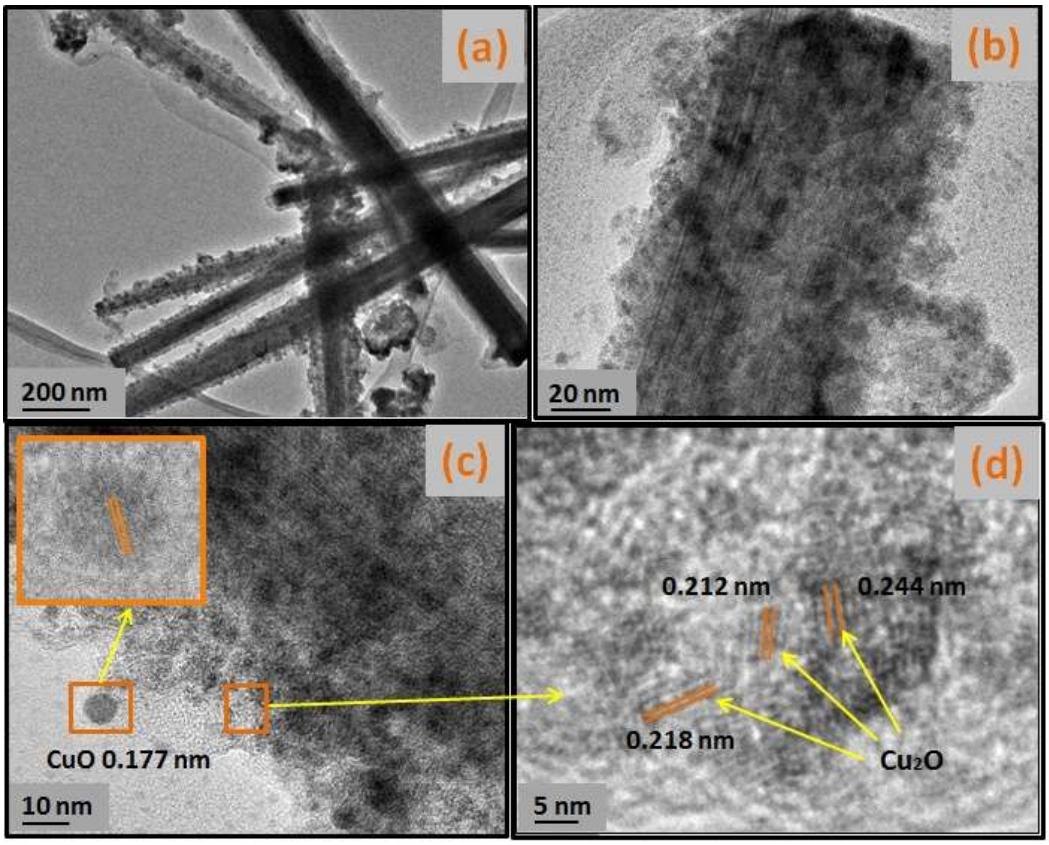

Figure V.5. TEM and HRTEM images of the obtained Cu_2O functionalized WO_3 nanoneedles, (a&b) low magnification and (c&d) high magnification.

As derived from TEM images, the fringe patterns with the interspacing distances of 0.218, 0.244 and 0.212 nm are similar to the interplanar distances of the (200), (111) and (200) lattice planes of Cu_2O respectively (ICDD-PDF Card Nº. 00-005-0667), whereas, that with interspacing distance of 0.177 nm is in a good agreement with the interplanar distance of the (112) lattice planes in bulk crystalline CuO (ICDD-PDF Card Nº. 00-045-0937). Hence, these results suggest that the smaller nanoparticles which represent the vast majority correspond to Cu_2O and the larger ones correspond to CuO. As a summary, XPS, NEXAFS-TXM and HRTEM results imply that both CuO and Cu_2O co-exist in the samples with Cu_2O being more profuse [129].

5.2.2 Gas sensing characterization

The gas sensing properties toward 5 ppm of H_2S of pristine WO_3 and Cu_2O functionalized WO_3 NNs were examined at operating temperatures ranging from 270 to 390 ºC. The maximum operating temperature was selected to ensure the safe operation of the sensor transducer (i.e., avoiding membrane damages or drift in the heating element). The results are shown in Figure V.6.

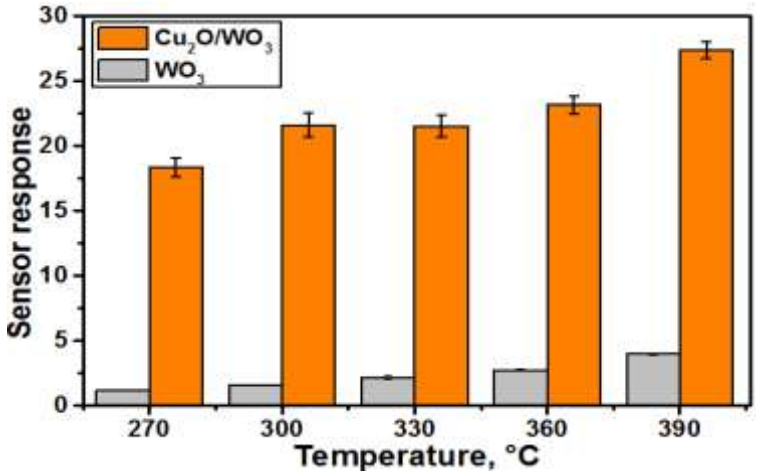

Figure V.6. Sensor responses and error bars to 5 ppm of H_2S as a function of the operating temperature.

Cu_2O/WO_3 samples showed stable and very high responses all over the operating temperatures tested. In contrast, pure WO_3 NNs displayed good and stable responses at temperatures equal or exceeding 280 ºC, while below this value, they exhibited unsaturated responses, with drift in the baseline resistance. For the range of temperatures tested, sensor response increases when the operating temperature is increased. Generally, in metal oxides, the optimal working temperature depends on the quantity of the adsorbed oxygen ionic species and the energy needed to enable the reactions between these ionic species and a target gas. The highest response recorded from pristine WO_3 samples toward 5 ppm of H_2S was 4,

while it reached 27.5 for Cu_2O/WO_3 NNs. Thus, the decoration with Cu_2O nanoparticles of WO_3 NNs has resulted in a 7-fold increase in sensor response.

In the subsequent studies, 390 °C was chosen as the optimal working temperature of the sensors. Figure V.7 depicts the responses obtained from the sensors to various concentrations of H_2S, at the optimal working temperature. The insets show the curves of the response versus concentration. From these results, it is evident that the gas sensor response increases when the concentration of the analyte is increased. Furthermore, at ppb levels (100 and 500 ppb), pristine WO_3 was not able to detect H_2S, whereas by the addition of Cu_2O, the detection limit has been improved and is now below 300 ppb.

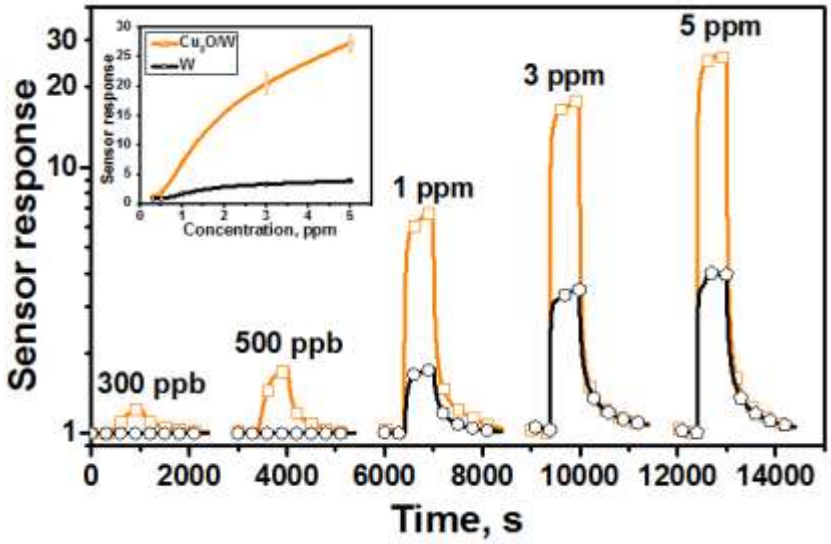

Figure V.7. Sensor response to various concentrations of H_2S at 390 °C. The inset shows the curves of the response vs. concentration.

Figure V.8 shows an example of the responses recorded from pristine WO_3 and Cu_2O/WO_3 sensors toward 1 ppm of H_2S at 390 °C. Overall, the sensors behave as an n-type semiconductor, i.e. decreasing the resistance when exposed to a reducing gas (H_2S). The sensors displayed stable and reproducible responses, and no drift in the response was observed. It is well known that the quality of the semiconductor based gas sensor material

affects the stability of the sensor and thus, the high crystallinity of our WO_3 NNs is responsible for the high stability of the sensors.

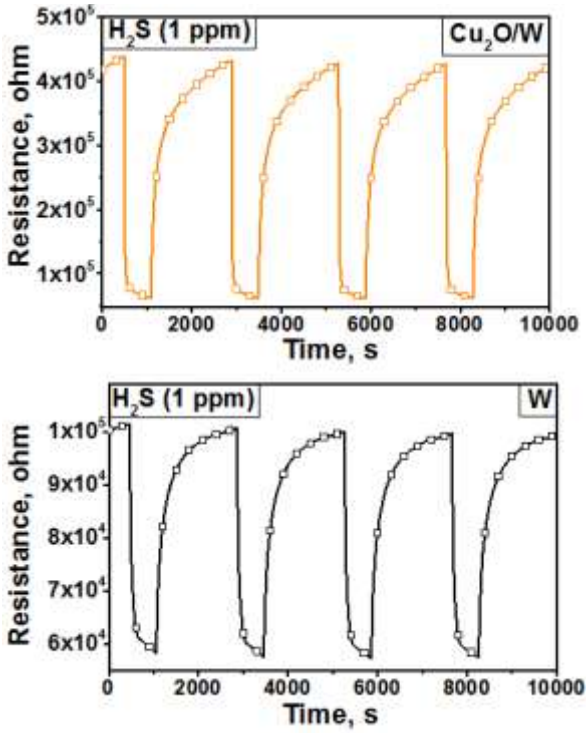

Figure V.8. Example of the responses recorded from pristine WO_3 (bottom) and Cu_2O/WO_3 (top) sensors toward 1 ppm of H_2S at 390 °C.

In addition, we can see from the response curves that the decoration with Cu_2O nanoparticles of the WO_3 NNs results in the baseline resistance of the sensor being increased. Cu_2O is a well-known p-type semiconductor and WO_3 is an n-type one, thus, p-n junctions are formed at the interfaces of the Cu_2O/WO_3 nanocomposite [129]. The formation of these, leads to the appearance of a space charge layer around each Cu_2O/WO_3 interface, which decreases the free electrons in the conduction band of WO_3 NNs and, therefore, increases the baseline resistance of the sensor [138]. At 5 ppm of H_2S, the response and recovery times were calculated for pristine and decorated WO_3 NNs (Figure V.9). The results indicate that Cu_2O decorated samples responded nearly six times faster (i.e., 2 s) than non-functionalized samples (i.e., 11 s). By comparing this result with the ones reported in the literature for metal/ metal oxide NPs functionalized metal oxide nanowires nanocomposite films, it can be concluded

that such a fast response time has not been reported until now [129]. A complete recovery of the baseline resistance was observed within 1100 s after the removal of H_2S, and this for both pristine and decorated samples.

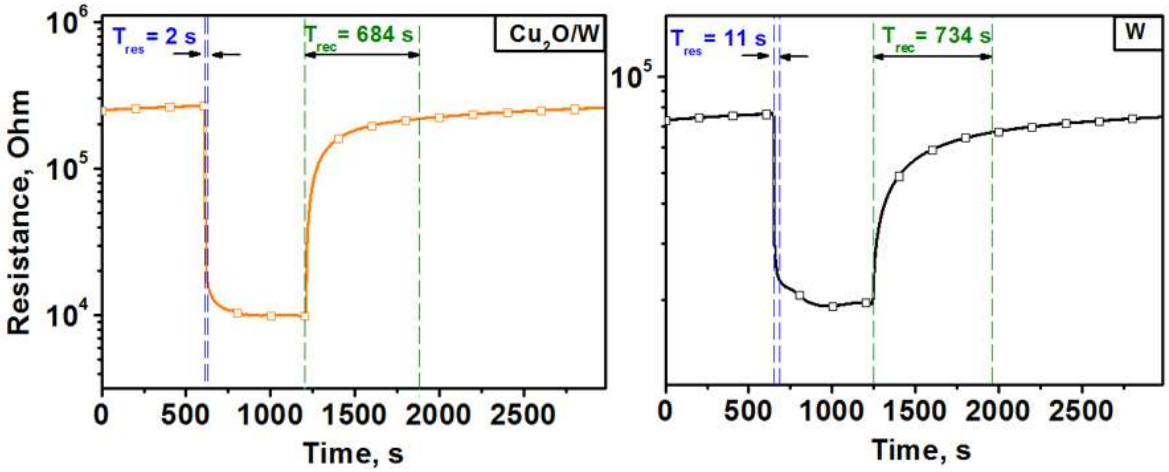

Figure V.9. Enlarged responses of functionalized and non-functionalized WO_3 sensors to 5 ppm H_2S at 390 °C. The response time, Tres, and recovery time, Trec, correspond to the 90% of change in the electrical resistance of the samples.

The selectivity of the sensors toward H_2S was studied by measuring the response to different interfering gases such as H_2 (500 ppm), CO (50 ppm), NH_3 (50 ppm), C_6H_6 (30 ppm) and NO_2 (40 ppb). All these concentrations are much higher than those one could expect to find in ambient air [139]. As shown in Figure V.10, it is clear that Cu_2O decorated WO_3 NNs sensors are more sensitive to low concentration of H_2S (5 ppm) than to the high concentrations of the interfering gases.

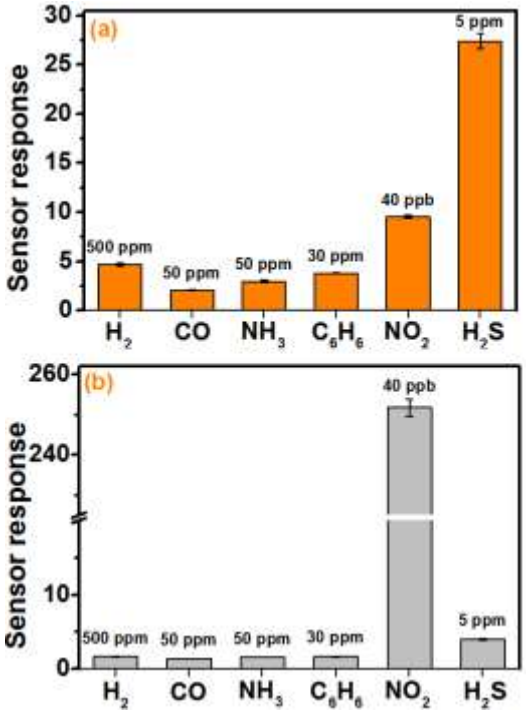

Figure V.10. Selectivity diagram of functionalized and non-functionalized WO_3 gas sensors toward different gases at 390 ºC.

The response of the Cu_2O/WO_3 sensor to H_2S is almost 7 times higher than to H_2 and C_6H_6, 13 times higher than to CO, and 9 times higher than to NH_3 vapours. It is worth noting that Cu_2O decorated WO_3 NNs show significant cross-sensitivity to NO_2, as opposed to pure WO_3 NNs, which show an ultra-high sensitivity toward trace concentrations of NO_2 (i.e., more than one hundred times higher than to the other species studied). Therefore, the combination of two sensors, namely, a Cu_2O decorated and a pristine WO_3 NNs sensor in a H_2S detector would enable the suppression of the NO_2 cross-sensitivity.

5.2.3 Gas sensing mechanism

It has been shown that Cu_2O decorated WO_3 NNs exhibit a remarkably improved H_2S response when compared to pristine WO_3 NNs. To explain the sensing mechanism for hydrogen sulphide, the surface adsorption and reaction model illustrated in Figure V.11 is suggested. When pristine WO_3 NNs are exposed to air, oxygen molecules can adsorb on their

surface and form chemisorbed oxygen species such as O_2^-, O^-or O^{2-}. The nature of oxygen adsorbates depends on the operating temperature (Equation V. 1-4) and, above 300 ºC, the predominant oxygen ions adsorbed are $O^{2-}_{(lattice)}$. Oxygen adsorbates lead to the formation of an electron depletion layer since they trap electrons from the conduction band of the *n*-type tungsten oxide NNs, which makes the material highly resistive.

When the sensor is exposed to H_2S, the chemisorbed oxygen species (O^{2-}*(lattice)*) can react with the reducing gas molecules giving H_2O (g) and SO_2 (g) following Equation 5 [140], while the electrons, originally trapped at oxygen adsorbates will be released, which eventually results in a decrease in the resistance of the NNs mat (Figure V. 11.a).

$$O_{2(g)}O_{2(ads)} \quad (1)$$

$$O_{2(ads)} + e^- \rightarrow O^-_{2(ads)} \; < 100\,°C \quad (2)$$

$$O^-_{2(ads)} + e^- \rightarrow 2O^-_{(ads)} \; 100 < T < 300\,°C \quad (3)$$

$$O^-_{(ads)} + e^- \rightarrow O^{2-}_{(lattice)} \; > 300\,°C \quad (4)$$

$$H_2S_{(g)} + 3O^{2-} \rightarrow SO_{2(g)} + H_2O_{(g)} + 6e^- \quad (5)$$

In contrast, Cu_2O/CuO decorated WO_3 NNs show a different mechanism (Figure V.11.b and c). Cu_2O/CuO nanoparticles and WO_3 NNs are p-type and n-type semiconductor oxides, respectively. The contact between these two different materials leads to the formation of numerous p-n heterojunctions and electron depletion layers at the interface between WO_3 NNs and Cu_2O/CuO nanoparticles. Upon exposure to H_2S, three simultaneous reactions can take place:

One corresponds to the interaction between the studied gas and the chemisorbed oxygen, which is described above the Equation V.5. The two others correspond to the interaction between H_2S molecules and Cu_2O/CuO nanoparticles. According to Equation V.6 and 7,

Cu_2O and CuO are converted to metallic Cu_2S and CuS respectively, by an oxygen/sulphur replacement mechanism [129,141] while the p-n heterojunctions are destroyed. Hence, a large number of electrons is released in the WO_3 NNs and a dramatic decrease in the resistance of the nanocomposite mat can be measured.

$$Cu_2O_{(s)} + H_2S_{(g)} \rightarrow Cu_2S_{(s)} + H_2O_{(g)} \quad (6)$$

$$CuO_{(s)} + H_2S_{(g)} \rightarrow CuS_{(s)} + H_2O_{(g)} \quad (7)$$

In the recovery phase, where synthetic air is flushed to clean the sensor surface, the copper oxides are regenerated according to Equation V.8 and 9, the p-n heterojunctions are restored and the material resistance returns to its original high value [129].

$$Cu_2S_{(s)} + \frac{1}{2}O_{2(g)} \rightarrow Cu_2O_{(s)} + SO_{2(g)} \quad (8)$$

$$CuS_{(s)} + \frac{3}{2}O_{2(g)} \rightarrow CuO_{(s)} + SO_{2(g)} \quad (9)$$

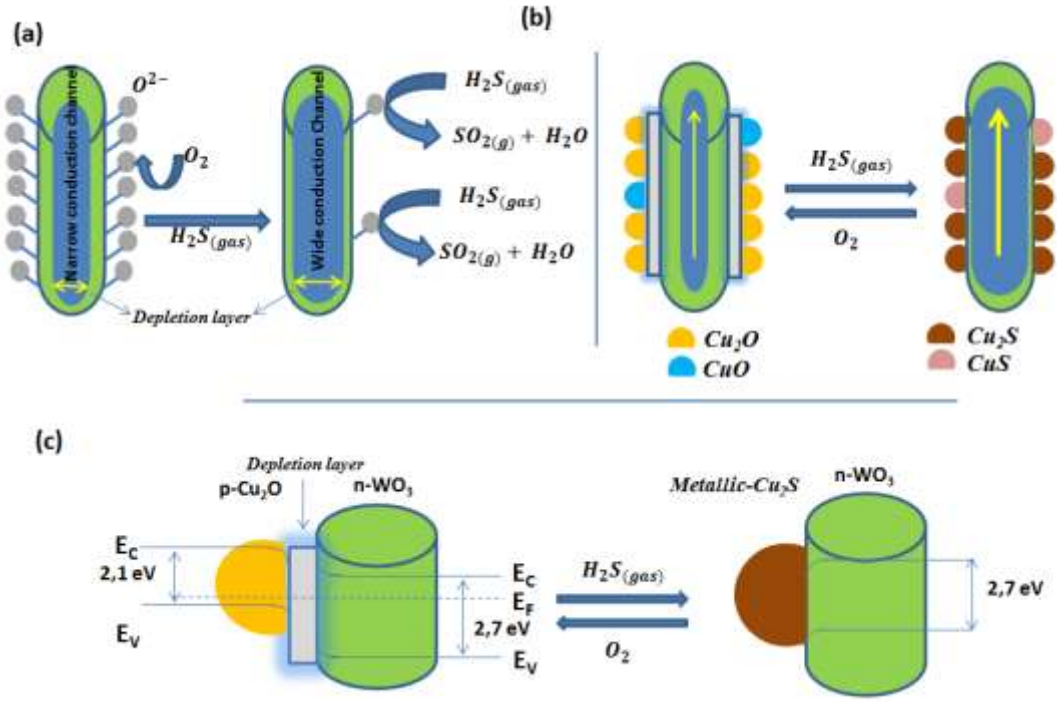

Figure V.11. H_2S gas sensing mechanism of (a) pure WO_3 NNs, (b) Cu_2O/CuO functionalized WO_3 NNs, and an example of the p-n heterojunction of the Cu_2O nanoparticles/WO_3 NNs before and after H_2S analyte (c).

5.2.4 Humidity cross-sensitivity

The influence of water vapour is a key factor to be taken in consideration for the development of chemoresistive metal oxide gas sensors. Ambient moisture can produce notable changes in the electrical properties of metal oxides and dramatically influences sensitivity. To study the effect of humidity, the response of the sensors toward 5 ppm of H_2S at an operating temperature of 390 ºC was monitored both under dry and humid (50% R.H. @ 25 ºC) conditions. Figure V.12 shows two consecutive cycles of response to H_2S and recovery in air under humid and dry conditions.

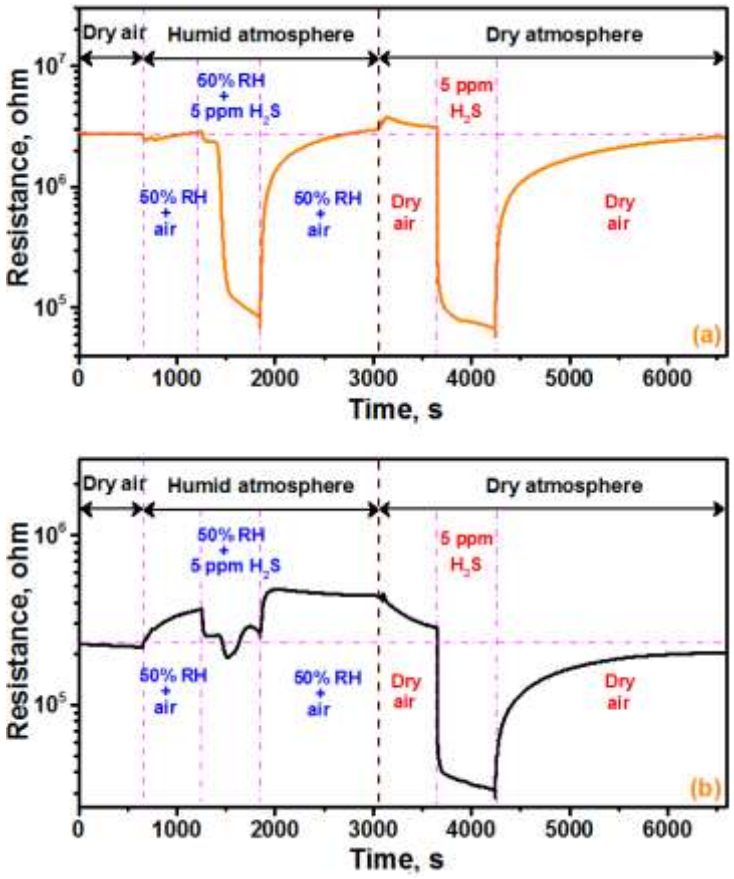

Figure V.12. Sensor resistance variation of (a) functionalized and (b) non-functionalized WO_3 NNs toward dry and humid (50% R.H. @ 25 ºC) atmospheres in a background of synthetic air and 5 ppm of H_2S in synthetic air.

From these results, it can be derived that there is a high influence of ambient moisture on the response of pristine WO_3 NNs. When humid air is introduced in the background, the resistance of the pristine WO_3 sensor is increased by 40% compared to its baseline resistance in dry air. This increase in the resistance under humid conditions has been reported before for SnO_2, ZnO and In_2O_3 [142,143]. Under humid conditions, the response of pristine WO_3 NNs to H_2S is dramatically reduced by 82%, which indicates the occurrence of a competition between water molecules (formation of hydroxyl groups) and H_2S for active sites. It is well-known that there is a high dependence between the effect of humidity on sensor response and the relative surface distribution of hydroxyl groups and oxygen species [142,143]. When

humidity is removed, the baseline resistance is restored and so is sensor response to H_2S. For Cu_2O decorated WO_3 NNs, small changes in the baseline resistance (below 5%) and response to H_2S (below 15%) can be observed when the sensor is operated under humid or dry conditions. The fact that the sensor baseline and the response mechanism to H_2S are dominated by the p-n heterojunctions brought in by the presence of Cu_2O nanoparticles, rather than by surface oxygen species, explains the high immunity of this nanomaterial to dramatic changes in background humidity [129].

5.3 Pd NPs functionalized WO_3 NNs synthesized via aerosol assisted-CVD and used for gas sensing application

In this section, we report on the synthesis and characterization of Pd nanoparticles decorated WO_3 NNs using different precursors (Palladium (II) acetylacetonate and ammonium hexachloropalladate (IV)) and different ways of AACVD functionalization (one step and two steps). The aim of this study was to find the optimal conditions to produce high quality Pd nanoparticles dispersed uniformly along the WO_3 NNs and then to test their gas sensing properties using hydrogen as target gas. The morphology of the deposited films were investigated by means of SEM, and TEM. The elemental and chemical composition were studied by HRTEM, EDX, and XPS. A comparative study was performed between films obtained by different methods.

5.3.1 Material characterization

Four samples of Pd nanoparticle functionalized WO_3 nanoneedles were prepared. Two of them were synthetized by a single step AACVD of $W(CO)_6$ co-reacting with either Palladium (II) acetylacetonate ($Pd(acac)_2$) or ammonium hexachloropalladate (IV) ($(NH_4)_2PdCl_6$). These samples are denoted Pd/WO_3 (Ac-**1SD**) and Pd/WO_3 (Am-**1SD**) respectively. The remaining films were prepared by a two-step AACVD method. In the first one, two layers of pure WO_3

NNs were prepared via AACVD of $W(CO)_6$. After that, the pre-grown nanoneedles were annealed and then functionalized with Pd NPs via AACVD of either Palladium (II) acetylacetonate ($Pd(acac)_2$) or ammonium hexachloropalladate (IV) ($(NH_4)_2PdCl_6$). These samples are denoted Pd/WO_3 (Ac-**2SD**) and Pd/WO_3 (Am-**2SD**) respectively. The experimental conditions have been summarised in chapter III, Table III.3 (Lines 9-12).

The colour of all as-deposited layers was dark blue indicative of partially reduced tungsten oxide (i.e., WO_{3-x}), while after annealing samples for 3 hours in air; their colour changed to white-yellow, indicative of the oxidation of tungsten oxide NN [11,73,74]. Furthermore, the samples were loosely adherent to the glass substrates, since they could be removed by using scotch tape. In addition, no visual change was observed in the films over the course of 5 months.

Figure V.13 displays SEM images of the as-deposited films. In general, all coatings consisted of a thick layer of uniform nanoneedles, distributed homogenously over the substrate. Pd/WO_3 (Ac-**1SD**) NNs were randomly aligned with a diameter size that varied between 40 to 120 nm, and a length of approximately 7 µm, whereas, for Pd/WO_3 (Ac-**2SD**) sample, the nanoneedles were thicker (50–150 nm) and almost two times longer (19 µm) to the previous ones. For Pd/WO_3 (Am-**1SD**) layer, the nanoneedles were thin (60 –100 nm), with non-uniform length and with an agglomeration of big nanoparticles on top of them. In contrast, for Pd/WO_3 (Am-**2SD**) film, the nanoneedles were very long (20 µm) and thick (50–200 nm). In this sample also bundle structures composed from 2–3 nanowires are observed. Therefore, double step deposition has produced thicker and longer nanoneedles in comparison to the ones obtained by single step AACVD, and this dissimilarity observed in the morphology, could be attributed to the deposition temperature which affects the growth rates of the materials [116,129].

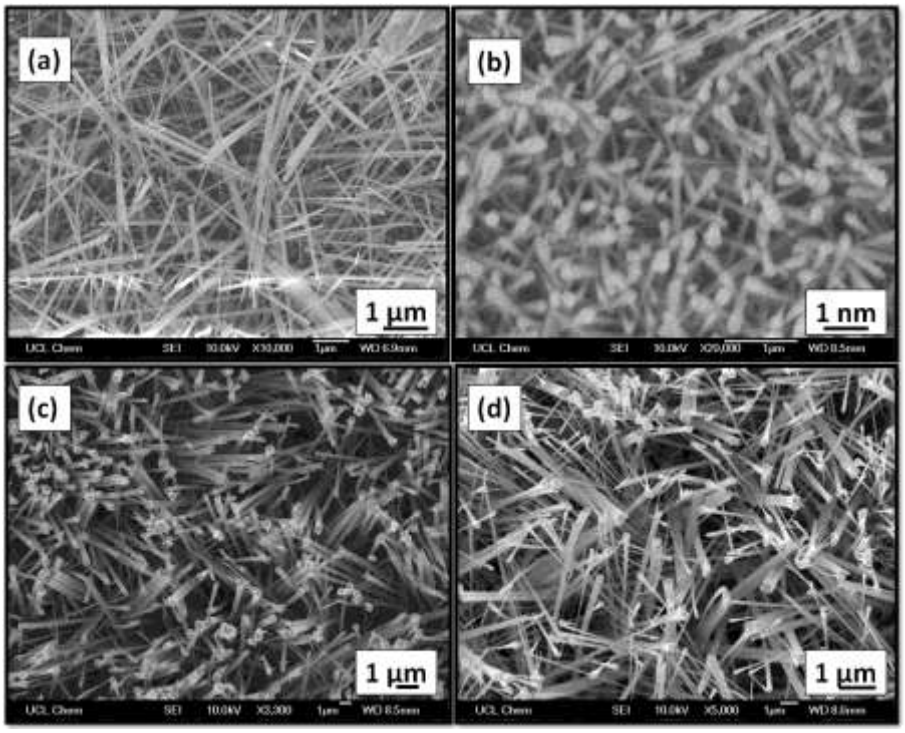

Figure V.13. SEM images of (a) Pd/WO_3 (Ac-**1SD**), (b) Pd/WO_3 (Am-**1SD**), (c) Pd/WO_3 (Ac-**2SD**) and (d) Pd/WO_3 (Am-**2SD**).

In order to obtain more detailed information about the morphology and the elemental composition of the as-synthesized samples, TEM and HRTEM were carried out. Figure V.14 shows the representative TEM images of the as-deposited nanoneedles decorated with Pd nanoparticles. The results revealed the presence of well-dispersed nanoparticles along the surface of the nanoneedles for Pd/WO_3 (Ac-**1SD**), Pd/WO_3 (Ac-**2SD**) and Pd/WO_3 (Am-**2SD**), consistent with results seen previously for gold and platinum NP functionalized WO_3 NNs [11]. However, for the Pd/WO_3 (Am-**1SD**) film, nanoparticles were very big (15–30) and were not well attached to the nanoneedles. Additionally, their production amount was very small in comparison to the other samples, and numerous self-nucleated and isolated particles were frequently observed. It is well known that in the AACVD approach, the solubility is an important criteria for precursor design [74]. $(NH_4)_2PdCl_6$ precursor has shown enough solubility in methanol as opposite to acetone. This fact has generated an instability

and lack of homogeneity between the precursor solutions of WO_3 and Pd nanoparticles. Thus, the insoluble crystals of the Pd precursors were directly transported to the heated zone inside the reactor, and there started to react and form separately these big detached nanoparticles. Overall, the particles displayed approximately spherical morphologies, with sizes between 3–5 nm, 15–30 nm, 4–6 nm and 2–4 nm for Pd/WO_3 (Ac-**1SD**), Pd/WO_3 (Am-**1SD**), Pd/WO_3 (Ac-**2SD**) and Pd/WO_3 (Am-**2SD**) respectively (total measured population was 20 particles). Furthermore, high-resolution TEM images show that single crystalline NNs with uniform lattice structures were obtained for all the samples synthesized. The spacing between adjacent lattice fringes is 0.378 nm, which is similar to the d-spacing of the (020) plane of WO_3 monoclinic phase (JCPDS card no. 01-072-0677), consistent with our previous results [11]. On the other hand, all the NPs were characterized by lattice fringes with interplanar spacing of 0.225 nm corresponding to the (111) plane of face-centred-cubic (fcc) palladium (ICDD card no. 00-046-1043). According to these results, it is clear that either single or double step AACVD methods have successfully demonstrated their efficiency to synthesize Pd nanoparticles from both precursors.

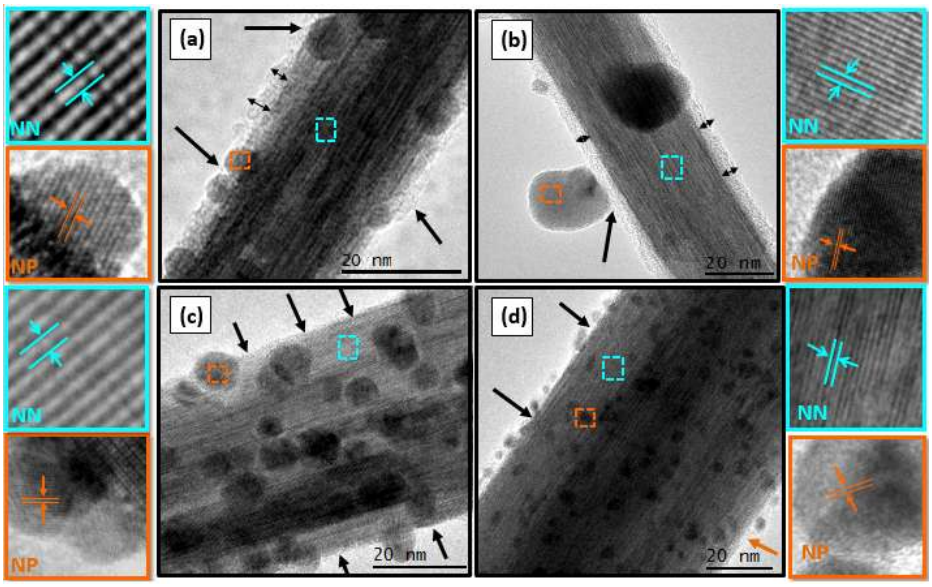

Figure V.14. TEM and HRTEM images of (a) Pd/WO_3 (Ac-**1SD**), (b) Pd/WO_3 (Am-**1SD**), (c) Pd/WO_3 (Ac-**2SD**) and (d) Pd/WO_3 (Am-**2SD**).

Owing to the stability and the high solubility of $Pd(acac)_2$ precursor in methanol and acetone solvents, the nanoparticle size has remained quite the same in both one-step or two-step AACVD methods, whereas, it has changed (i.e. size) by using $(NH_4)_2PdCl_6$) precursor. Furthermore, we have observed the formation of a thick amorphous layer (indicated by black arrows, see Figure V.14) surrounding the nanoneedles of samples grown by single step AACVD method. This can be associated to the combustion of the solvents during the deposition process. However, in the double step AACVD method the amorphous layer was almost completely eliminated, due to the annealing of the nanoneedles before the deposition of palladium nanoparticles. Hence, this finding could further enhance the electrical contact between the nanoneedle and the nanoparticles and could provide better results for many applications that required as deposited films (e.g. metal particles) without further annealing or oxidation.

XPS analysis of the as-deposited and annealed films was conducted. Figure V.15.a displays an example of W 4f spectrum recorded from the as-deposited Pd/WO_3 (Ac-**2SD**) and its fitting analysis. The components centred at 35.4 eV and 37.5 eV are associated to the $4f_{7/2}$ and W $4f_{5/2}$ spin orbit doublet respectively. These values are in good agreement with those found in the literature for W^{+6} in WO_3 stoichiometric films [130]. After annealing, no shifts in the bending energies of the two spin orbits were observed and the composition of the surface remains stoichiometric (Figure V.15.b). The same result was observed from the W4f XP spectrum of Pd/WO_3 (Ac-**1SD**) and Pd/WO_3 (Am-**2SD**) films. Figure V.15.c shows the W 4f XP spectrum recorded from the as-deposited Pd/WO_3 (Am-**1SD**) and its fitting analysis. To reproduce the spectrum two doublets of Lorentzian curves were fitted. The doublet of the highest intensity peak, centred at 35.9 eV and 38 eV corresponded to $4f_{7/2}$ and $4f_{5/2}$

respectively, and were generated by photoelectrons emitted from W atoms with the oxidation state +6, i.e., stoichiometric WO_3 [130]. On the other hand, the small W 4f doublet found at 34 eV and 36 eV were generated by photoelectrons emitted from W atoms in the oxidation state +4, in line with [144]. After annealing (Figure V.15.d), the small doublet corresponding to the oxidation state +4 disappeared and the spectrum had the same features observed from Pd/WO_3 (Ac-**2SD**) film, which indicates the full oxidation of surface layer.

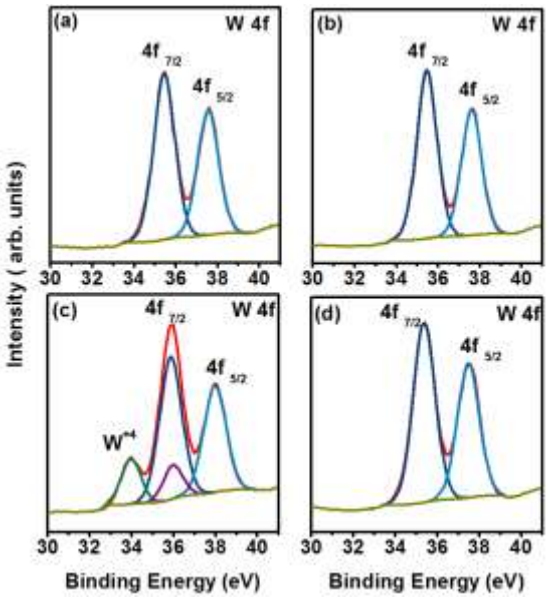

Figure V.15. XPS W 4f core-level spectra of (a) as deposited Pd/WO_3 (Ac-**2SD**), (b) after annealing, (c) as deposited Pd/WO_3 (Am-**1SD**) and (d) after annealing.

Figure V.16.a depicts the Pd 3d XPS spectrum recorded from the as-deposited Pd/WO_3 (Ac-**1SD**) film. This could be fitted using one pair of two strong peaks and one singlet. The strong peaks at 335.5 eV and 340.76 eV are assigned to Pd $3d_{5/2}$ and Pd $3d_{3/2}$ for Pd (0) metal respectively [145], whereas, the small peak at 336.2 eV is ascribed to PdO_3 [146]. The XPS spectra of the as prepared Pd/WO_3 (Ac-**2SD**) and Pd/WO_3 (Am-**2SD**) films (Figure V.16.c and e) consist of two deconvoluted doublets respectively. The highest one with components centred at 335.1 eV and 340.4 eV are associated to Pd $3d_{5/2}$ and Pd $3d_{3/2}$ for Pd metal respectively [147], while the short one at binding energy of 336.4 eV and 341.6 eV is

attributed to PdOx [148]. After annealing of the layers at 500 ºC for 3 h, the XPS spectra of the three samples (Figure V.16.b,d and f), were dominated by two strong peaks at 336.9–342.2 eV, 337.1–342.4 eV and 336.9–342.1 eV for Pd/WO_3 (Ac-**1SD**), Pd/WO_3 (Ac-**2SD**) and Pd/WO_3 (Am-**2SD**) films respectively[149-150]. These binding energies correspond to Pd $3d_{5/2}$ and Pd $3d_{3/2}$ spin orbits for PdO. Regarding Pd/WO_3 (Am-**1SD**) film, we could not observe any reflections or peaks in the Pd 3d spectrum (low mass production). Thus, for as deposited coatings either by single or double step AACVD, two valence states for Pd species were observed: 0 and 2+. By comparing their relative intensity, it is clear that the majority of the Pd nanoparticles were in Pd(0) state (i.e. metal) for as-deposited samples. In contrast, after the annealing, all Pd nanoparticles were oxidized to Pd(II) (i.e., PdO).

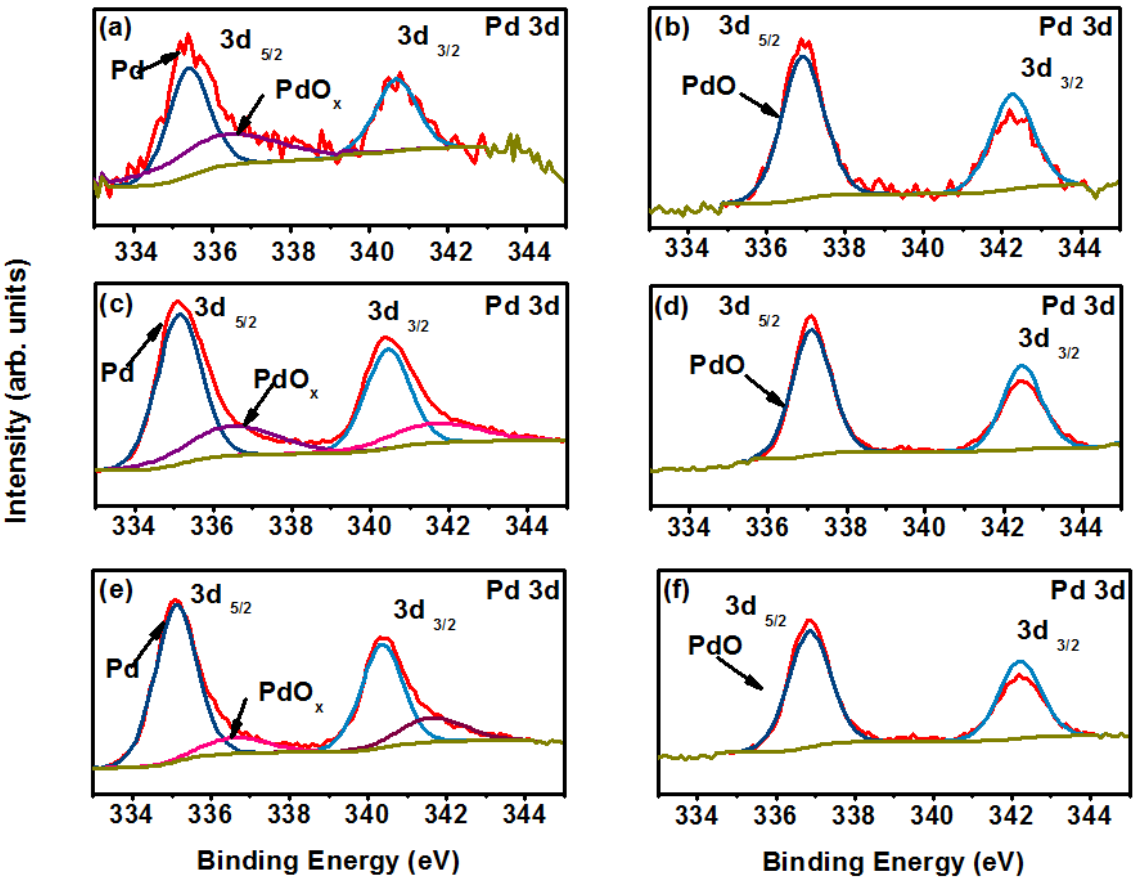

Figure V.16. XPS Pd 3d core-level spectra of (a) as deposited Pd/WO_3 (Ac-**1SD)**, (b) after annealing, (c) as deposited Pd/WO_3 (Ac-**2SD**), (c) after annealing, (e) Pd/WO_3 (Am-**2SD**) and (f) after annealing.

During the HRTEM analysis, we noticed that the amount of nanoparticles found in Pd/WO_3 (Ac-**2SD**) film was higher than in Pd/WO_3 (Ac-**1SD**) (see Figure V.14.a and c). Due to this, we have scrutinized the productivity of Pd nanoparticles by both methods, using $Pd(acac)_2$ as a precursor.

Table V.1 illustrates the weight and the atomic percentage of Pd metal deposited by either single step AACVD (5 mg of the precursor, see Table V.1, line 1) or by double step AACVD method (using different amount of Pd precursor, 5, 7 and 9 mg). At 5 mg of palladium precursor, we can see that the weight and the atomic percentages of Pd metal found in Pd/WO_3 (Ac-**2SD**) film, were 15 and 40 times higher than for Pd/WO_3 (Ac-**1SD**) respectively, which means that only 3% of the Pd weight production can be achieved by using single step deposition compared to double step one. Although, we have remarked that by increasing the amount of precursors by a step of 2 mg, the amount of Pd NPs produced is significantly increased. This finding will have a great impact for applications that need a high level of metal loading, or just to minimise the consumption of expensive, noble metal precursors. Thus, double step AACVD can be considered as a cost-effective way for the functionalization of nanomaterials with noble metal nanoparticles, which is very important for a successful scaling up of the process in view of its application by industry.

Table V. 1. EDX analysis of (1) sample prepared by 1 single step AACVD using precursor 1(5 mg),(b),(c) and (d) samples prepared by double steps AACVD using 5, 7 and 9 mg of $Pd(acac)_2$ precursor respectively.

Sample name	Pd Weight %	Pd Atomic %

(1)	Pd/WO_3 (Ac -**1SD**) – 5 mg	0.40	1.42
(2)	Pd/WO_3 (Ac -**2SD**) – 5 mg	14.76	22.25
(3)	Pd/WO_3 (Ac -**2SD**) – 7 mg	19.45	28.96
(4)	Pd/WO_3 (Ac -**2SD**)– 9 mg	21.39	35.44

5.3.2 Gas sensing characterization

Pristine WO_3, Pd/WO_3 (Ac-**1SD**), Pd/WO_3 (Ac-**2SD**) and Pd/WO_3 (Am-**2SD**) films were directly deposited via AACVD method onto MEMS-based gas sensor substrates. More details about the experimental conditions are mentioned in Table III.3 (lines 13-16). Gas sensing tests were carried out to different concentrations of hydrogen by using dc resistance measurements. The sensors were tested at various sensor temperatures from 50–350 °C, in intervals of 50° C, in order to understand the effect of the temperature on the sensor responses. Four replicate measurements per temperature were performed in order to assess the reproducibility of results. Figure V.17 displays the sensor responses to 500 ppm of hydrogen as a function of the operating temperature. At temperature below 200°C, pristine WO_3 film showed very small responses, especially at 50 °C and 100 °C, where it was not able to detect the analyte. However at temperature exceeding 200 °C, the sensor showed good and saturated responses, their maximum toward 500 ppm of Hydrogen, was achieved at 350°C. This finding indicates the normal behaviour known through pure metal oxide sensors, since they need elevated working temperatures.

For Pd/WO_3 (Ac-**2SD**), Pd/WO_3 (Ac-**1SD**) and Pd/WO_3 (Am-**2SD**) sensors, the responses were increased by increasing the temperature, reaching the maximum at 150 °C, 200 °C and 250 °C respectively, then they start to decrease by increasing the temperature. For Pd/WO_3 (Ac-**1SD**) and Pd/WO_3 (Am-**2SD**) sensors, the responses were very stable, saturated

and reproducible at temperature ranging from 150 -250 °C, while besides this interval, the responses were unstable, showing drifts in their base lines resistance. Pd/WO_3 (Ac-**2SD**) sensor exhibited stable and saturated responses at temperatures below 200 °C, while exceeding this value, the sensor started to be unstable, showing small sensitivity toward the studied analyte. Additionally, this sensor has exhibited good responses at temperatures near to the ambient (50 °C), the response was equal to 23, which is 12 time higher than the maximum response displayed by pristine WO_3 sensor (350 °C).

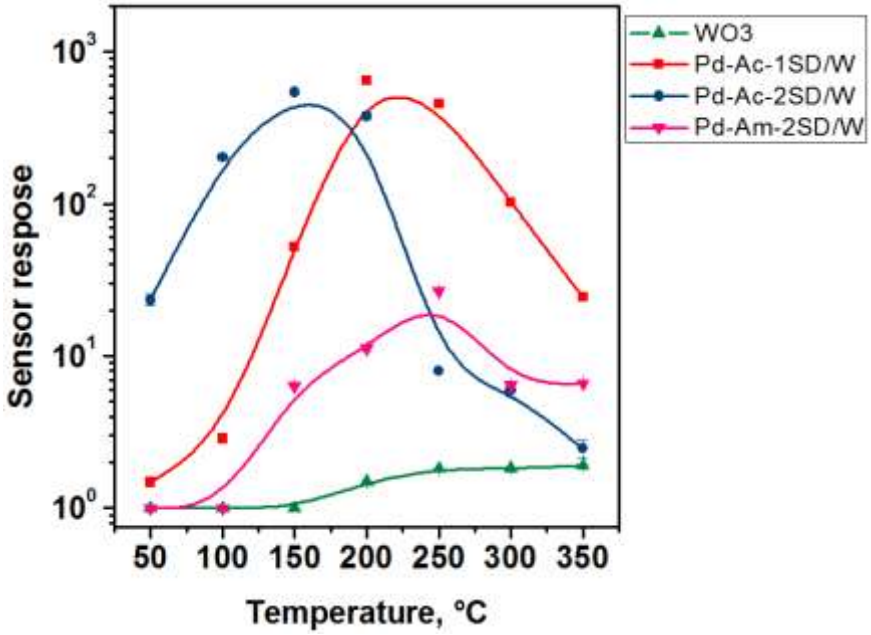

Figure V.17. Sensor responses to 500 ppm of hydrogen as a function of operating temperature.

To study the relationship between the sensor response and the gas concentration, we have exposed our sensors toward various concentrations of hydrogen ranging from 40 to 500 ppm, at working temperatures of 150 °C for Pd/WO_3 (Ac-**2SD**) and 250 °C for the rest of the sensors. Figure V.18 illustrates the sensor responses as a function of the gas concentration. As we can see, by increasing the gas concentration the responses of all the sensors were increased. Furthermore, the slope of the calibration curve (i.e. sensitivity) for pure WO_3 sensors was very small compared to the other sensors; the response was varied between 1.13

and 1.83 for concentrations ranging from 40 to 500 ppm of H_2. In addition, functionalized samples exhibited quite similar tendency regarding the concentration variation. However, sensors functionalized by Pd $(acac)_2$ precursor showed higher responses than the one functionalized by $(NH_4)_2PdCl_6$ precursor. At 500 ppm of H_2, the responses of Pd/WO_3 (Ac-**1SD**) and Pd/WO_3 (Ac-**2SD**) were 18 and 20 times higher than those of Pd/WO_3 (Am-**2SD**) sensor, respectively.

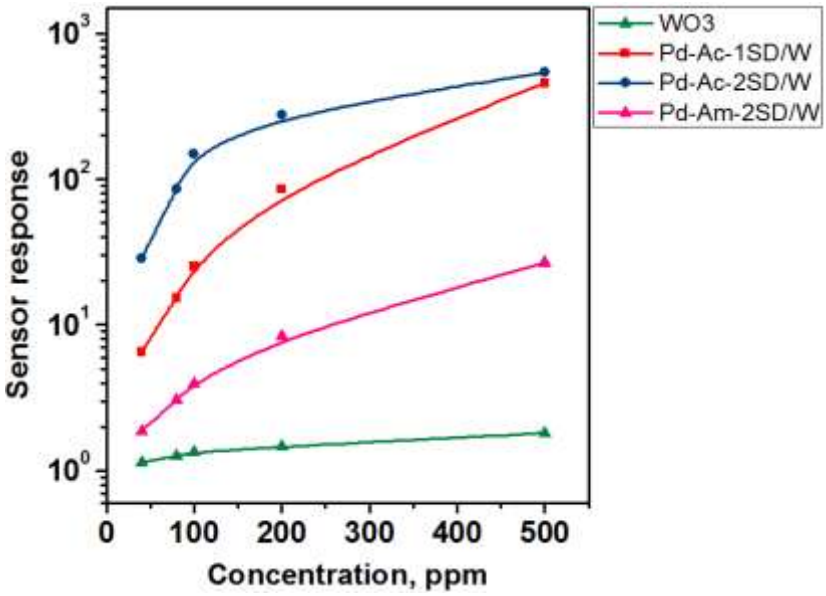

Figure V.18. Sensor responses toward various concentration of hydrogen.

Figure V.19 illustrates an example of the sensors resistance changes toward consecutive concentrations of H_2 gas, ranging from 40 to 500 ppm at operating temperature of 150 °C for Pd/WO_3 (Ac-**2SD**) and 250 °C for the rest of the sensors. The sensors responses showed an n-type semiconductor behaviour, i.e. decreasing electrical resistance when exposed to a reducing gas such as H_2. Furthermore, the sensors showed very stable responses with complete recovery to the baseline resistance. Additionally, it is clear from the graphs (Figure V.19), that the fabricated sensors were able to discern between the various concentrations of the studied analyte, which is in line with the results illustrated in Figure V.18. Moreover, we have studied the reproducibility of the sensor responses by re-exposing them to 80 ppm of H_2.

As it is shown in Figure V.19, all the sensors showed reproducible behaviour, getting good reproducible responses to 80 ppm of H_2 at the beginning and at the end of the repeated detection/recovery cycles. A slight increase in the baseline resistance was observed from the Pd/W (Ac-**2SD**) sensor.

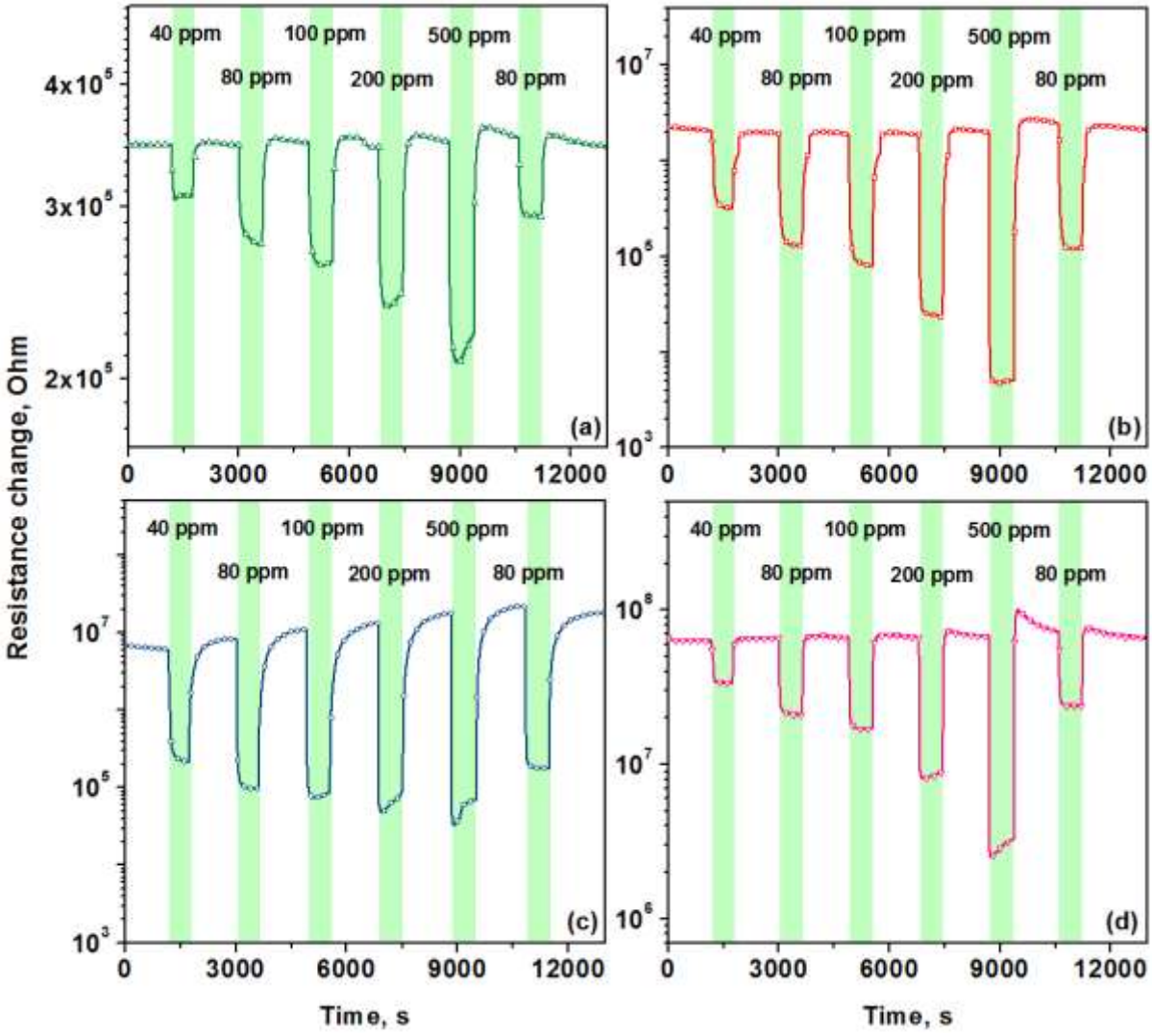

Figure V.19. Film resistance changes (a) pristine WO_3 film, (b) Pd/W (Ac-**1SD**), (c) Pd/W (Ac-**2SD**) and (d) Pd/W (Am-**2SD**), toward various concentrations of H_2.

The selectivity of the sensors toward 100 ppm of H_2 was studied by measuring the response to different interfering gases such as NH_3 (100 ppm), C_6H_6 (200 ppm) and CO (200 ppm) at operating temperature of 150 °C for Pd/WO_3 (Ac-**2SD**) and 250 °C for the rest of the sensors. All these concentrations are chosen with the aim to be higher or equal to the

concentration of the target gas (100 ppm of H_2). As shown in Figure V.20, it is clear that sensors functionalized by using $Pd(acac)_2$ precursor exhibit higher sensitivity toward H_2 (100 ppm) than to the higher concentrations of the interfering gases.

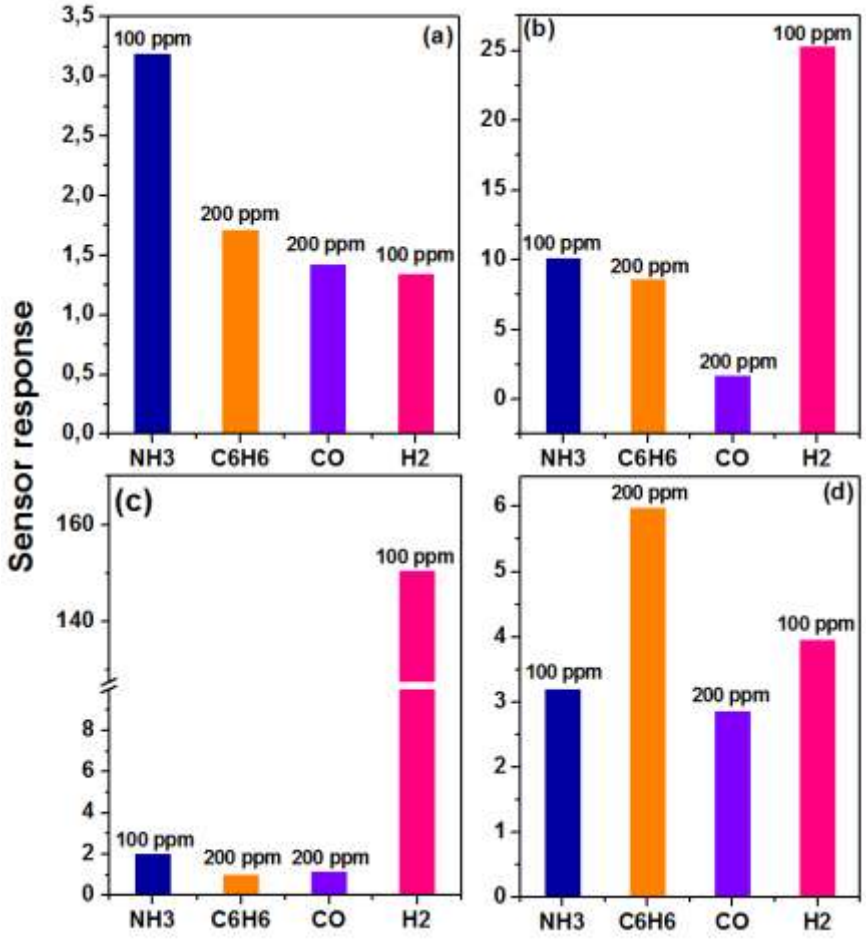

Figure V.20. Selectivity diagram of functionalized and non-functionalized WO_3 gas sensors toward NH_3, C_6H_6 and CO interfering gases,(a) pristine WO_3 film, (b) Pd/W (Ac-**1SD**), (c) Pd/W (Ac-**2SD**) and (d) Pd/W (Am-**2SD**).

The response of Pd/WO_3 (Ac-**1SD**) sensor to 100 ppm of H_2 is almost 2.5 times higher than to NH_3, 3 times higher than to C_6H_6, and 15.5 times higher than to CO gas. Additionally, the response of Pd/WO_3 (Ac-**2SD**) sensor toward 100 ppm of H_2 is almost 76 times higher than to NH_3, 150 times higher than to C_6H_6, and 133 times higher than to CO gas. It is worth noting that Pd/WO_3 (Am-**2SD**) sensor shows significant cross-sensitivity to C_6H_6, while pure WO_3 suffers from a very high cross-sensitivity toward all the interfering gases.

5.4 Summary

As a summary, gas-sensitive hybrid material consisting of Cu_2O nanoparticle-decorated WO_3 NNs is successfully grown via a single step AACVD method. The morphological, structural, and composition analysis show that our method is effective for growing single crystalline, n-type WO_3 nanoneedles decorated with p-type Cu_2O nanoparticles at moderate temperatures (i.e., 380 °C), with cost effectiveness and short fabrication times, directly onto micro-hotplate transducer arrays in view of obtaining gas sensors. The gas sensing studies performed show that this hybrid nanomaterial has excellent sensitivity and selectivity to H_2S (7-fold increase in response compared with that of pristine WO_3 nanoneedles), a low detection limit (below 300 ppb of H_2S) together with unprecedented fast response times (2 s) and high immunity to changes in background humidity. These superior properties arise due to the multiple p-n heterojunctions created at the nanoscale in our hybrid nanomaterial.

Furthermore, palladium (II) acetylacetonate as a precursor appeared to be very suitable for the growth of well dispersed Pd nanoparticles by using either single step or double step AACVD method. In contrast, Ammonium hexachloropalladate(IV) as a precursor has shown its inefficacity to synthesize Pd nanoparticles by a single step process. These results revealed that functionalization using the double step approach opens a simple pathway to incorporate metal nanoparticles from a wide range of precursors with low solubility in organic solvents. Moreover, XPS results have shown that, for as deposited coatings, the majority of the Pd nanoparticles were presented as Pd(0) state, while, after the annealing, all the nanoparticles were oxidized and converted to Pd(II). EDX analysis revealed that the double step route yielded the highest content of Pd nanoparticles compared to their counterpart, which makes it a cost–effective way for being adopted by the industry for the mass production of such nanomaterials. Finally, the well dispersed Pd NPs produced from $Pd(acac)_2$ precursor, using

single or double step AACVD method, have highly improved the gas sensing properties of WO_3 NNs toward H_2, which indicate that the careful choice of the precursors is of a primary importance in the fabrication of reliable gas sensors.

Chapter VI. Conclusions and future works

In this Thesis, the AACVD method was used for the growth of non-functionalized and functionalized WO_3 NNs with either metal or metal oxide NPs, for gas sensing applications. The findings have demonstrated that AACVD is:

1) A flexible, inexpensive and high-yield technique for growing metal oxides with remarkable gas sensing properties.
2) A suitable technique for tuning functionalities (e.g. Au, Pt, Cu_2O and Pd NPs) in metal oxide host matrices within a single step deposition.
3) Compatible with a wide range of substrates including glass, ceramic, flexible polymeric and silicon micro electro-mechanical systems (MEMS).

Moreover, various gases have been used to test the fabricated sensors. The results have shown that functionalized samples have exhibited enhanced gas sensing properties compared to pristine WO_3 sensors. A summary of the findings of this thesis is listed below:

1. Tungsten oxide nanostructures functionalised with Au or Pt NPs have been synthesized, using a single-step AACVD method, onto alumina substrate. The morphology and the structure of the synthesised materials were quite similar to the ones performed at UCL University. Moreover, the gas sensing properties shown from the fabricated alumina sensors (Au/W, Pt/W and W), were comparable to the ones observed from MEMs-based gas sensors. Thus, these results indicate the good reproducibility of AACVD method regarding the morphology, the structures and the gas sensing properties of the synthesised materials.

2. WO_3 NNs have also been deposited from a commercially available hexacarbonyl precursor, using AACVD technique. It was found that by adjusting the solvents, the nanoneedle-like structures can be easily obtained.
3. Owing to the lower temperature used in AACVD, compared to CVD methods, flexible polymeric substrates were successfully coated by a direct growth of either Pt or Au NPs functionalized WO_3 NNs. The morphology and the structures of the obtained materials were similar to the ones reported for alumina sensors, while the gas sensing results were highly enhanced toward H_2 and ethanol.
4. Localized heating, via resistive microheaters, was satisfactorily employed for the AACVD growth of 1D nanostructures (non-functionalized or functionalized tungsten oxide with Au or Pt NPs) on gas sensing microsystems. Results demonstrated that each microsensor provides suitable thermal conditions for the localized synthesis, via AACVD, of high quality functional nanostructures (with similar characteristics to those obtained by using conventional AACVD method, i.e. in 'hot-wall' reactors), which represent a great economic improvement due to the optimization of material usage, the simplification of the processing steps and consequently the reduction of the processing time. The sensing devices fabricated using this method showed satisfactory sensitivities to H_2, CO and EtOH, pointing out the feasibility of a selective detection of CO in processes involving the presence of H_2 or EtOH.
5. WO_3 NNs decorated with Cu_2O nanoparticles were successfully grown onto MEMS gas sensor substrates via a single-step AACVD. The gas sensing results have revealed that the decoration of WO_3 NNs with Cu_2O nanoparticles dramatically increases their response to H_2S (i.e., a 700% increase in comparison to that of pristine tungsten oxide nanoneedles). A low detection limit below 300

ppb has been demonstrated. Furthermore, this hybrid nanomaterial shows the fastest response time ever reported (2 s) and very low moisture cross-sensitivity, which is rarely found in metal oxides. Consequently, these results pave the way for a new generation of nanotechnology-enabled H_2S analysers with superior performance.

6. Palladium (II) acetylacetonate as a precursor appeared to be very suitable for the growth of well dispersed Pd nanoparticles by using either single step or double step AACVD methods. In contrast, Ammonium hexachloropalladate(IV) as a precursor has shown its inefficacity to synthesize Pd nanoparticles by a single step process. These results revealed that functionalization using the double step approach opens a simple pathway to incorporate metal nanoparticles from a wide range of precursors with low solubility in organic solvents. Moreover, XPS results have shown that for as deposited coatings, the majority of the Pd nanoparticles were presented as Pd(0) state, while, after the annealing, all the nanoparticles were oxidized and converted to Pd(II). EDX analysis revealed that double steps route yielded the highest content of Pd nanoparticles compared to their counterpart, which makes it a cost–effective way of noble metal functionalization that could be adopted by the industry. Finally, the well dispersed Pd NPs produced from $Pd(acac)_2$ precursor, using single or double step AACVD method, have highly improved the gas sensing properties of WO_3 NNs toward H_2, which indicate that the carful choice of the precursors is of a primary importance in the fabrication of reliable gas sensors.

Finally, Table VI.1 gives a resume of important data recorded from all the fabricated sensors of this thesis work.

Table VI.1. Summary of important data recorded from all the fabricated sensors.

Sensor	Material characterization				Gas sensing results							
	Growth T (°C)	NPs-D (nm)	NNs-D (nm)	NNs-L (µm)	Target gas	Concentration (ppm)	Sensor substrate	Electrodes gap (µm)	Top (°C)	Ra/Rg	t_{res} (s)	t_{rec} (s)
Au/WO_3	350	4-10	60-100	8	EtOH	40	Alumina	700	250	4.23	73	164
	380	-----	-------	-------	EtOH	80	Polymeric substrate	5	320	7.25	----	----
	580	5-20	20-350	--------	EtOH	80	MEMs-substrate	50	390	6	10	644
	380	-----	-------	-------	H_2	500	Polymeric substrate	5	320	47.4	54	37
	580	5-20	20-350	--------	H_2	500	MEMs-substrate	50	390	5.6	15	752
	580	5-20	20-350	--------	CO	500	MEMs-substrate	50	390	1.87	44	210
Pt/WO_3	350	1-4	60-100	8	EtOH	40	Alumina	700	250	13.07	257	337
	380	-----	-------	-------	EtOH	80	Polymeric substrate	5	280	16	----	----
	580	5-12	20-350		EtOH	80	MEMs-substrate	50	330	3.46	61	376
	380	-----	-------	-------	H_2	500	Polymeric substrate	5	200	75.4	42	290
	380	-----	-------	-------	H_2	500	Polymeric substrate	90-120	200	31	51	158

	580	5-12	20-350	------	H_2	500	MEMs-substrate	50	390	8.37	36	587
	580	5-12	20-350		CO	500	MEMs-substrate	50	330	4.9	54	421
Pd/WO_3 (Ac-**1SD**)	400	3-5	40-120	7	H_2	500	MEMs-substrate	50	200	646	---	---
Pd/WO_3 (Ac-**2SD**)	400	4-6	50-150	19	H_2	500	MEMs-substrate	50	150	542	----	----
Pd/WO_3 (Am-**1SD**)	400	2-4	50–200	20	H_2	500	MEMs-substrate	50	250	26	----	----
Cu_2O/WO_3	380	2-3	50-240	5	H_2S	5	MEMs-substrate	50	390	27.5	2	684

Legend: NPs-D: diameter size of the NPs, NNs-D: diameter of the NNs, NNs-L: length of the NNs, Top: operating temperature, t_{res}: response time, t_{rec}: recovery time.

Some suggestions for future works:

- Working with other metal oxides such as indium oxide,
- Using surface-sensitive spectroscopies during sensor operation for better understanding of sensing mechanisms.

References

1. S. Vallejos, *et al.*, "Microsensors based on Pt–nanoparticle functionalised tungsten oxide nanoneedles for monitoring hydrogen sulfide", RSC Adv., vol. 4, pp. 1489–1495, 2014.
2. S. Zhang, *et al.*, "Facile fabrication of a well-ordered porous Cu-doped SnO2 thin film for H_2S sensing", ACS Appl. Mater, Interfaces., vol. 6, pp. 14975–14980, 2014.
3. L. He *et al.*, "Development of sensors based on CuO-doped SnO_2 hollow spheres for ppb level H_2S gas sensing", J. Mater. Sci., vol. 44, pp. 4326–4333, 2009.
4. North Carolina Department of Environment and Natural Resources, Summary of Rule Amending the Hydrogen Sulfide Acceptable Ambient Level, http://daq.state.nc.us/toxics/studies/H2S/, accessed: March, 2006.
5. M. Ke, *et al.*, "a MEMS-based benzene gas sensor with a self-heating WO_3 sensing layer", Sens., vol.9, pp. 2895–2906, 2009.
6. V.S. Vaishnava, *et al.*, "Development of ITO thin film sensor for detection of benzene", Sens. Actuators, B, vol. 206, pp. 381–388, 2015.
7. V.V. Ganbavle, *et al.*, "Rajpure, Development of Zn_2SnO_4 thin films deposited by spray pyrolysis method and their utility for NO_2 gas sensors at moderate operating temperature", J. Anal. Appl. Pyrolysis, vol. 107, pp. 233–241, 2014.
8. D. Zhang, *et al.*, "Detection of NO_2 down to ppb levels using individual and multiple In_2O_3 nanowire devices", Nano.Lett., vol.4, pp. 1919-1924, 2004.
9. A. Gurlo, *et al.*, "Nanosensors: towards morphological control of gas sensing activity. SnO_2, In_2O_3, ZnO and WO_3 case studies", Nanoscale, vol. 3, pp. 154–165, 2011.
10. G. Shen, *et al.*, "Vapor−Solid Growth of One-dimensional layer-structured gallium sulfide nanostructures", ACS Nano, vol. 3, pp. 1115–1120, 2009.
11. S. Vallejos, *et al.*, "Single-step deposition of Au- and Pt-nanoparticle-functionalized tungsten oxide nanoneedles synthesized via aerosol-assisted CVD, and used for fabrication of selective gas microsensor arrays", Adv. Funct. Mater., vol. 23, pp. 1313–1322, 2013.
12. R. S. Devan, *et al.*, "One-dimensional metal-oxide nanostructures: recent developments in synthesis, characterization, and applications", Adv. Funct. Mater., vol. 22, pp. 3326–3370, 2012 .

References

13. A. Riaz, *et al.*, "Carbon-, binder-, and precious metal-free cathodes for non-aqueous lithium–oxygen batteries: nanoflake-decorated nanoneedle oxide arrays", ACS Appl. Mater. Interfaces, 2014, 6, pp. 17815–17822.
14. A. Kolmakov, *et al.*, "Enhanced gas sensing by individual SnO_2 nanowires and nanobelts functionalized with Pd catalyst particles", Nano Lett., vol. 5, pp. 4667–4673, 2005.
15. G. F. Fine, *et al.*, "Metal oxide semi-conductor gas sensors in environmental monitoring", Sensors, vol. 10, pp. 5469-5502, 2010.
16. T. Seiyama, *et al.*, "A new detector for gaseous components using semiconductor thin film", Anal. Chem., vol. 34, pp.1502-1503, 1962.
17. N.Taguchi, Published patent application in Japan, S37-47677, Oct.1962.
18. M. Batzill, *et al.*, "The surface and materials science of tin oxide", Prog. Surf. Sci., vol. 79, pp. 47–154, 2005.
19. N. Yamazoe, *et al.*, "Oxide semiconductor gas sensors", Catal. Surv. Asia, vol. 7, pp. 63–75, 2003.
20. D.H. Yoon, *et al.*, "Microstructure and CO gas sensing properties of porous ZnO produced by starch addition", Sens.Actuators, B, vol. 45, pp. 251-257, 1997.
21. S. Bai, *et al.*, "Low-temperature hydrothermal synthesis of WO_3 nanorods and their sensing properties for NO2", J. Mater. Chem., vol. 22, pp. 12643–12650, 2012.
22. J. Szuber, *et al.*, "The effect of oxygen adsorption on the electronic properties of the polar GaAs (111) surface after thermal cleaning in ultrahigh vacuum", Thin solid films, vol. 170, pp. 219-226, 1989.
23. A. Rothschild, *et al*., "The effect of grain size on the sensitivity of nanocrystalline metal-oxide gas sensors", J. Appl. Surf., vol. 95, pp. 6374-6380.
24. M. Kaur, *et al.*, "Chemiresistor gas sensors: material, mechanisms and fabrications", in Science and Technology of chemiresistor gas sensors, D.K. Aswal and S. K. Gupta, Editors, Nova Science publisher, 2007.
25. E. Lassner *et al.*, "Tungsten: properties, chemistry, technology of the element, alloys, and chemical compounds", Kluwer Academic / Plenum Publishers, New York, 1999.
26. R. Chatten, *et al.*, "The oxygen vacancy in crystal phases of WO_3", J. Phys. Chem. B, vol. 109, pp. 3146–3156, 2005.
27. P. Woodward *et al.*, "Ferroelectric tungsten oxide", J. Solid. State. Chem., vol. 131, pp. 9–17, 1997.

28. P.M. Woodward, *et al.*, "Structure refinement of triclinic tungsten trioxide", J. Phys. Chem. Solids, vol. 56, pp.1305–1315, 1995.
29. J. M. Coronado, "Design of advanced photocatalytic materials for energy and environmental application", in green energy and technology, J. M. Coronado *et al.*, Eds., Springer, Verlarg London, 2013.
30. I. Jimenez, *et al.*, "Crystalline structure, defects and gas sensor response to NO_2 and H_2S of tungsten trioxide nanopowders", Sens. Actuators, B, vol. 93, pp. 475-485, 2003.
31. P. J. Shaver, "Activated tungsten oxide gas detectors", Appl. Phys. Lett., vol. 11, pp. 255–257, 1967.
32. Y.K. Chung, *et al.*, "Gas sensing properties of WO_3 thick film for NO_2 gas dependent on process condition", Sens. Actuators, B, vol. 60, pp. 49–56, 1999.
33. M. Penza, *et al.*, "Tungsten trioxide (WO_3) sputtered thin films for a NOx gas sensor", Sens. Actuators, B, vol. 50, pp. 9–18, 1998.
34. M. Akiyama, *et al.*, "Tungsten oxide based semiconductor sensor highly sensitive to NO and NO_2", Chem. Lett., vol. 20, pp. 1611–1614, 1991.
35. L.G. Teoh, *et al.*, "Sensitivity properties of a novel NO_2 gas sensor based on mesoporous WO_3 thin film", Sens. Actuators, B, vol. 96, pp. 219–225, 2003.
36. S.H. Wang, *et al.*, "Nano-crystalline tungsten oxide NO_2 sensor", Sens. Actuators, B, vol. 94, pp. 343–351, 2003.
37. L.F. Reyes, *et al.*, "Gas sensor response of pure and activated WO_3 NPs films made by advanced reactive gas deposition", Sens. Actuators, B, 117, pp. 128–134, 2006.
38. Y.G. Choi, *et al.*, "Wet process-based fabrication of WO_3 thin film for NO_2 detection", Sens. Actuators, B, vol. 101, pp. 107–111, 2004.
39. H. Xia, *et al.*, "Au-doped WO_3-based sensor for NO_2 detection at low operating temperature", Sens. Actuators, B, vol. 134, pp. 133–139, 2008.
40. E.P.S. Barrett, *et al.*, "The mechanism of operation of WO_3 based H_2S sensors", Sens. Actuators, B, vol. 1, pp. 116–120, 1990.
41. I. M. Szilagyi, *et al.*, "Gas sensing selectivity of hexagonal and monoclinic WO_3 to H_2S", Solid State Sci., vol. 12, pp. 1857–1860, 2010.
42. M. Stankova, *et al.*, "Sensitivity and selectivity improvement of rf sputtered WO_3 microhotpalte gas sensors", Sens. Actuators, B, vol. 113, pp. 321–326, 2006.
43. J.L. Solis, *et al.*, "Nanocrystalline tungsten oxide thick films with high sensitivity to H2S at room temperature", Sens. Actuators, B, vol. 77, pp. 316–321, 2001.

References

44. J. L. Solis, *et al.*, "Gas-Sensing properties of nanocrystalline WO_3 films made by advanced reactive gas deposition", J. Am. Ceram. Soc., vol. 84, pp.1504–508, 2001.
45. Y. Shen, *et al.*, "Influence of effective surface area on gas sensing properties of WO_3 sputtered thin films", Thin Solid Films, vol. 517, pp. 2069–2072, 2009.
46. Ch. Zhang, *et al.*, "Highly sensitive hydrogen sensors based on co-sputtered platinum-activated tungsten oxide films", Int. J. Hydrogen. Energy, vol. 36, pp. 1107–1114, 2011.
47. Ch. Zhang, *et al.*, "Magnetron sputtered tungsten oxide films activated by dip-coated platinum for ppm-level hydrogen detection", Thin Solid Films, vol. 520, pp. 3679–3683, 2012.
48. A. Boudiba, *et al.*, "Preparation of highly selective, sensitive and stable hydrogen sensors based on Pd-doped tungsten trioxide", Proc. Eng., vol. 5, pp. 180–183, 2010.
49. E. Llobet, *et al.*, "Fabrication of highly selective tungsten oxide ammonia sensors", J. Electrochem. Soci, vol. 147, pp. 776–779, 2000.
50. T. Siciliano, *et al.*, "WO_3 gas sensor prepared by thermal oxidation of tungsten", Sens. Actuators, B, vol. 133, pp. 321–326, 2005.
51. V. Srivastava, et al., "Highly sensitive NH_3 sensor using Pt catalysed silica coating over WO3 thick films", Sens. Actuators, B, vol. 133, pp. 46–52, 2008.
52. C.N. Xu, *et al.*, "Selective detection of NH over NO in combustion exhausts by using Au and MoO_3 doubly promoted WO_3 element", Sens. Actuators, B, vol. 65, pp. 163–165, 2000.
53. X. Wang, *et al.*, "Study of WO-based sensing materials for NH and NO detection", Sens. Actuators, B, vol. 66, pp. 74–76, 2000.
54. M. Hübner, *et al.*, "CO sensing mechanism with WO_3 based gas sensors", Sens. Actuators, B, vol. 151, pp. 103–106, 2010.
55. M, Ahsan, et al., "Low temperature CO sensitive nanostructured WO_3 thin film doped with Fe", Sens. Actuators, B, vol. 162, pp. 14–21, 2011.
56. R. Ionescu, *et al.*, "Low-level detection of ethanol and H_2S with temperature-modulated WO_3 NP gas sensors", Sens. Actuators, B, vol. 104, pp. 132–139, 2005.
57. J. Zhang, *et al.*, "Pt clusters supported on WO_3 for ethanol detection", Sens. Actuators, B, vol. 147, pp. 185–190, 2010.
58. C.V. G. Reddy, *et al.*, "Selective detection of ethanol vapor using $xTiO_2$–$(1 - x)$ WO_3 based sensor", Sens. Actuators, B, vol. 94, pp. 99–102, 2003.

References

59. R. Ionescu, *et al.*, "Ethanol and H_2S gas detection in air and in reducing and oxidising ambience: application of pattern recognition to analyse the output from temperature-modulated NP WO_3 gas sensors", Sens. Actuators, B, vol. 104, pp. 124–131, 2005.
60. A. Labidi, *et al.*, "Ethanol and ozone sensing characteristics of WO_3 based sensors activated by Au and Pd", Sens. Actuators, B, vol. 120, pp. 338–345, 2006.
61. W. Belkacem, *et al.*, "Cobalt nanograins effect on the ozone detection by WO_3 sensors", Sens. Actuators, B, vol. 132, pp. 196–201, 2008.
62. R.J. Wu, *et al.*, "Application of Au/TiO_2–WO_3 material in visible light photoreductive ozone sensors", Thin Solid Films, vol. 574, pp. 156–161, 2015.
63. C. C. Koch, Nanostructured materials: processing, properties, and applications: William Andrew Pub., 2007.
64. J. P. Reithmaier, *et al.*, Nanostructured materials for advanced technological applications: Springer, 2009.
65. S. Barth, *et al.*, "Synthesis and applications of one-dimensional semiconductors", Progress in Materials Science, vol. 55, pp. 563–627, 2010.
66. Y. Xia, *et al.*, "One-Dimensional nanostructures: synthesis, characterization, and applications", Adv. Mater., vol. 15, pp. 353–389, 2003.
67. A. Kolmakov, *et al.*, "Chemical sensing and catalysis by one-dimensional metal oxide nanostructures", Annu. Rev. Mater. Res., vol. 34, pp. 151–180, 2004.
68. G. Korotcenkov, *et al.*, "Grain size effects in sensor response of nanostructured SnO_2 and In_2O_3 based conductometric gas sensors", Rev. Solid State Mater. Sci., vol. 34, pp. 1-17, 2009.
69. E. Comini, *et al.*, "Quasi-one dimensional metal oxide semiconductors: Preparation, characterization and application as chemical sensors", Prog. Mater. Sci., vol. 54, pp. 1–67, 2009.
70. G. Neri, "First fifty years of chemoresistive gas sensors", Chemosensors, vol. 3, pp. 1–20, 2015.
71. K.J. Choi, *et al.*, "One-dimensional oxide nanostructures as gas-sensing materials: Review and issues", Sensors, vol. 10, pp, 4083–4099, 2010.
72. T. Stoycheva, *et al.*, "Micromachined gas sensors based on tungsten oxide nanoneedles directly integrated via aerosol assisted CVD", Sens. Actuators, B, vol. 198, pp. 210–218, 2014.
73. F. E. Annanouch, *et al.*, "AA-CVD growth and ethanol sensing properties of pure and metal decorated WO_3 nanoneedles", IJNT, vol. 10, pp. 455–469, 2013.

74. F. E. Annanouch, *et al.*, "Aerosol assisted chemical vapour deposition of gas-sensitive nanomaterials", Thin Solid Films, vol. 548, pp. 703–709, 2013.
75. A. J. T. Naik, *et al.*, "Nanostructured tungsten oxide gas sensors prepared by electric field assisted aerosol assisted chemical vapour deposition", J. Mater. Chem. A, vol. 1, pp. 1827–1833, 2013.
76. F. E. Annanouch, *et al.*, "Gas sensing properties of metal-decorated tungsten oxide nanowires directly grown onto flexible polymeric hotplates", Proc. Eng., vol. 87, pp. 700–703, 2014.
77. S. Park, *et al.*, "H_2S gas sensing properties of CuO-functionalized WO_3 nanowires", Ceramics Inter., vol. 40, pp. 11051– 11056, 2014.
78. F. Chávez, *et al.*, "Sensing performance of palladium-functionalized WO_3 nanowires by a drop-casting method", Appl. Surf. Sci., vol. 275, pp. 28–35, 2013.
79. S. Ma, *et al.*, "Synthesis and low-temperature gas sensing properties of tungsten oxide nanowires/porous silicon composite", Sens. Actuators, B. 192, pp. 341–349, 2014.
80. Y. Qin, *et al.*, "Nanowire (nanorod) arrays-constructed tungsten oxide hierarchical structure and its unique NO_2-sensing performances", J. Alloy. Compd, vol. 615, pp. 616–623, 2014.
81. C.S. Rout, *et al.*, "Sensors for the nitrogen oxides, NO_2, NO and N_2O, based on In_2O_3 and WO_3 nanowires", Appl. Phys. A, vol. 85, pp. 241–246, 2006.
82. B. Cao, *et al.*, "Growth of monoclinic WO_3 nanowire array for highly sensitive NO_2 detection", J. Mater. Chem., vol. 19, pp. 2323–2327, 2009.
83. B. Deb, *et al.*, "Gas sensing behaviour of mat-like networked tungsten oxide nanowire thin films", Nanotechnology, vol. 18, pp. 1-7, 2007.
84. V.B. Patil, *et al.*, "Hydrothermally synthesized tungsten trioxide nanorods as NO_2 gas sensors", Ceramic International, vol. 41, pp. 3845–3852, 2015.
85. J. Zhang, *et al.*, "Vertically aligned tungsten oxide nanorod film with enhanced performance in photoluminescence humidity sensing", Sens. Actuators, B, vol. 202, pp. 708–713, 2014.
86. H. Zhang, *et al.*, "TiO_2 (B) nanoparticle-functionalized WO_3 nanorods with enhanced gas sensing properties", Phys. Chem. Chem. Phys., vol. 16, pp. 10830–10836, 2014.
87. Q. Q. Jia, *et al.*, "Exposed facets induced enhanced acetone selective sensing property of nanostructured tungsten oxide", J. Mater. Chem. A, vol. 2, pp. 13602–13611, 2014.
88. C. Wongchoosuk, *et al.*, "Carbon doped tungsten oxide nanorods NO_2 sensor prepared by glancing angle RF sputtering", Sens. Actuators, B, vol. 181, pp. 388–394, 2013.

References

89. J. Yu, *et al.*, "A hydrogen/methane sensor based on niobium tungsten oxide nanorods synthesised by hydrothermal method", Sens. Actuators, B, 184, pp. 118–129, 2013.
90. Q. Xiang, *et al.*, "Au Nanoparticle Modified WO_3 Nanorods with Their Enhanced Properties for Photocatalysis and Gas Sensing", J. Phys. Chem. C, vol. 114, pp. 2049–2055, 2010.
91. S. J. Choi, *et al.*, "Facile synthesis of hierarchical porous WO_3 nanofibers having 1D nanoneedles and their functionalization with non-oxidized graphene flakes for selective detection of acetone molecules", RSC Adv., vol. 5, 7584–7588, 2015.
92. G. Wang, *et al.*, "Fabrication and Characterization of Polycrystalline WO_3 Nanofibers and Their Application for Ammonia Sensing", J. Phys. Chem. B, vol. 110, pp. 23777–23782, 2006.
93. J. y. Leng, *et al.*, "Synthesis and gas-sensing characteristics of WO_3 nanofibers via electrospinning", J. Colloid. Interface. Sci., vol. 356, pp. 54–57, 2011.
94. J. Li, *et al.*, "Synthesis, characterization and enhanced gas sensing performance of WO_3 nanotube bundles", New J. Chem., vol. 37, pp. 4241–4249, 2013.
95. Y. H. Lin, "Fabrication of tin dioxide nanowires with ultrahigh gas sensitivity by atomic layer deposition of platinum", J. Mater. Chem., vol. 21, pp. 10552–10558, 2011.
96. S. Matsushima, *et al.*, "Dispersion and electronic interaction of palladium particles supported on tin oxide", J. Chem. Soc. Jpn., vol. 1991, pp. 1677–1683, 1991.
97. R. G. Palgrave *et al.*, "Aerosol assisted chemical vapor deposition using nanoparticle precursors: A route to nanocomposite thin films", J. Am. Chem. Soc., vol. 128, pp. 1587–1597, 2006.
98. X. Hou, *et al.*, "Processing and applications of aerosol-assisted chemical vapor deposition", Chem. Vap. Depos., vol. 12, pp. 583–596, 2006.
99. K.-L. Choy, "Chemical vapour deposition of coatings", Prog. Mater. Sci., vol. 48, pp. 57–170, 2003.
100. M. Oljaca, *et al.*, "Flame Synthesis of nanopowders via combustion chemical vapor deposition", J. Mater. Sci. Lett., vol. 21, pp. 621-626, 2002.
101. H.B. Wang, *et al.*, "Deposition and characterization of YSZ thin films by aerosol-assisted CVD", Mater. Lett., vol. 44, pp. 23–28, 2000.
102. J. Zhao, *et al.*, "Tin oxide thin films prepared by aerosol-assisted chemical vapor deposition and the characteristics on gas detection", Sens. Actuators, B, vol. 145, pp. 788–793, 2010.

References

103. T. Stoycheva, *et al.*, "Aerosol-assisted CVD of SnO_2 thin films for gas-sensor applications", Chem. Vap. Deposition, vol. 17, pp. 247–252, 2011.

104. L. G. Bloor, *et al.*, "Tantalum and titanium doped In_2O_3 thin films by aerosol-assisted chemical vapor deposition and their gas sensing properties", Chem. Mater., vol. 24, pp. 2864−2871, 2012.

105. N. Panjawi, *et al.*, "The Preparation of titanium dioxide gas sensors by the electric field assisted aerosol CVD reaction of titanium isopropoxide in toluene", Chem. Vap. Deposition, vol.18, pp.102–106, 2012.

106. W. B. Cross, *et al.*, "Tungsten oxide coatings from the aerosol-assisted chemical vapor deposition of W(OAr)6 (Ar = C_6H_5, C_6H_4F-4, C_6H_3F2-3,4); photocatalytically active γ-WO_3 films," Chem. Mater., vol. 15, pp. 2786–2796, 2003.

107. W. B. Cross, "Chemical vapour deposition of tungsten oxide thin films from single source precursors," University College of London, London, 2002.

108. J. Courbat, *et al.*, "Design and fabrication of micro-hotplates made on a polyimide foil: electrothermal simulation and characterization to achieve power consumption in the low mW range", J. Micromech. Microeng, vol. 21, pp. 015014, 2011.

109. J. Courbat, *et al.*, "Drop-coated metal-oxide gas sensor on polyimide foil with reduced power consumption for wireless applications", Sens. Actuators, B, vol. 161, pp. 862–868, 2012.

110. J.F. McAleer, *et al.*, "Tin dioxide gas sensors. Part 2.-The role of surface additives", J. Chem. Soc., Faraday Trans. 1: Physical Chemistry in Condensed Phases, vol. 84, pp. 441–457, 1988.

111. D. Koziej, "Operando X-ray absorption spectroscopy studies on Pd-SnO_2 based sensors", Phys. Chem. Chem. Phys., vol. 11, pp. 8620–8625, 2009.

112. M. Hübner, et al., "The Structure and Behavior of Platinum in SnO_2-Based Sensors under Working Conditions", Angew. Chem. Int. Ed., vol. 50, pp. 2841–2844. 2011.

113. S. Vallejos, *et al.*, "Au nanoparticle-functionalised WO_3 nanoneedles and their application in high sensitivity gas sensor devices", Chem. Commun., vol. 47, pp. 565–567, 2011.

114. S. Vallejos, *et al.*, "Catalyst-free vapor-phase method f or direct integration of gas sensing nanostructures with polymeric transducing platforms", http://dx.doi.org/10.1155/2014/932129.

115. B.D. Sosnowchik, *et al.*, "Localized heating induced chemical vapor deposition for one-dimensional nanostructure synthesis", J. Appl. Phys., vol. 107, pp. 051101–14, 2010.

116. S. Vallejos, *et al.*, "AACVD Control parameters for selective deposition of tungsten oxide nanostrucutres", J. Nanosci. Nanotechnol., vol. 11, pp. 8214–20, 2011.

117. S. Vallejos, *et al.*, "Au nanoparticle-functionalised WO_3 nanoneedles and their application in high sensitivity gas sensor devices", Chem. Commun., vol. 47, pp. 565–567, 2011.

118. S. Vallejos, *et al.*, "Localized heating to tungsten oxide nanostructures deposition on gas microsensor arrays via aerosol assisted CVD, Solid-State Sensors, Actuators and Microsystems", Transducers & Eurosensors XXVII: The 17th International Conference, pp. 1166–1169, 2013.

119. S. Ashraf, *et al.*, "Aerosol assisted chemical vapour deposition of WO_3 thin films from tungsten hexacarbonyl and their gas sensing properties", J. Mater. Chem., vol. 17, pp. 3708–3713, 2007.

120. C.K. Tsung, *et al.*, "Shape-and orientation-controlled gold nanoparticles formed within mesoporous silica nanofibers", Adv. Funct. Mater., vol. 16, pp. 2225–2230, 2006.

121. J.M. Kim, *et al.*, "Preparation and characterization of Pt nanowire by electrospinning method for methanol oxidation", Electrochim. Acta., vol. 55, pp. 4827–4835, 2010.

122. C. Santato, *et al.*, "Crystallographically oriented mesoporous WO_3 films: synthesis, characterization, and applications", J. Am. Chem. Soc., vol., 123, pp. 10639–10649, 2001.

123. Y.-T. Hsieh, *et al.*, "Growth and optical properties of uniform tungsten oxide nanowire bundles via a two-step heating process by thermal evaporation", Thin Solid Films, vol. 519, pp. 1668–1672, 2010.

124. J.Y. Luo, *et al.*, "Evidence of localized water molecules and their role in the gasochromic effect of WO_3 nanowire films", J. Phys. Chem. C, vol. 113, pp. 15877–15881, 2009.

125. T. Sergio, "Work function, electronegativity, and electrochemical behaviour of metals: II. Potentials of zero charge and "electrochemical" work functions", J. Electroanal. Chem. Interfacial Electrochem., vol. 33, pp. 351-378, 1971.

126. T. He, *et al.*, "Photochromic materials based on tungsten oxide", J. Mater. Chem., vol. 17, pp. 4547–4557, 2007.

127. N. Yamazoe, *et al.*, "Theory of power laws for semiconductor gas sensors", Sens. Actuator, B, vol. 128, pp. 566–573, 2008.

128. F.E. Annanouch, *et al.*, "Localized aerosol-assisted CVD of nanomaterials for the fabrication of monolithic gas sensor microarrays", Sens. Actuator, B, accepted manuscript, 2015.

129. F.E. Annanouch, *et al.*, "Aerosol assisted CVD grown WO_3 nanoneedles decorated with copper oxide NPs for the selective and humidity resilient detection of H_2S", ACS Appl. Mater. Interfaces, doi: 10.1021/acsami.5b00411.

130. C. Navío, *et al.*, "Gold clusters on WO_3 nanoneedles grown via AACVD: XPS and TEM studies", Mater. Chem. Phys., vol. 134, pp. 809–813, 2012.

131. F. Y. Xie, *et al.*, "XPS studies on surface reduction of tungsten oxide nanowire film by Ar+ bombardment". J. Electron Spectrosc. Relat. Phenom., vol. 185, pp. 112–118, 2012.

132. L. Ottaviano, *et al.*, "Core level and valence band investigation of WO_3 thin films with synchrotron radiation", Thin Solids Films, vol. 436, pp. 9–16, 2003.

133. F. Bussolotti, *et al.*, "Surface electronic properties of polycrystalline WO_3 thin films: a study by core level and valence band photoemission", Surf. Sci., vol. 538, pp. 113–123, 2003.

134. G. Leftheriotis, *et al.*, "A. Effect of the tungsten oxidation states in the thermal coloration and bleaching of amorphous WO_3 films", Thin Solid Films, vol. 384, pp. 298–306, 2001.

135. H. Y. Wong, *et al.*, "Effects of ion beam bombardment on electrochromic tungsten oxide films studied by X-ray photoelectron spectroscopy and Rutherford back-scattering", Thin Solid Films, vol. 376, pp. 131–139, 2000.

136. A. B. Gurevich, *et al.*, "NEXAFS investigation of the formation and decomposition of CuO and Cu_2O thin films on Cu(100)", Surf. Sci., vol. 442, pp. L971– L976, 1999.

137. M. Grioni, *et al.*, "Studies of copper valence states with Cu L3 x-ray-absorption spectroscopy", Phys. Rev. B, vol. 39, pp. 1541–1545, 1989.

138. P. V. Tong, *et al.*, "Diameter controlled synthesis of tungsten oxide nanorod bundles for highly sensitive NO_2 gas sensors", Sens. Actuators, B, vol. 183, pp. 372–380, 2013.

139. EU, D., 50/EC of the European Parliament and of the Council of 21 May 2008 on ambient air quality and cleaner air for Europe. Official Journal of the European Union, 2008, L152.

140. L, Wang, *et al.*, "CuO nanoparticle decorated ZnO nanorod sensor for low-temperature H_2S detection". Mater. Sci. Eng. C, vol. 32, pp. 2079–2085, 2012.

141. A. Galtayries, *et al.*, "XPS and ISS studies on the interaction of H_2S with polycrystalline Cu, Cu_2O and CuO surfaces", Surf. Interface Anal., vol., 23, pp. 171–179, 1995.

142. Z. Bai, *et al.*, "Effect of humidity on the gas sensing property of the tetrapod-shaped ZnO nanopowder sensor", Mater. Sci. Eng. B, vol. 149, pp. 12–17, 2008.

143. O. Merdrignac-Conanec, *et al.*, "Humidity effect on baseline conductance and H2S sensitivity of cadmium germanium oxynitride thick film gas sensors", Sens. Actuators, B, vol. 63, pp. 86–90, 2000.

144. G. A. Ozin, *et al.*, "Intrazeolite nonstoichiometric tungsten oxides", J. Am. Chem. SOC., vol. 114, pp. 8953–8963, 1992.

145. A. Babaei, *et al.*, "Electrocatalytic promotion of palladium nanoparticles on hydrogen oxidation on Ni/GDC anodes of SOFCs via spillover", J. Electrochem. Soc., vol. 156, pp. B1022–B1029, 2009.

146. J. M. Tura, *et al.*, "XPS and IR (ATR) analysis of Pd oxide films obtained by electrochemical methods", Surf. Interface. Anal., vol. 11, pp. 447–449, 1988.

147. C. J. Jenks, *et al.*, "Photoelectron spectra of an $Al_{70}Pd_{21}Mn_9$ quasicrystal and the cubic alloy $Al_{60}Pd_{25}Mn_{15}$", Phys. Rev. B, vol. 54, pp. 6301–6306, 1996.

148. W. E. Moddeman, et al, "XPS surface and bulk studies of heat treated palladium in the presence of hydrogen at 150°C", Surf. Interface Anal., vol. 11, pp. 317–326, 1988.

149. A. Tressaud, *et al.*, "X-Ray Photoelectron Spectroscopy of Palladium Fluorides", Allg. Chem., vol. 540, pp. 291–299, 1986.

150. T. H. Fleisch, *et al.*, "Photoreduction and Reoxidation of Platinum Oxide and Palladium Oxide Surfaces", J. Phys. Chem., vol. 90, pp. 5317–5320, 1986.